LITHIUM INTERCALATION REACTIONS WITH TRANSITION METAL OXIDES

A thesis submitted to the

Department of Chemistry

University of Cape Town

in fulfilment of the requirements for the degree of

Doctor of Philosophy

by

Rosalind June Gummow

Division of Materials Science and Technology
CSIR
PO Box 395
Pretoria
0001

August 1993

ABSTRACT

An investigation of several lithium transition metal oxide systems has been undertaken with the aim of synthesising an optimised $LiMO_2$ compound (M = Mn, Co or Co/Ni mixtures) for application as a cathode in rechargeable lithium batteries. Attention has been focused on systems which show promise for application as cathodes in rocking-chair cells which do not contain metallic lithium anodes.

A novel lithium cobalt oxide, LT-$LiCoO_2$ (LT for low temperature), has been synthesised at 400°C. This compound has near-cubic symmetry and can be indexed to either a trigonal unit cell (space group $R\bar{3}m$) with a=2.830(1)Å and c=13.875(8)Å, or to a face-centred cubic unit cell (space group Fd3m) with a=8.002(1)Å. The near-cubic symmetry is maintained on delithiation.

Neutron and X-ray powder diffraction refinement of the LT-$LiCoO_2$ sample has shown it to be best described as a layered structure ($R\bar{3}m$ symmetry) with approximately 6% of the cobalt cations in the predominantly lithium layer and vice versa. An acid-leached sample LT-$Li_{0.4}CoO_2$ was, however, shown to have a defect spinel structure.

Electrochemical extraction of lithium from LT-Li_xCoO_2 occurs on a constant voltage plateau at 3.61V versus lithium for $0.2<x<0.95$. Li/LT-$LiCoO_2$ cells charge and discharge at significantly lower voltages than Li/HT-$LiCoO_2$ cells (HT for high temperature) when cycled galvanostatically. Li/LT-$LiCoO_2$ cells however show poor reversibility and large polarisation voltages.

Nickel doping of LT-$LiCoO_2$ cathodes has been investigated. LT-$LiCo_{1-y}Ni_yO_2$ compounds with y=0.1 and 0.2 are essentially single phase with very similar X-ray diffraction patterns and electrochemical properties compared to LT-$LiCoO_2$. The addition of nickel dopants improves the specific capacity and reversibility of LT-$LiCoO_2$ cathodes. The chemically delithiated compound LT-$Li_{0.4}Co_{1-y}Ni_yO_2$, in particular, shows improved cycling performance compared to LT-$Li_{0.4}CoO_2$ suggesting that the spinel structure is stabilised by the addition of nickel dopants. For nickel contents greater than

20% a second phase, $Li_yNi_{1-y}O$, is also visible in the X-ray diffraction patterns of LT-$LiCo_{1-y}Ni_yO_2$ compounds. The nickel analogue of LT-$LiCoO_2$, LT-$LiNiO_2$ could not be synthesised; the X-ray diffraction patterns of $LiNiO_2$ products synthesised at 400°C showed only peaks of the rocksalt phase NiO.

A fully lithiated "$LiMnO_2$" compound, closely resembling the lithiated spinel $Li_2Mn_2O_4$ has been synthesised directly from simple precursors in a hydrogen atmosphere at 300-350°C. The "$LiMnO_2$" compounds formed under these conditions are slightly non-stoichiometric. An alternative synthesis technique, using carbon as reducing agent in argon at ~600°C, results in "$LiMnO_2$" products which are intergrowth structures of the tetragonal $Li_2Mn_2O_4$ phase and the orthorhombic $LiMnO_2$ phase. These compounds are electrochemically active and transform to the spinel structure on cycling.

To my husband, Bruce

ACKNOWLEDGEMENTS

The author would like to thank the following for their contributions to this dissertation:

Dr Michael Thackeray for his guidance, patience and for sharing his enthusiasm for the subject.

Professor L R Nassimbeni for his useful comments and advice.

Dr A W Paterson for financial support and for allowing the work performed at the Division of Materials Science and Technology to be used for this thesis.

Dr W I F David and Dr S Hull of the Rutherford Appleton Laboratory for performing the neutron diffraction experiments and carrying out the refinements of the neutron diffraction data.

Dave Liles for his willing assistance in performing the Rietveld refinements of the X-ray data of lithium cobalt oxides and for the preparation of several of the crystallographic diagrams.

Hans Lachmann, Gerda Gries and Monika Schatz for performing atomic absorption analyses.

Julian Stander for performing the particle size and surface area analyses.

All my colleagues in Battery Technology for their encouragement and assistance.

My husband Bruce and my family for their patience and constant moral support.

TABLE OF CONTENTS

CHAPTER 2 : EXPERIMENTAL TECHNIQUES 27

LIST OF FIGURES

LIST OF TABLES

PUBLICATIONS

Sections of this work have been published.

1. *Structure and Electrochemistry of Lithium Cobalt Oxide Synthesised at 400°C,* R J Gummow , M M Thackeray, W I F David and S Hull, Mat. Res. Bull., **27**, 327 (1992).

2. *Lithium-Cobalt-Nickel-Oxide Cathode Materials Prepared at 400°C for Rechargeable Lithium Batteries,* R J Gummow and M M Thackeray, Solid State Ionics, **53-56,** 681 (1992).

3. *Spinel versus Layered Structures for* $LiCoO_2$ *Synthesised at 400°C,* R J Gummow, D C Liles and M M Thackeray, Mat. Res. Bull., **28**, 235 (1993).

4. *A Reinvestigation of the Structures of Lithium-Cobalt-Oxides with Neutron-Diffraction Data*, R J Gummow, D C Liles, M M Thackeray and W I F David, Mat. Res. Bull. Submitted for publication (1993).

5. *Characterization of* $LT\text{-}Li_xCo_{1-y}Ni_yO_2$ *Electrodes For Rechargeable Lithium Cells,* R J Gummow and M M Thackeray. Submitted to J. Electrochem. Soc. (1993).

6. *Lithium Extraction from Orthorhombic Lithium Manganese Oxide and the Phase Transformation to Spinel*, R J Gummow, D C Liles and M M Thackeray. Submitted to Mat. Res. Bull. (1993).

PATENTS

1. *Lithium Transition Metal Oxide, Cobalt Case*, SA Patent 91/2329 , US Patent 5160712. (Also filed in UK, France, Germany, Canada and Japan).

2. *Electrochemical Cell, Discharged Cathode*, SA Patent 91/9814. (Also filed in USA, UK, France, Germany, Canada and Japan).

CHAPTER 1
INTRODUCTION

The development of the battery industry over the last fifteen years has been driven by an increasing awareness of the environment and by the rapid development of the microelectronics industry. The demand for small, efficient primary (non-rechargeable) batteries for electronic applications has grown steadily and primary lithium batteries are now widely used as power supplies for watches, calculators and for memory-back-up applications. These batteries typically contain a lithium intercalation compound as cathode and metallic lithium as anode.

During the last five years there has been a growing trend in the use of rechargeable (secondary) batteries for portable equipment, for example cellular phones, CD players, camcorders and lap-top computers. The battery of choice for these applications has been the nickel-cadmium cell which offers good rechargeability and reliability at moderate cost. A rechargeable lithium battery is a potential replacement for nickel-cadmium with higher energy density, better shelf life and the advantage of being assembled from non-toxic components. Several rechargeable lithium batteries have been developed to the prototype stage and a few have been available in the market-place for a short time but as yet they have not been successfully manufactured on a commercial scale.

This lack of commercial development can be attributed to the instability of lithium metal in contact with typical organic-solvent-based electrolytes. The surface of the lithium metal becomes coated with a passivating film[1,2] which ensures a good shelf-life for lithium batteries but leads to severe problems in electrode cyclability. When a cell is charged, lithium is deposited in granular form at the lithium anode. The passivation of these lithium deposits can lead to their effective electronic insulation and subsequent discharges are therefore less efficient. This leads to the formation of dendrites of finely divided lithium on the anode and a loss in cycling efficiency. Attempts have been made to improve the lithium cycling efficiency by modifying the electrolytes[3,4] or by applying uniaxial pressure to the lithium surface[5,6]. Using both optimum electrolytes and pressures of 1.4 MPa on the lithium electrodes, 99% cycling efficiencies have been achieved[7]. However, application of pressure to the lithium electrode limits the design possibilities for the batteries and requires the use of expensive separators to prevent shorting.

The finely divided lithium which is deposited at the anode on cycling is highly reactive and poses a safety hazard especially under conditions of abuse. Incidents of fires involving secondary Li/MoS_2 cells have been reported which led to the products being recalled[8,9]. One way of overcoming this problem is to replace the metallic lithium anode with a lithium intercalation compound. The charge and discharge of the cell then simply involves the transfer of lithium from a lithium intercalation cathode to a lithium intercalation anode i.e. the lithium is "rocked" back and forth. Cells of this type are therefore termed "rocking-chair" cells and were first proposed by Armand in 1980[10].

The use of the "rocking-chair" concept has given fresh impetus to the development of secondary lithium batteries. Sony Corporation of Japan recently announced that it was to commercially produce what they termed "lithium-ion" cells[11]. These cells are essentially "rocking-chair" cells and use $LiCoO_2$ as the lithium-rich cathode coupled with a carbon intercalation anode. This system offers the prospect of a D-size cell which can give a cycle life of 1200 cycles at 100% depth of discharge at an average voltage of 3.6 V which is three times that of a Ni-Cd battery.

"Rocking-chair" cells are assembled in the discharged state and the first charge cycle involves the transfer of lithium ions from the lithium rich cathode to the lithium deficient anode. In this work several intercalation cathodes which can be synthesised in the discharged state and can potentially be used as electrodes in "rocking-chair" cells have been synthesised and evaluated.

This chapter gives an introduction to intercalation reactions, the structure of intercalation compounds and performance requirements for battery electrodes.

1.1 INTERCALATION REACTIONS

In the case of an electroactive host, an intercalation reaction can be described by :-

$$z A^{+} + z e + H \rightarrow A_zH$$

where *A* is the guest species and ***H*** the host lattice. The guest species is introduced into the host lattice to yield a product with a structure which ideally closely resembles that of the host. The insertion or extraction of lithium from the host lattice frequently results a slight structural rearrangement of the host. The reactions are then strictly termed topotactic. The term intercalation is derived from the French "intercaler" meaning to put between layers and therefore strictly refers to the insertion of a guest species into a two-dimensional host structure. The terms intercalation, insertion and topotactic reactions are however used interchangeably in the current literature.

Since the insertion of lithium into a host lattice causes only minor modification to the host structure, such reactions are frequently readily reversible. As a result intercalation compounds have been studied widely for applications in, for example, electrochromic displays[12], "smart windows"[13] and as solid-state electrodes for secondary lithium batteries.

The conventional intercalation cell consists of a lithium metal anode, an intercalation cathode and a lithium ion conducting electrolyte. The anode and cathode are separated by an electronically insulating separator, e.g microporous polypropylene. When the cell is discharged lithium ions are inserted into the host lattice and the host is reduced. When the cell is charged, lithium ions are removed from the host lattice and the host lattice is oxidised.

For a conventional lithium intercalation cell the reactions at the cathode and anode respectively are :-

$$xLi + MX_n + ze \rightleftharpoons Li_xMX_n$$

$$Li \rightleftharpoons Li^+ + e$$

In a "rocking-chair" cell the lithium metal anode is replaced by a second lithium intercalation compound. The overall cell reaction for a "rocking-chair" cell with a lithium intercalation compound as both cathode and anode and lithium as the guest species can be described as :-

$$Li_yM_nY_m + MX_n \underset{discharge}{\overset{charge}{\rightleftharpoons}} Li_{(y-x)}M_nY_m + Li_xMX_n$$

1.2 ELECTRODE REQUIREMENTS FOR SECONDARY LITHIUM BATTERIES

If a secondary lithium battery is to compete successfully with the established Ni-Cd technology it must have acceptable voltage, capacity, energy density, shelf-life and rechargeability.

1.2.1 Voltage and Energy Density

Lithium metal is a desirable anode for an intercalation cell as it is the most electropositive and lightest metal in the electrochemical series. Replacing lithium metal as anode with any other compound as in a rocking-chair cell leads to unavoidable losses in cell voltage. The cathode materials used for rocking-chair cells therefore ideally have high voltages versus lithium to ensure acceptable overall cell voltages. Analogously compounds for anode applications are required to have low voltages versus lithium. Fig 1.1 shows the voltage ranges versus lithium for several commonly used electrode compounds.

Voltage stability over a charge/discharge cycle is also desirable for some electronic applications. Electrode materials with voltages which vary only slightly with lithium content are therefore preferred.

The energy of 1 mole of reaction, E_T is given by :-

$$E_T = -\Delta G = nFE_{cell}$$

where G is the Gibb's free energy, F is Faraday's constant and E_{cell} is the cell e.m.f. A high cell voltage therefore ensures a high cell energy. The energy density or specific energy of a cell is defined as the cell energy divided by the mass and is expressed in $\mathrm{Whrkg^{-1}}$ or in terms of the volume in $\mathrm{Whrl^{-1}}$.

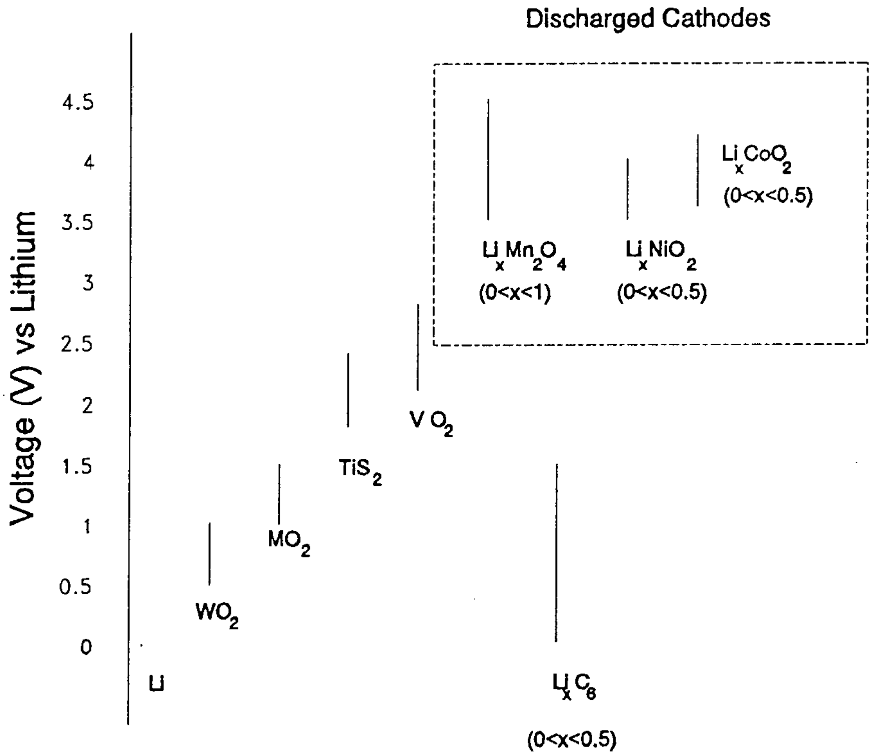

Figure 1.1 : Potential ranges vs lithium of various lithium intercalation compounds.

1.2.2 Specific Capacity

The theoretical specific capacity of a lithium intercalation electrode may be calculated as:-

$$\textit{Theoretical Specific Capacity} = \Delta x F/M$$

where Δx is the number of moles of lithium intercalated, F is Faraday's constant and M is the molar mass of the intercalation compound. The specific capacity is usually expressed in mAhr/g or Ahr/kg. A high theoretical capacity for an intercalation electrode is obtained when there is a wide range of x in Li_xMX_n.

In practical applications, the usable capacity of an intercalation electrode is often significantly less than the theoretical capacity. Lithium intercalation and deintercalation often result in irreversible structural modifications of the host lattice which significantly alter its electrochemical properties. An ideal intercalation electrode for a secondary cell has a lattice which changes very little with lithium content over a wide range of stoichiometry. Table 1.1 gives the characteristics of several rechargeable intercalation cells[11,14].

Fig. 1.2 gives a comparison of the discharge behaviour of several rocking-chair cells with a commercial D-size nickel-cadmium battery[15]. The data for $LiMn_2O_4$/carbon and $LiNiO_2$/carbon are extrapolated to practical hardware assuming, as an approximation, that 33% of the theoretical capacity is obtained in practice. The data for the $LiCoO_2$/carbon cell is that for Sony's D-size rechargeable batteries.

1.2.3 Power

The power delivered by a cell, P is defined by :-

$$P = iE_{cell}$$

where i is the current flowing and E_{cell} is the cell voltage. For intercalation cathodes the

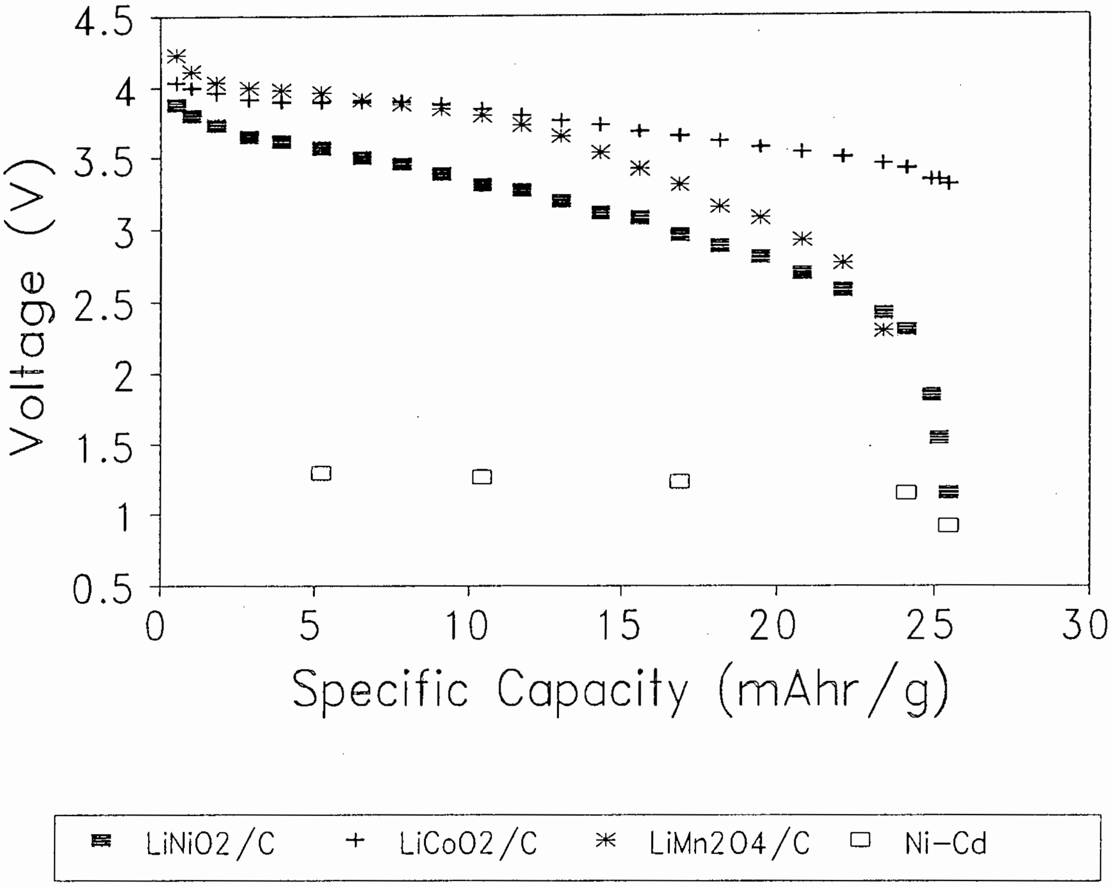

Figure 1.2 : A comparison of the discharge behaviour of several rocking-chair cells with a commercial Ni-Cd cell.[15]

Table 1.1 : Characteristics of some rechargeable intercalation cells

System	**x**	**Cathode Capacity (Ahr/kg)**	**Nominal discharge voltage(V)**	**Specific energy (Whr/kg)**
$xLi+LiMn_2O_4 \leftrightarrow Li_{1+x}Mn_2O_4$	1.0	143	2.8	400
$xLi+TiS_2 \leftrightarrow Li_xTiS_2$	1.0	235	2.1	473
$xLi+V_6O_{13} \leftrightarrow Li_xV_6O_{13}$	3.6	179	2.3	412
$C+LiCoO_2 \leftrightarrow Li_xC_6+$ $Li_{1-x}CoO_2$	0.5	140	3.6	115*

* Commercial Sony Lithium-ion cell

rate limiting process is the solid state diffusion of the lithium ions in the host lattice. Intercalation electrodes with high lithium ion diffusion rates are therefore required for high power applications. Table 1.2 contains a summary of some of the values of diffusion coefficients listed for intercalation compounds in the current literature. The diffusion rate limitation may be minimised by appropriate electrode design e.g. by using thin film electrodes.

Table 1.2 Chemical diffusion coefficients of lithium in several intercalation electrodes

Electrode	Diffusion Coefficient (cm^2s^{-1})
Li_xCoO_2[16]	$5\text{-}7 \times 10^{-8}$
Li_xTiS_2[17,18]	5×10^{-9}
$Li_xMn_2O_4$[15]	1×10^{-9}
Li_xC_6[15]	1×10^{-8} - 1×10^{-9}
Li_xNiO_2[19]	2×10^{-7}

1.2.4 Rechargeability

The rechargeability of a lithium battery is assessed in terms of the fraction of the initial charge or discharge capacity that is recovered on subsequent cycles. Due to the presence of side reactions e.g. electrolyte decomposition or irreversible changes in the host structure on cycling, the capacity decreases gradually as the electrode is cycled. Detailed studies of the changes in crystal structure of lithium intercalation electrodes as a function of lithium content reveal the nature of the changes that occur and enable the observed capacity losses to be understood. Overcharge or overdischarge protection is sometimes required to prevent irreversible degradation of electrodes.

The cycle life of a cell is defined as the number of charge/discharge cycles which can be performed by a cell before its capacity drops below a certain cut-off limit.

1.3 STRUCTURE OF LITHIUM INTERCALATION ELECTRODES

Lithium intercalation compounds were recognised as potential cathodes for rechargeable lithium batteries in the 1970's by several authors[20-24] and a large number of compounds have been evaluated. Whittingham was the first to demonstrate the possibility of a lithium intercalation cell using Li as the anode and TiS_2 as cathode with the anode and cathode reactions :-

$$Li \rightleftharpoons Li^{+} + e$$
$$TiS_2 + Li^{+} + e \rightleftharpoons LiTiS_2$$

The use of MX_2 dichalcogenides as intercalation cathodes in lithium batteries is limited by their low voltages versus lithium (2-2.5 V) and by the fact that they are sensitive to moisture. As a result attention has been shifted to the lithium transition metal oxides which are more oxidising than the chalcogenides and therefore offer higher voltages versus lithium.

Most of the oxides used as intercalation cathodes have structures which are either related to the ReO_3 structure or have oxygen close packing.

The ReO_3 structure is composed of octahedral $[ReO_6]$ units sharing corners. A large vacant 12 co-ordinate site is situated in the middle of a cube of 8 $[ReO_6]$ units. Each such site shares its square faces with neighbouring sites providing interconnecting channels in three perpendicular directions (Fig 1.3).

Many compounds with structures related to that of ReO_3 by crystallographic shearing have been studied as intercalation electrodes. These include ReO_3[25,26], monoclinic and hexagonal WO_3[27-29], V_2O_5[30], VO_2[31] and V_6O_{13}[32].

The transition metal oxides with oxygen close packing fall into three main categories : those with layered, spinel and rutile-related structures.

In the rutile structure the oxygen anions are hexagonally close packed with metal ions in

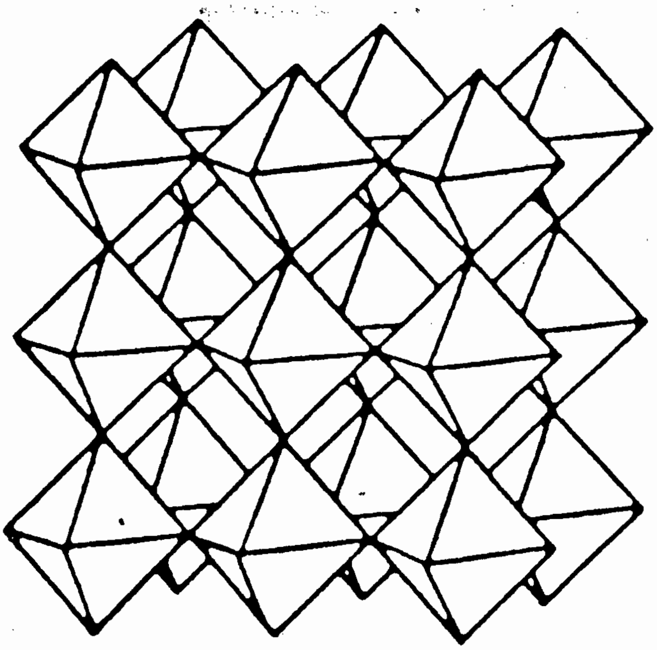

Figure 1.3 : Idealised structure of ReO_3

octahedral sites. Empty one-dimensional channels for Li^+ diffusion are formed by corner and edge-sharing octahedra. Several transition metal oxides with the rutile structure have been found to reversibly intercalate lithium e.g. MoO_2, WO_2, RuO_2[33].

γ-MnO_2 is the form of MnO_2 commonly used in aqueous MnO_2 batteries. It has a structure which has been described as an intergrowth of the rutile and ramsdellite structures. It contains both 1x1 and 2x1 empty channels for Li^+ diffusion. Recently an almost pure ramsdellite phase containing 2x1 channels for Li^+ diffusion has been synthesised and shown to be capable of reversibly intercalating lithium over a large composition range[34].

1.3.1 The Spinel Structure

Several lithium transition metal oxides crystallise with the spinel structure. Spinels have a framework structure with a three-dimensional network of inter-connecting sites available for lithium ion diffusion.

1.3.1.1 Description of the spinel structure

The AB_2X_4 spinel structure has a unit cell which contains 8 formula units and can be referred to the Fd3m space group. It consists of a cubic close packed anion array with the anions situated in 32e positions. The anion positions are determined by the parameter u. If $u=0.25$ then the anions at positions (u u u) are ideally cubic close packed but the value of u adjusts to accommodate different cations in the tetrahedral and octahedral sites. Most spinels have u-values in the range 0.25 to 0.27. One eighth of the tetrahedral sites, the 8a sites at (0.125 0.125 0.125) are filled and half of the octahedral sites, the 16d sites at (0.5 0.5 0.5) are filled. As the u parameter increases the 8a tetrahedra increase in size and the 16d octahedra decrease in size. There are several empty octahedral and tetrahedral sites in the structure. The empty octahedra, the 16c at (0 0 0) share faces with the 8a tetrahedra. The empty 8b tetrahedra share faces with four occupied 16d octahedra and the empty 48f tetrahedra share faces with 16d and 16c octahedra. The spinel structure is illustrated in Fig.1.4.

Table 1.3 gives the distances between the various crystallographic sites as a function of the lattice parameter a and the anion positional parameter u[35].

1.3.1.2. The effect of d-electron configuration

The d-electrons of transition metal cations generally do not participate directly in bond formation but do influence the co-ordination environment and properties such as magnetism.

The effect of d-electrons on structure and properties can be understood in terms of basic

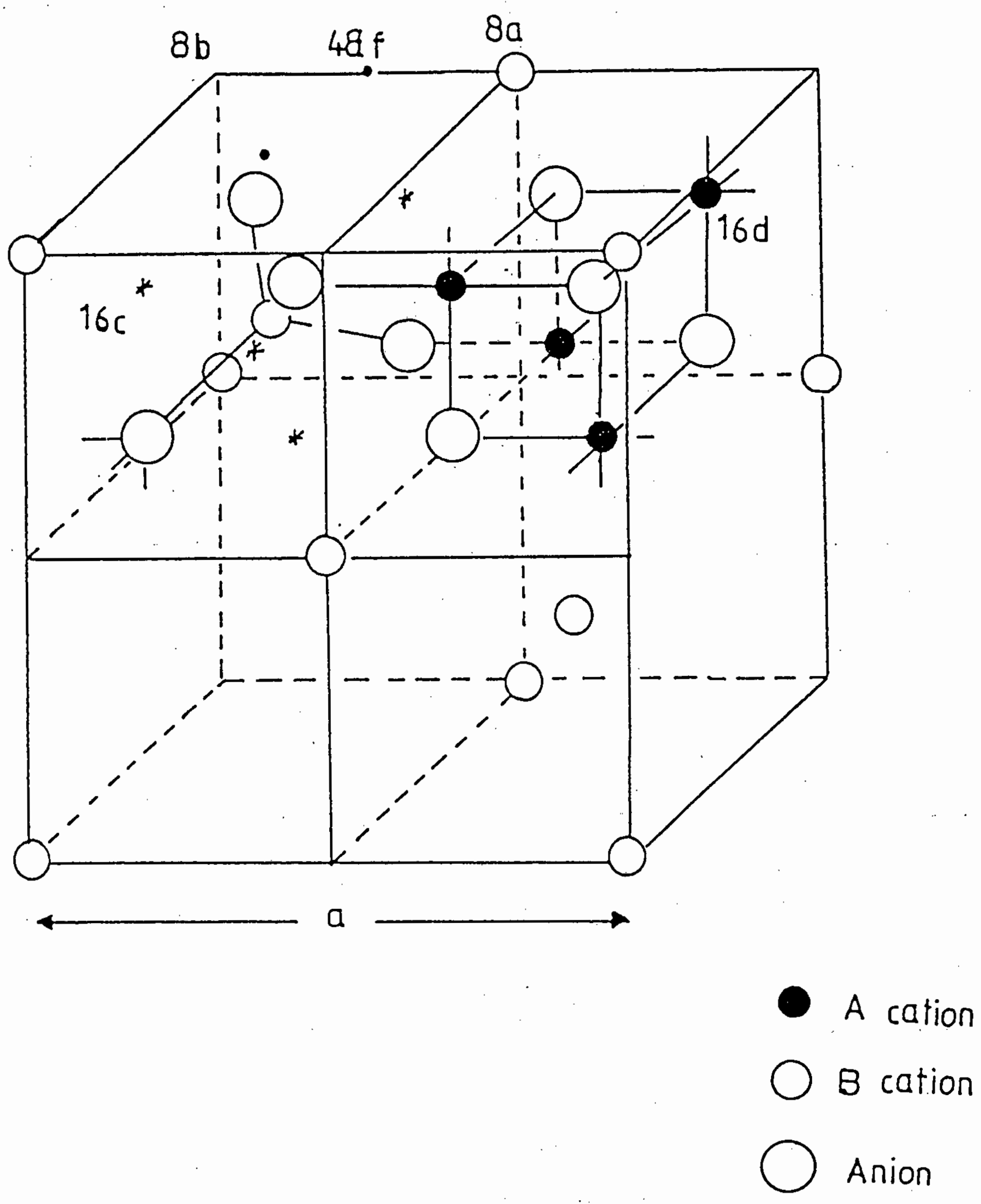

Figure 1.4 : Idealised structure of an AB_2X_4 spinel

Table 1.3 Interatomic distances as a function of the unit cell edge *a* and the anion positional parameter *u* in a $A[B]_2X_4$ spinel.

Atom Pair	Distance	Comments
A..A	$a\sqrt{3}/4$	tet-tet cation separation
A..B	$a\sqrt{11}/8$	tet-oct cation separation
B..B	$a\sqrt{2}/4$	oct-oct cation separation
A-X	$a\sqrt{3}(u\text{-}0.125)$	tet bond
B-X	$a(3u^2\text{-}2u+0.375)^{0.5}$	oct bond
X..X	$a\sqrt{2}(2u\text{-}0.25)$	tet edge
X..X	$a\sqrt{2}(0.75\text{-}2u)$	shared oct edge
X..X	$a(4u^2\text{-}2u+0.375)^{0.5}$	unshared oct edge

crystal field theory (CFT). In a free transition metal ion the 5 d-orbitals are degenerate. However when the ion is either tetrahedrally or octahedrally co-ordinated the d-orbitals split into two non-degenerate groups (Fig 1.5). The splitting in tetrahedral co-ordination is smaller than in octahedral co-ordination ($\Delta_{tet}=4/9\Delta_{oct}$).

According to Hund's rule electrons occupy orbitals singly, if possible. For example, for a d^4 ion in octahedral co-ordination electrons first occupy the t_{2g} orbitals singly, the 4th electron can then either fill an e_g orbital (high spin) or be paired in a t_{2g} orbital (low spin). The configuration which is adopted depends on the relative magnitude of Δ and the spin-pairing energy P. The magnitude of Δ depends on the ligands and on the transition metal. Large Δ is found for high field ligands e.g. CN^- and results in low spin configurations. The magnitude of Δ also increases from the 3d to 4d to 5d transition metal series. The crystal field strength of O^{2-} is low enough to allow high-spin configurations in most 3d transition-metal oxides.

The tetrahedral versus octahedral site preference of transition metal cations depends on their crystal field stabilisation energy (CFSE). In octahedral co-ordination each t_{2g} electron experiences a stabilisation of $(4/10)\Delta_{oct}$ and each e_g orbital a destabilisation of $(6/10)\ \Delta_{oct}$. In tetrahedral co-ordination each e electron has a stabilisation of $(6/10)\Delta$tet

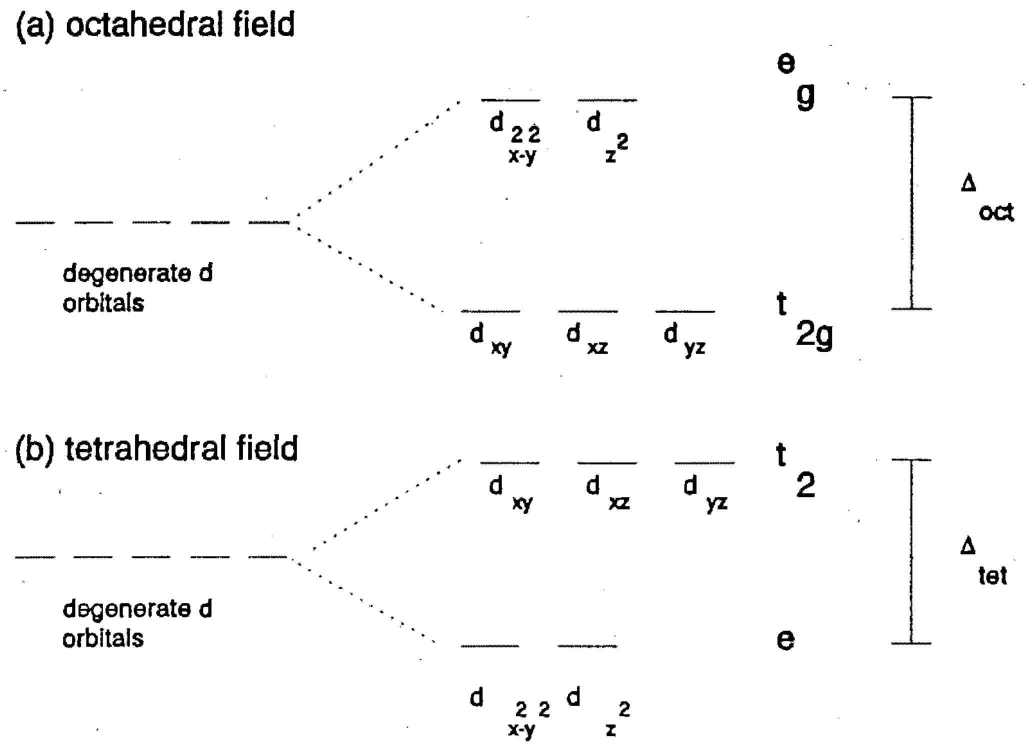

Figure 1.5 : Splitting of d energy levels in a) an octahedral and b) a tetrahedral field

and each t_2 electron has a destabilisation of $(4/10)\Delta_{tet}$. Values of CFSE calculated in this way may be used to predict site preferences but more accurate data can be obtained spectroscopically. Table 1.4 shows crystal field stabilisation energies estimated for several transition metal cations[36].

AB_2X_4 spinels can have cation distributions that are either normal $A[B_2]X_4$ or inverse $B[AB]X_4$, where the square brackets denote cations in 16d positions. Intermediate cation distributions are also found in some cases. The parameter γ is used to indicate the fraction of A ions on octahedral sites i.e. $\gamma=0$ for a normal spinel and $\gamma=1$ for an inverse spinel. The cation distribution in spinels is determined by both lattice energies and CFSE effects. If lattice energy is considered alone then calculations have shown that 2,3 spinels (i.e. $A=M^{2+}$ and $B=M^{3+}$) would tend to be normal while 4,2 spinels (i.e. $A=M^{4+}$, $B=M^{2+}$) would tend to be inverse. CFSE effects however influence the observed cation distribution.

Co_3O_4 for example is a normal spinel with $Co^{2+}(d^7)$ occupying tetrahedral sites and $Co^{3+}(d^6)$ in octahedral sites[37]. Co^{3+} is low spin and gains more CFSE in octahedral sites than Co^{2+} loses by occupying tetrahedral sites. Fe_3O_4 on the other hand is an inverse spinel[38]. $Fe^{3+}(d^5)$ has no CFSE in either tetrahedral or octahedral co-ordination while $Fe^{2+}(d^6)$ has an octahedral site preference.

Table 1.4
Crystal field stabilisation energies (kJ mol^{-1}) estimated for transition metal oxides

Ion		Octahedral stabilisation	Tetrahedral stabilisation	Excess octahedral stabilisation
Ti^{3+}	d^1	87.4	58.5	28.9
V^{3+}	d^2	160.1	106.6	53.5
Cr^{3+}	d^3	224.5	66.9	157.6
Mn^{3+}	d^4	135.4	40.1	95.3
Fe^{3+}	d^5	0	0	0
Mn^{2+}	d^5	0	0	0
Fe^{2+}	d^6	49.7	33.0	16.7
Co^{2+}	d^7	92.8	61.9	30.9
Ni^{2+}	d^8	122.1	35.9	86.2
Cu^{2+}	d^9	90.3	26.8	63.5

Several spinels have lattices which are distorted to tetragonal symmetry e.g. Mn_3O_4[39] and $CuFe_2O_4$[40]. The *c/a* ratio may be either greater than or less than 1. It is now generally accepted that the distortion is due to the Jahn-Teller effect as described by Dunitz and Orgel[41]. For example, in a d^9 cation one of the e_g orbitals contains one electron and the other contains two and in octahedral co-ordination the e_g orbitals are no longer degenerate (Fig 1.5). The presence of the d^4 Mn^{3+} cation in the octahedral sites accounts for the distortion in Mn_3O_4 while the d^9 Cu^{2+} cation in the tetrahedral sites similarly results in the distortion in $CuFe_2O_4$.

1.3.1.3 Lithium insertion and extraction from spinel oxides

Normal cubic spinels with prototypic Fd3m symmetry can be described by the notation $A_{(8a)}[B_2]_{(16d)}X_{4(32e)}$ i.e. the A cations occupy the tetrahedral 8a sites and the B cations the octahedral 16d sites respectively. The spinel structure also contains several empty sites: the 16c octahedral sites and the tetrahedral 8b and 48f sites.

The 8b tetrahedra share faces with 4 occupied 16d octahedra. The proximity of the B cations prevents insertion in these sites. The 48f tetrahedra share faces with two occupied 16d octahedra and two empty 16c octahedra. Insertion in these sites is therefore unlikely.

The 8a sites are the furthest away from the occupied 16d sites and are therefore energetically the most favourable for the A cations.

The empty 16c octahedra share faces with 6 vacant 48f tetrahedra and 2 occupied 8a tetrahedra. Lithium insertion into the 16c octahedral sites causes some, or all, of the 8a cations in the neighbouring 8a sites to migrate into 16c sites.

The $[B_2]X_4$ spinel framework therefore provides a three-dimensional network of interconnected 8a tetrahedral and 16c octahedral sites through which lithium cations can diffuse.

Lithium insertion into several transition metal oxides with the spinel structure has been studied e.g. Mn_3O_4[42], Fe_3O_4[43,44], $LiMn_2O_4$[42], LiV_2O_4[45].

In Fe_3O_4 ($Fe^{3+}[Fe^{2+}Fe^{3+}]O_4$), lithium ions enter the 16c sites and the Fe^{3+} ions are displaced from 8a to 16c sites by electrostatic repulsion while retaining the $[B_2]X_4$ spinel framework. It was found that Fe_3O_4 could be lithiated up to a composition $LiFe_3O_4$. Further lithiation resulted in extrusion of metallic iron from the lattice.

Similarly lithium can be inserted into Mn_3O_4 ($Mn^{2+}[Mn_2^{3+}]O_4$) to give $LiMn_3O_4$ while retaining the $[B_2]X_4$ spinel framework. Mn_3O_4 is tetragonally distorted (c/a=1.157) due to the presence of the d^4 Mn^{3+} ions. The axial ratio decreases when lithium is inserted to c/a=1.054 in $LiMn_3O_4$ as the concentration of the Mn^{3+} cations decreases.

In both Fe_3O_4 and Mn_3O_4 there are large transition metal cations in the 8a sites which would be expected to impede the diffusion of lithium in the interstitial space. Attention has therefore been focused on the LiM_2O_4 spinels which contain only lithium ions in the interstitial sites of the $[B_2]X_4$ spinel framework.

1.3.1.4. Li-Mn-O Spinels

Of great technological interest is the spinel $LiMn_2O_4$ which is a normal cubic spinel with lithium ions in the 8a tetrahedral sites. Lithium can be inserted into $LiMn_2O_4$ to give a fully lithiated product $Li_2Mn_2O_4$ in which the lithium ions have been found to occupy the 8a and 16c sites of the $[B_2]X_4$ spinel structure[42]. Lithiation of $Li_xMn_2O_4$ results in an almost immediate distortion of the lattice to tetragonal symmetry (c/a=1.16) and a two-phase region exists for $1<x<2$. Extensive lithiation with butyllithium eventually leads to the collapse of the spinel structure and the formation of Li_2MnO_2. This compound has a hexagonal close packed anion array with Mn^{2+} ions in alternate octahedral site basal planes and Li^+ in tetrahedral sites of the other basal planes[46].

Lithium can also be extracted from $LiMn_2O_4$ both by acid-leaching and by electrochemical methods to yield λ-MnO_2 with a defect spinel structure[47,48].

Synthesis of Li-Mn-O spinels at moderate temperatures (300-500°C) results in the formation of stoichiometric or defect spinels which can be represented by the general formula $Li_2O.yMnO_2$ ($y>2.5$) and contain manganese in the 4^+ oxidation state[49]. The end members of the $Li_2O.yMnO_2$ system are $Li_4Mn_5O_{12}$ ($y=2.5$) and λ-MnO_2 ($y=\infty$).

Table 1.5 shows the structural characteristics and electrode capacities of several selected Li-Mn-O spinel phases. The spinels of the $Li_2O.yMnO_2$ solid solution offer increased capacities compared to $LiMn_2O_4$ on the 3V plateau. The tetragonal distortion in Li-Mn-O spinels occurs approximately at an average manganese oxidation state of +3.5 and the large volume changes associated are largely responsible for the poor cycling of $LiMn_2O_4$ electrodes on the 3V plateau. The magnitude of the tetragonal distortion in $Li_2O.yMnO_2$ spinels is reduced ($c/a=1.14$) compared to that in $LiMn_2O_4$ ($c/a=1.16$) and significant capacity can be obtained from the cathodes before the tetragonal distortion occurs resulting in improved reversiblity of these cathodes on the 3V plateau compared to $LiMn_2O_4$.

Table 1.5 Structural characteristics and electrode capacities of selected spinel phases

Composition	Spinel Notation	Average Mn Valency	Symmetry	Theoretical Capacity (mAhr/g)
Mn_3O_4	$Mn[Mn_2]O_4$	2.67	Tetragonal	117
λ-MnO_2	$\square_{1.0}[Mn_2]O_4$	4.00	Cubic	308
$LiMn_2O_4$	$Li[Mn_2]O_4$	3.50	Cubic	148
$Li_2Mn_4O_9$	$(Li_{0.89}\square_{0.11})[Mn_{1.78}\square_{0.22}]O_4$	4.00	Cubic	213
$Li_4Mn_5O_{12}$	$Li[Li_{0.33}Mn_{1.67}]O_4$	4.00	Cubic	163

1.3.1.5 Synthesis of LiM_2O_4 spinels from layered precursors

Several LiM_2O_4 spinels cannot be synthesised directly. One possible synthesis route is from the layered $LiMO_2$ analogue. If the layered $LiMO_2$ compound is delithiated to the spinel composition, $Li_{0.5}MO_2$, and then heated gently to moderate temperatures (200-400°C), LiM_2O_4 spinels can be formed. The transition from the layered to spinel structures involves the migration of a quarter of the transition metal cations from the 3b sites of the transition metal layer to the 3a sites of the original lithium-rich layer and a rearrangement of the lithium cations in the lattice. This results in the spinel structure which has a 3:1 ratio of transition metal cations in alternate layers of octahedral sites in the {111} direction. This technique has been used successfully to synthesise LiV_2O_4[50] and $LiNi_2O_4$[51,52] spinels. The ease with which this transition occurs at moderate temperatures (200-300°C) emphasizes the stability of the spinel structure in comparison to a defect rocksalt structure.

1.3.2 Layered Intercalation Compounds

TiS_2 is typical of the class of two-dimensional layered intercalation compounds. The transition metal dichalcogenides MX_2 have a close-packed anion lattice with the transition metal cations in either octahedral or trigonal prismatic co-ordination. The X-M-X layers are held together by van der Waals bonding. Lithium insertion into the MX_2 lattice requires the layers to be prised apart. Several layered $LiMO_2$ oxides are known.

1.3.2.1 Description of $LiMO_2$ Structures with $R\bar{3}m$ Symmetry

The layered oxides $LiMO_2$ (M = Co[53], Cr[54], Ni[55], V[56]) are characterized by the trigonal space group $R\bar{3}m$. With hexagonal axes and the origin located at the centre of symmetry, the cubic-close-packed oxygen anions are located at positions 6c, (0 0 z), ideally at (0 0 0.25). The lithium and transition-metal cations ideally reside in alternate layers of octahedral sites between the cubic close packed oxygen planes. They are located at the special positions 3a and 3b at (0 0 0) and (0 0 0.5), respectively. All the octahedral sites of the unit cell are occupied. There are two empty sets of crystallographically independent tetrahedra in the unit cell. Both sets are located at 6c positions (0 0 z), one in the lithium layer and one in the transition-metal layer, ideally at (0 0 0.375) and (0 0 0.125). The octahedra share faces with the tetrahedra. Simultaneous occupation of face-sharing tetrahedra and octahedra is energetically unfavourable because of the short inter-site distance between them. Any negative deviation of the oxygen positional parameter from 0.25 compresses the MO_6 octahedra and elongates the LiO_6 octahedra. An idealised $R\bar{3}m$ structure of the $LiMO_2$ lattice is given in Fig 1.6.

1.3.2.2 Lithium extraction from layered $LiMO_2$ oxides

In the layered transition metal oxides the electrostatic repulsion between O-M-O layers

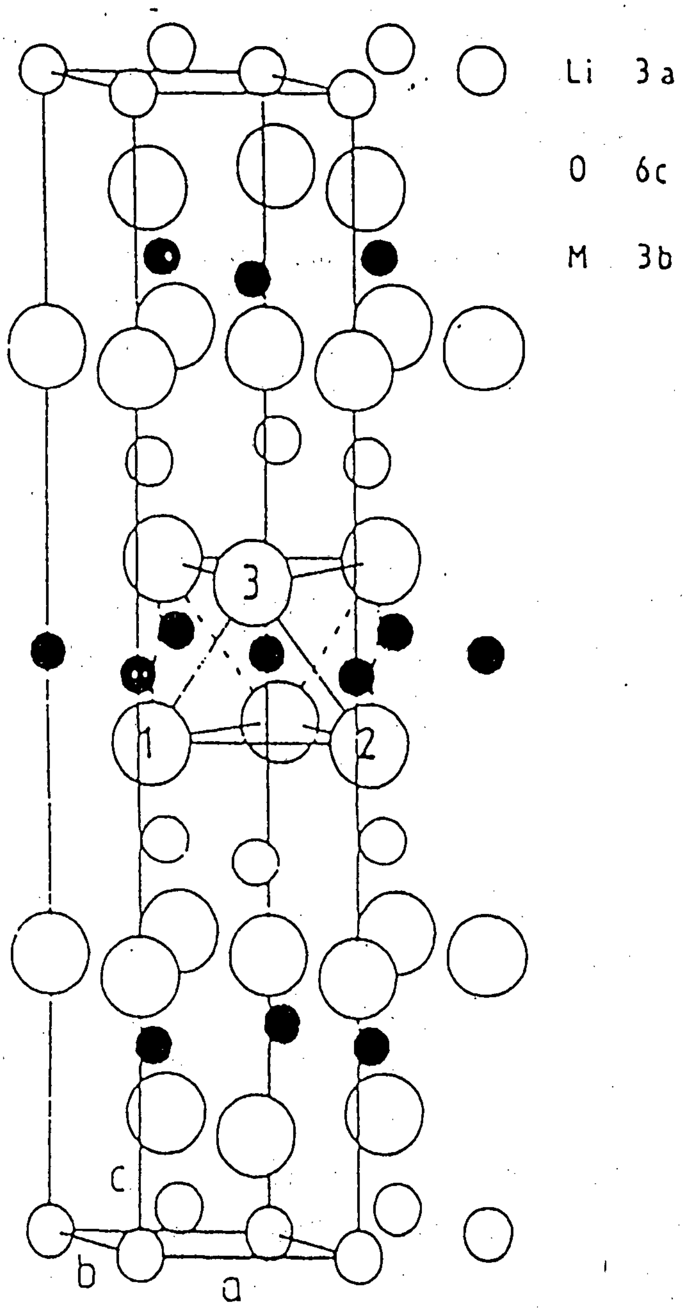

Figure 1.6 : Idealised $LiMO_2$ Structure with $R\bar{3}m$ Symmetry.

is stronger than the van der Waals forces between them. The MO_2 oxides are therefore not stable and lithium extraction from $LiMO_2$ compounds is accompanied by a rapid *c*-axis expansion. It has been argued that the *c*-axis degree of freedom in $LiMO_2$ compounds leads to enhanced lithium ion diffusion rates; for example the diffusion rate of lithium in $LiCoO_2$[16] is an order of magnitude higher than that in $LiTiS_2$[17,18].

The stability of the MO_2 framework on delithiation is critical to the application of these materials as cathodes in lithium batteries. The structure of delithiated Li_xMO_2 oxides can be modified by a displacement of transition metal cations from the 3b sites of the transition metal layer to the 3a sites of the original lithium layer. This transition occurs at some critical lithium content and is illustrated schematically in Fig.1.7. Such a structural transformation is irreversible and limits the reversible range in Li_xMO_2 cathodes. This behaviour has been observed in the case of Li_xVO_2[57] in which a third of the vanadium cations are displaced to the original lithium-rich layer at $x=0.67$. Further lithium extraction is possible and leads to a final composition of $Li_{0.1}V_{0.33}[V_{0.67}]O_2$ where $[V_{0.67}]$ refers to cations in the octahedral sites of the original vanadium layer.

In the case of $LiNiO_2$ this type of transformation has not been observed. It is widely recognised however that it is difficult to synthesise $LiNiO_2$ with the ideal stoichiometry. Samples are generally found to be deficient in lithium with an overall composition $Li_{1-x}Ni_{1+x}O_2$. The additional nickel cations are of necessity located in the lithium-rich layer resulting in a compound with an imperfect layered structure[58]. Some hysteresis in the a-axis and the unit cell volume on insertion and removal of lithium from the lattice has tentatively been attributed to migration of some Ni atoms into the Li layers at low x values[59].

Neutron diffraction studies of $LiCoO_2$ have shown it to have an almost ideal layered structure when synthesised at 900°C[60]. Lithium can be reversibly extracted from $LiCoO_2$ with three reversible phase transitions having been found for Li_xCoO_2 cathodes at voltages below 4.3 V versus lithium. Unlike the case of $LiVO_2$ however, these phase transitions involve minor modifications to the lattice and the CoO_2 framework is essentially maintained at least for $x>0.33$[61]. Mizushima et al observed a reduction in

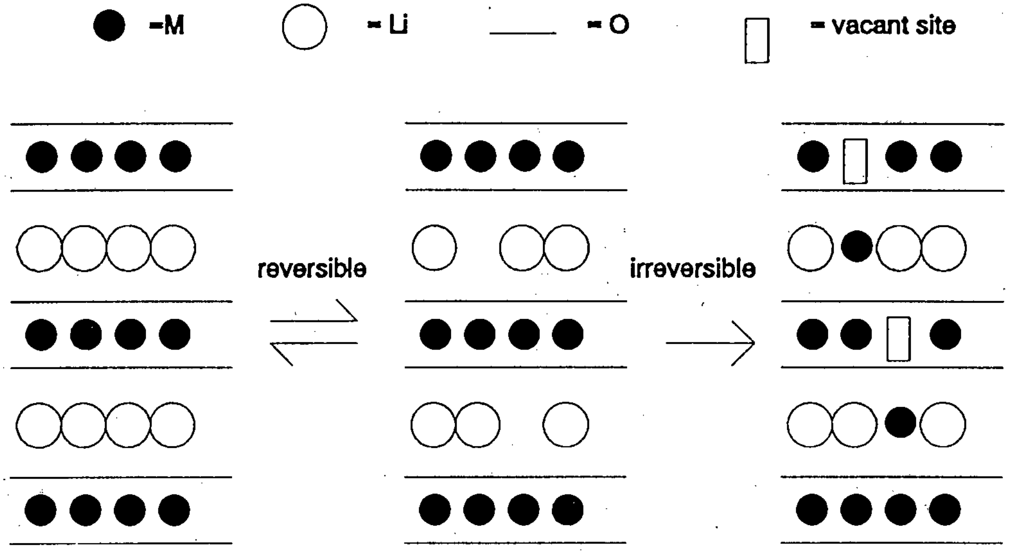

Figure 1.7 : Reversible and irreversible structural modifications in the $LiMO_2$ lattice with $R\bar{3}m$ symmetry.

crystallinity for $x<0.33$[62] and an irreversible phase transition above 4.3V has been reported[63].

The very high oxidation potentials of the Co^{3+}/Co^{4+} and Ni^{3+}/Ni^{4+} couples means that the voltages versus lithium of Li_xMO_2 compounds (M=Co or Ni) for low x values are outside of the electrolyte stability windows of commonly used electrolytes. This reduces the useful range of lithium stoichiometry for practical applications.

Both Li_xCoO_2 and Li_xNiO_2 as well as solid solutions of the type $Li_xCo_{1-y}Ni_yO_2$ are currently being investigated as cathodes for secondary lithium batteries. In this work the structure and electrochemistry of a low temperature (400°C) form of $LiCoO_2$ is reported and compared with that of the standard $LiCoO_2$ synthesised at 900°C. Low temperature synthesis of $Li_xCo_{1-y}Ni_yO_2$ cathodes is also investigated.

No $LiMnO_2$ compound with the $R\bar{3}m$ crystal structure is known to exist although the sodium analogue $NaMnO_2$ exists in two polymorphic forms : α-$NaMnO_2$ with a distorted R$\bar{3}$m structure and ß-$NaMnO_2$ with an orthorhombic structure. $LiMnO_2$ crystallises with an orthorhombic structure isostructural with ß-$NaMnO_2$[64].

The orthorhombic $LiMnO_2$ structure consists of Li and Mn cations arranged in zig-zag layers of octahedral sites parallel to the {001} direction. The idealised orthorhombic $LiMnO_2$ structure is illustrated in Fig 1.8.

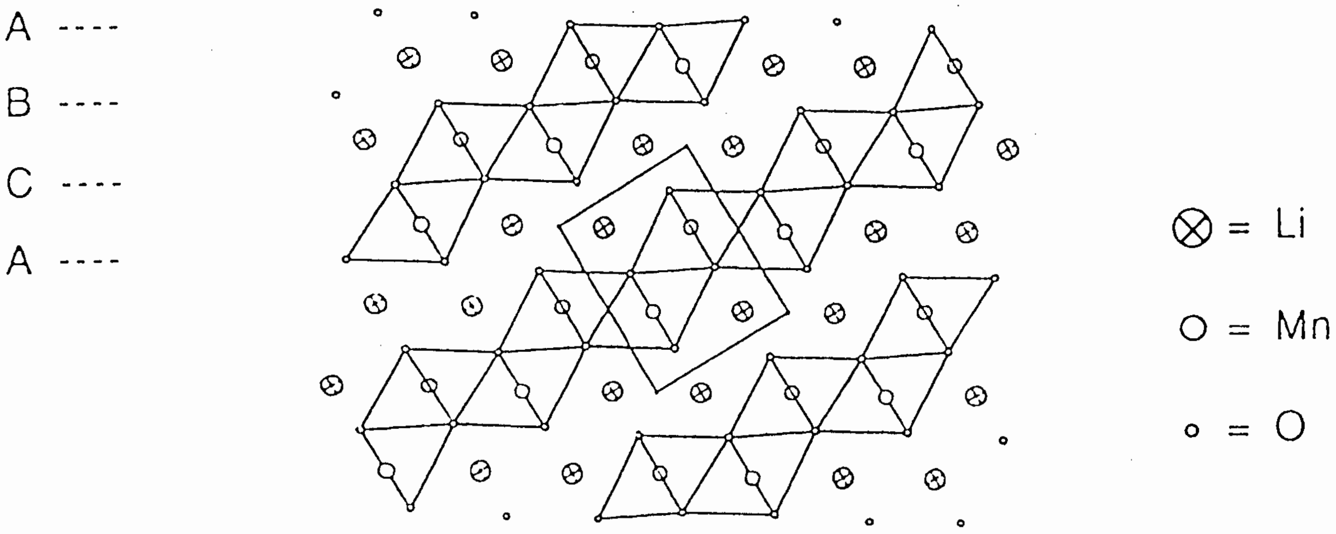

Figure 1.8 : Idealised structure of orthorhombic $LiMnO_2$

It has recently been demonstrated that it is possible to synthesise a layered lithium manganese oxide from Li_2MnO_3 by acid digestion. Li_2MnO_3 has a rocksalt structure in which layers of octahedral sites containing only lithium ions alternate with layers containing manganese and lithium ions in a 2:1 ratio (Fig 1.9). All the manganese ions in Li_2MnO_3 are in the 4^+ oxidation state preventing the electrochemical extraction of lithium from the structure. Acid-leaching of Li_2O from Li_2MnO_3 has, however, been shown to result in a single-phase $Li_{0.36}Mn_{0.91}O_2$ product comprised of alternate layers of trigonal prisms and sheets of edge-shared octahedra. Lithiation of $Li_{0.36}Mn_{0.91}O_2$ with LiI results in a $Li_{1.09}Mn_{0.91}O_2$ product which has a close-packed oxygen array and closely resembles the layered structures of $LiCoO_2$ and $LiNiO_2$[65].

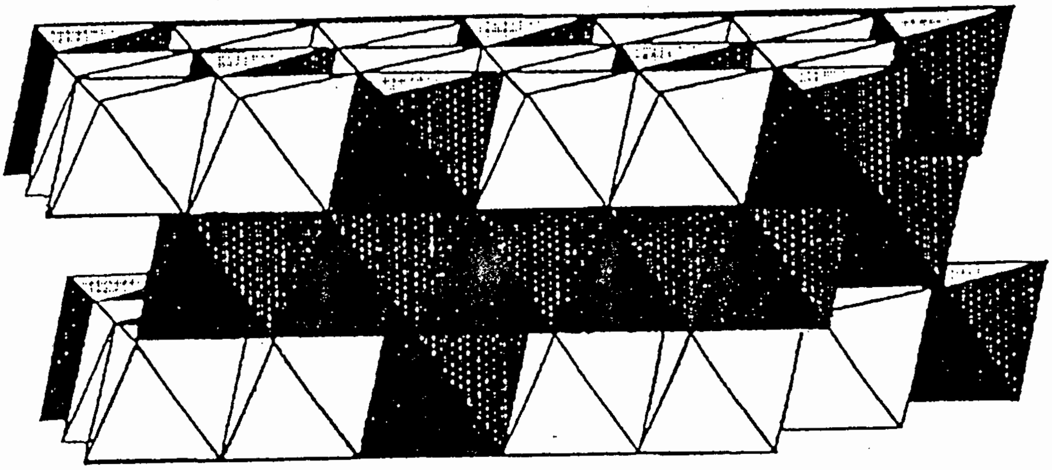

Figure 1.9 : Idealised diagram of the Li_2MnO_3 structure.

1.4 AIM OF THIS WORK

The development of commercial, rechargeable lithium batteries has been limited by concerns regarding their safety. The current efforts in this field are directed at developing rocking-chair cells using lithium intercalation compounds as both cathode and anode. This removes the need for a metallic lithium electrode and greatly increases the safety of the cells. The anode material of choice is low crystallinity carbon, typically petroleum coke, which has a high reversible capacity, high specific energy and is readily available. An ideal cathode material for a rocking-chair cell has not yet been developed.

The compounds $LiCoO_2$, $LiNiO_2$ and $LiCo_{1-y}Ni_yO_2$ are being incorporated into commercial rocking-chair cells, but their useful range of stoichiometry is limited by both their high voltages versus lithium at low lithium contents, and by irreversible phase changes which occur at low x values in Li_xMO_2 (M=Co, Ni or Co/Ni mixtures)[66-68].

The spinel $Li_xMn_2O_4$ has also been investigated as a partially discharged cathode for rocking-chair cells, utilising the composition range $0<x<1$. This gives a cathode with an average voltage of 4V versus lithium metal[15,69]. Despite the excellent reversibility demonstrated by this cathode it has a very high voltage versus lithium which requires the use of sophisticated electrolytes to prevent cell degradation. In addition, it does not contain any excess lithium to compensate for the inevitable loss of capacity after the first cycle of the carbon anodes typically used in rocking-chair cells.

It is possible to lithiate $LiMn_2O_4$ to a composition $Li_2Mn_2O_4$ either chemically or electrochemically, but lithium insertion for $1<x<2$ in $Li_xMn_2O_4$, is not very reversible.

The aim of this work is therefore to synthesise an optimised $LiMO_2$ cathode (where M=Mn, Co or Co/Ni mixtures) with a reduced operating voltage (3-3.6V), high specific capacity and improved cycling stability compared with standard materials e.g $LiCoO_2$, $LiNiO_2$ and $LiMn_2O_4$. The compound is also required to be synthesised in a lithium-rich or discharged state initially to allow it to be coupled with a carbon anode in a rocking-chair configuration.

The following aspects are examined in this work:-

- The effect of lowering the synthesis temperature of $LiCoO_2$ from 900°C to 400°C is investigated. The structure and electrochemistry of the novel form of $LiCoO_2$ (termed LT-$LiCoO_2$ for low temperature) is examined. The suitability of LT-$LiCoO_2$ as a cathode for rocking-chair cells is assessed.

- Previous investigators have found that the cycling stability of standard $LiCoO_2$ cathodes can be improved by the addition of nickel dopants. The effect of nickel-doping on the structural and electrochemical properties of LT-$LiCoO_2$ is therefore investigated.

- $LiNiO_2$ is also a potential candidate as an electrode for rocking-chair cells. The possibility of forming the nickel analogue of LT-$LiCoO_2$ by synthesis at 400°C is explored.

- A fully discharged, electrochemically active $LiMnO_2$ compound is an attractive cathode for a rocking-chair cell. Novel techniques for synthesising such compounds under reducing conditions are investigated. The suitability of these compounds as rocking-chair cell cathodes is examined.

CHAPTER 2

EXPERIMENTAL TECHNIQUES

Several experimental techniques were used in the course of this work to characterise the compounds under investigation. X-ray and neutron powder diffraction were used for structure determinations, thermal analysis was used to examine thermal stability and phase changes, and several different electrochemical techniques were applied to determine the electrochemical behaviour of the compounds being studied. In this chapter a brief description of each of these techniques will be given.

2.1 DIFFRACTION TECHNIQUES

Radiation with wavelengths of the same order of magnitude as the interatomic spacings of atoms in a crystal (~1 Å) is diffracted by crystal lattices to generate characteristic diffraction patterns. Two types of radiation are widely used for diffraction experiments: X-rays and neutrons.

X-rays were discovered in 1895 by Röntgen but it was only several years later that the diffraction of X-rays by crystals was explained by von Laue and Bragg. In 1932 the existence of the neutron was established and within four years it was demonstrated that the neutron could also be diffracted.

The interaction of radiation with matter is a scattering phenomenon. The incident beam is scattered in all directions by the atoms or ions of the lattice. In the case of X-rays, the interaction is with the electronic clouds of the atoms or ions, while for neutrons the interaction is with the nuclei of the atoms or ions of the crystal lattice. A peak in the scattered intensity is only observed if the scattered beams from different atoms or ions interfere constructively.

2.1.1 Bragg's Law

Bragg derived the law governing diffraction of X-rays in 1914 by describing diffraction as "reflection" from planes in a crystal lattice. Bragg's law is however equally valid for neutron diffraction.

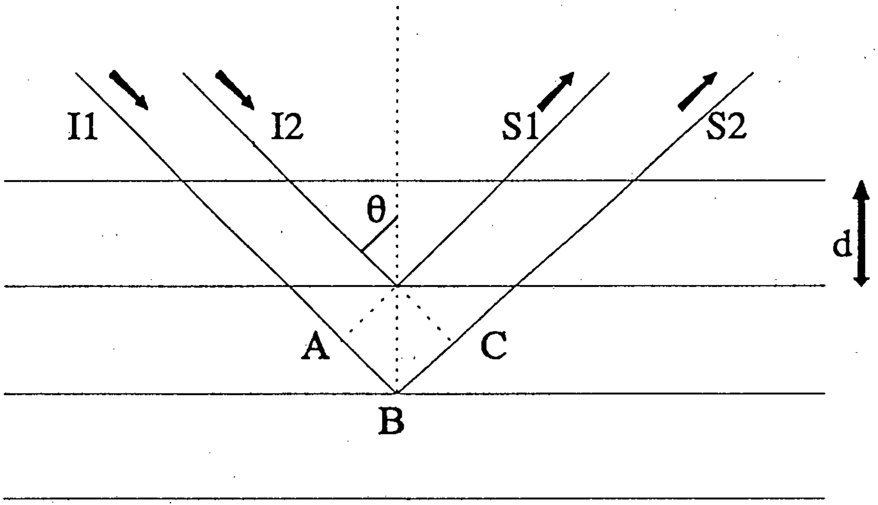

Figure 2.1 : Derivation of Bragg's Law of diffraction

The incident beams of radiation I1 and I2 (Fig. 2.1) are "reflected" by two parallel lattice planes separated by a distance d. The "reflected" beams S1 and S2 will be in phase and interfere constructively only if the difference in their path-lengths is an integral multiple of the radiation wavelength, λ. This condition is fulfilled if :-

$$AB + BC = n\lambda$$

or

$$2d \sin\theta = n\lambda \quad \textit{Bragg's Law}.......(2.1)$$

Although Bragg's law is derived by considering diffraction in terms of reflection of radiation from crystal planes, it gives the same result as a full mathematical treatment[70] which is beyond the scope of this work.

The planes of a crystal lattice are defined in terms of their Miller indices i.e. the reciprocals of their intercepts with the crystallographic axes. For example, if a plane has intercepts a/h, b/k and c/l with the crystallographic axes a, b and c, then its Miller indices are (h, k, l).

Bragg's law is more commonly written in the form :-

$$2d \sin\theta = \lambda \quad i.e. \; n=1$$

This is possible as an nth order reflection from a (h, k, l) plane is equivalent to a first order reflection from a (nh, nk, nl) plane.

2.1.2 Powder diffraction

Single crystal X-ray diffraction generates large amounts of data which enables accurate structure determinations. However the use of the technique is dependent on the availability of good quality single crystals of the compounds of interest. In the case of intercalation compounds, single crystals are generally not available. These materials are often made by solid state synthesis at moderate temperature and the products are sometimes metastable, transforming to other polymorphs at elevated temperatures. In the few cases where single crystals are available, the large volume changes commonly associated with lithium intercalation may cause the crystals to fracture.

Successful single-crystal studies have been performed in a few cases, for example $Li_{1+x}V_3O_8$, where detailed information regarding the structural changes which occur on lithiation has been obtained[71].

The powder diffraction technique using either X-ray or neutron radiation, is an attractive alternative. In this technique a finely divided, powdered sample is used and it is assumed that the particles are randomly distributed in such a way that all possible orientations of the crystal are represented in a sample. Powder X-ray diffraction has been widely used for the study of intercalation compounds and powder neutron diffraction is finding increasing application in this area particularly in the structural refinement of lithium intercalation compounds[72,73].

The major drawback of powder diffraction is that the three-dimensional data which would be collected for a single crystal sample is reduced to one dimension in powder diffraction. This results in peak overlap and a reduction in diffractometer resolution. This problem is generally most severe in the case of large unit cells or low symmetry materials.

Both X-ray and neutron powder diffraction studies were used in this work to determine structure and cation distributions for several lithium transition-metal oxides.

2.1.3. Experimental Apparatus

2.1.3.1. X-ray diffractometers

X-ray diffraction has the advantage of reasonable cost and accessibility over neutrons.

The original powder diffraction method was the Debye-Scherrer method. In this method a powdered sample was illuminated by a collimated X-ray beam and the diffracted beam was recorded on a film placed on a cylindrical support surrounding the sample. This original technique is seldom used today. In modern film methods (Guinier focusing methods), a convergent intense incident beam is used which gives excellent resolution of lines and reduces exposure times considerably.

Diffractometers use a scintillation or geiger counter as the detector instead of a photographic film and the output may be connected directly to a digital computer. In all other respects the geometry is identical to that of the Debye-Scherrer method. The detector is scanned slowly over a range of 2 theta values to detect the diffracted beams. In this work X-ray diffraction experiments were performed with a conventional flat-plate diffractometer. A schematic diagram of the diffractometer is shown in Fig.2.2[74].

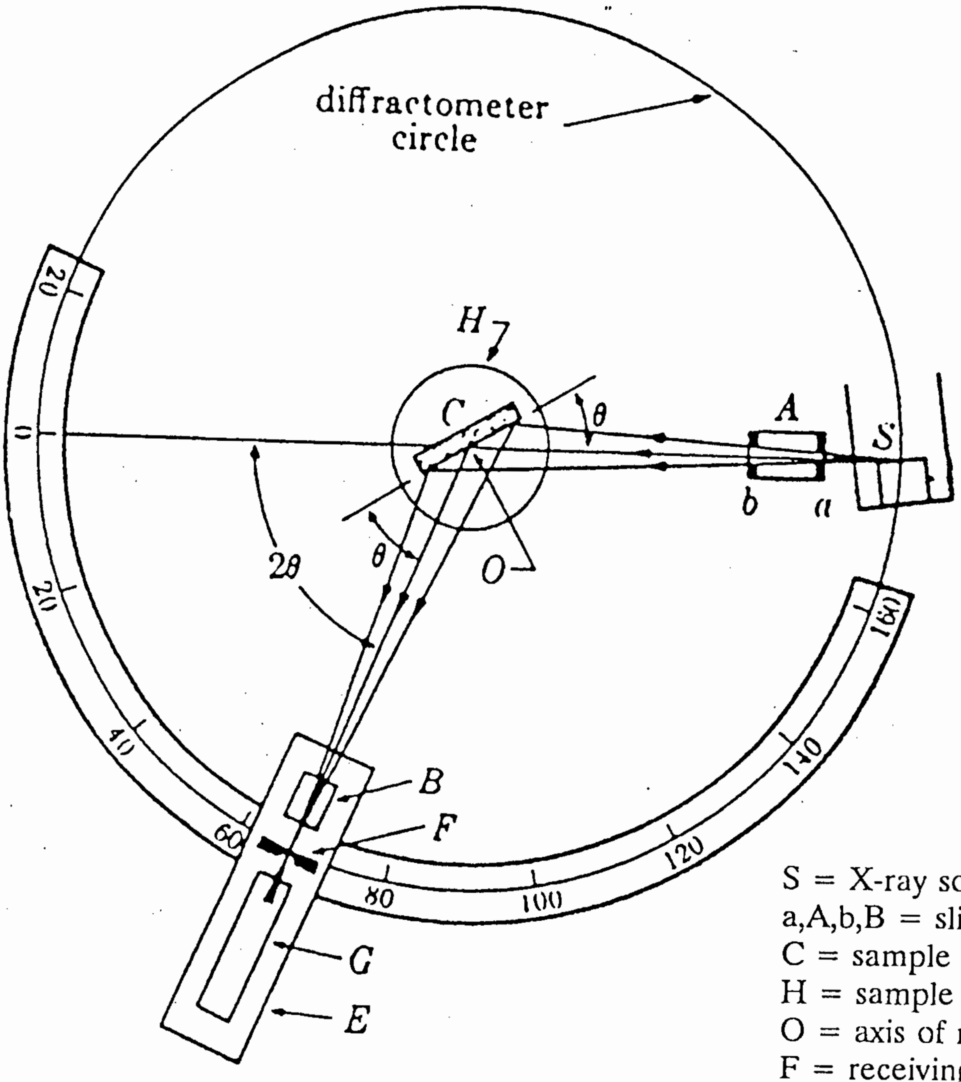

S = X-ray source
a,A,b,B = slits
C = sample
H = sample holder
O = axis of rotation
F = receiving slit
G = detector
E = detector holder

Figure 2.2 : Schematic diagram of a flat-plate diffractometer

Both diffractometers and modern focusing cameras use convergent X-ray beams. A convergent X-ray beam is produced by exploiting the geometrical properties of a circle. By ensuring that the source, the sample and the detector all lie on the circumference of a circle, the X-rays are made to converge at the detector. (Fig.2.3.)

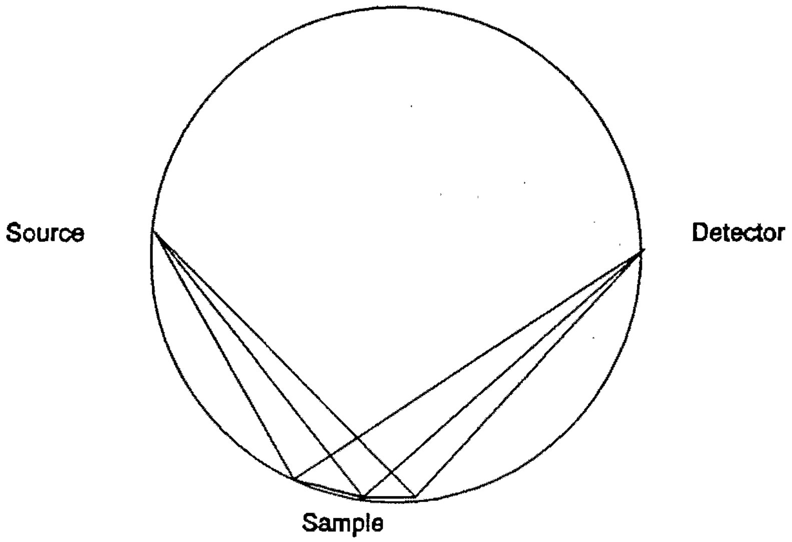

Figure 2.3. : Focusing of X-rays

Modern diffractometers generally use crystal monochromators to give highly monochromatic radiation. These consist of a single crystal of, for example, quartz or graphite. The crystal is orientated such that a set of strongly diffracting planes is at the Bragg angle for the desired wavelength of radiation. Only the selected wavelength is diffracted giving a monochromatic beam.

2.1.3.2 Neutron Diffraction Apparatus

The development of neutron diffraction as a scientific tool has been closely linked to the development of nuclear reactors and accelerators for neutron production.

Neutron powder diffraction experiments can be performed either under constant or variable wavelength conditions.

Constant wavelength neutron diffraction was the technique used for early neutron powder diffraction experiments and is used with steady-state reactor sources. It is essentially the same as the analogous X-ray technique. A neutron beam is generally monochromated with a single crystal monochromator as discussed for X-ray diffraction and the detector is rotated about the sample to detect the diffracted beams.

Variable wavelength neutron diffraction is used with synchrotron or spallation neutron sources. The advantage of this technique is that the full wavelength spectrum of the source may be used resulting in a far higher flux than with monochromatic sources. The neutron diffraction data discussed in this work were obtained with the Spallation Neutron Source at the Rutherford Appleton Laboratory in the U.K..

In the case of a variable wavelength technique, the detectors remain fixed and Bragg's law can be written as :-

$$\lambda_{hkl} = 2d_{hkl}\sin\theta$$

Spallation neutron sources produce pulsed, polychromatic radiation. The wavelength of neutrons is related to their velocity by :-

$$p_n = m_n v_n = \frac{h}{\lambda} \text{.........} \textit{de Broglie's Law}$$

where p_n, v_n and m_n are the momentum, velocity and mass of the neutron, h is Planck's constant and λ is the neutron wavelength,

$$v_n = \frac{L}{t}$$

where L is the total flight path of the neutron and t is the time-of -flight, then

$$t_{hkl} = 2\left(\frac{m_n}{h}\right) L d_{hkl} \sin\theta$$

This equation illustrates that the time-of-flight of the neutrons is proportional to the d spacing of the lattice planes for fixed θ and L values.

The neutron pulse at a spallation neutron source has a finite time width. The neutrons propagate non-dispersively since their wavelength and therefore also their velocity is constant and independent of their flight path. It therefore follows that the longer the flight path, *L* the higher the resolution since

$$\frac{\Delta L}{L}=\frac{\Delta t}{t}=\frac{\Delta d}{d}$$

where *d* is the interplanar spacing and *t* is the time-of-flight.

2.1.4 Structure Determination from Powder Diffraction Data

The powder diffraction spectrum of a compound contains structural information in both the position and intensity of the diffraction peaks.

The position of peaks in a powder diffraction pattern can be related to the interplanar spacing (*d*) using Bragg's law. The interplanar spacing is related to the Miller indices of the planes, the angles between the crystallographic axes and the lattice constants of the unit cell by specific relations depending on the symmetry. The general formula for a triclinic unit cell is :-

$$\begin{aligned}\frac{1}{d^2} = \frac{1}{V^2}[&h^2b^2c^2\sin^2\alpha + k^2a^2c^2\sin^2\beta + l^2a^2b^2\sin^2\gamma\\ &+ 2hkabc^2(\cos\alpha\cos\beta - \cos\gamma)\\ &+ 2kla^2bc(\cos\beta\cos\gamma - \cos\alpha)\\ &+ 2hlab^2c(\cos\alpha\cos\gamma - \cos\beta)]\end{aligned}$$

where V is the cell volume, h,k and l are the Miller indices, a, b and c are the lattice constants and α, β and γ are the angles between b and c, a and c and a and b respectively.

For a cubic crystal lattice with, α, β and γ = 90° and $a=b=c$ this reduces to:-

$$\frac{1}{d^2}=\frac{h^2+k^2+l^2}{a^2}$$

In order to determine the positions of atoms within the unit cell, the intensity distribution of the diffraction pattern must be examined. There are two possible ways in which this can be done. The first is known as integrated intensity refinement. In this technique, the integrated intensities of the peaks of the diffraction pattern are obtained and used for the refinement. This was the technique used for the earliest powder diffraction work. The second technique is the Rietveld technique[75,76]. In this method each point in the diffraction profile is used in the refinement without the intermediate step of obtaining integrated intensities. This technique only became feasible in 1967 with the introduction of powerful computers for data reduction.

Several factors affect the intensities of the diffracted peaks.

2.1.4.1 The Structure Factor

An X-ray or neutron scattered by an atom in a unit cell can be described as a wave F_j by

$$F_j=f_je^{i\delta_j}$$

where f_j is the amplitude of the scattered intensity referred to as the atomic scattering factor and δ_j is the phase and where

$$\delta_j=2\pi(hx_j+ky_j+lz_j)$$

where h, k and l are Miller indices and x_j, y_j and z_j are the atomic co-ordinates.

The total scattered intensity from all the atoms in a unit cell is decribed by the structure factor of the unit cell, F_{hkl}, which is simply a summation of F_j over all the atoms in the unit cell.

$$F_{hkl}=\sum_j f_je^{i\delta_j}$$

The information obtained from a diffractometer is in the form of intensities I where

$$I_{hkl} \propto |F_{hkl}|^2$$

The structure factor F_{hkl} contains most of the information relating the scattered intensity distribution to the structure of the unit cell. The atomic scattering factors for X-rays, f_j, are directly proportional to the number of electrons in a given atom (or ion) and inversely proportional to $\sin\theta/\lambda$. In contrast, since neutrons are scattered by the nucleus and not the electrons, the scattering factors for neutrons vary irregularly with the atomic number and show no variation with scattering angle (Fig 2.4). This means that light elements e.g. lithium which scatter X-rays weakly, scatter neutrons comparatively strongly.

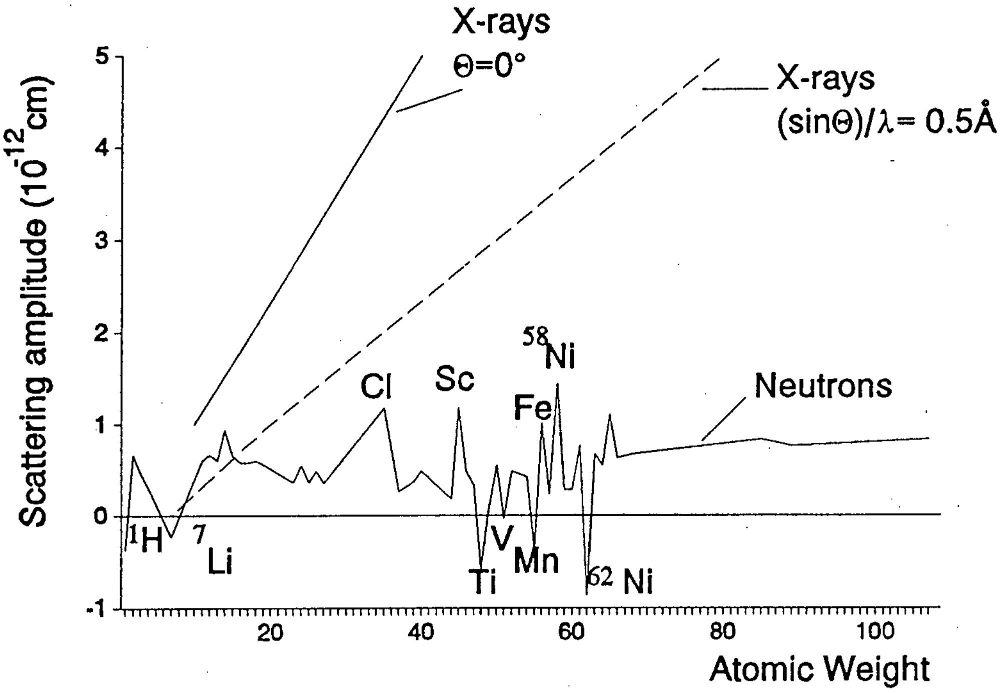

Figure 2.4 : Scattering of neutrons and X-rays[77].

This factor is the single most important advantage of neutron diffraction over X-ray diffraction for lithium intercalation compounds. While X-ray diffraction refinements allow the transition metal ion positions to be determined accurately, the lithium ion positions can generally not be refined independently due to the low X-ray scattering power of lithium. As can be seen from Fig 2.4, the neutron scattering of lithium is strong thus enabling a significantly better refinement of lithium ion positions from neutron data.

Also, while X-ray scattered intensities fall off with increasing scattering angle, the same is not true for neutrons enabling high angle data to be collected.

2.1.4.2 Peak Shape

The Rietveld method was originally developed for constant wavelength neutron diffraction where the peak shape can be defined by a simple "Gaussian" function as a good approximation. For time-of-flight neutron diffraction this is not the case and the neutron creation and moderation processes introduce asymmetry to the peaks. It is, however, possible to successfully model the peak shape by convolution of a Gaussian function and two decaying exponentials.

For X-ray diffraction, the peak shape is not well defined but can be modelled by sums of Lorentzians and Pseudo-Voigt functions.

2.1.4.3 Temperature Factor - B

The atomic scattering factors, f_j, for scattering centres are defined on the basis of a stationary ion. However, in practice, the ions in a crystal are vibrating about a mean position and the greater the temperature, the greater the vibration. This causes the cloud of the ion to be spread over a wider volume than that of a stationary ion. The scattering power of the real ion falls off more rapidly than that of the ideal stationary ion by a factor:-

$$e^{-B(\sin^2\theta)/\lambda^2}$$

where B, the isotropic temperature factor, is related to the mean-square amplitude of atomic vibration, $\bar{u}^2$ by:-

$$B = 8\pi^2\overline{u^2}$$

If the vibration is anisotropic, six vibrational parameters are needed to describe a thermal ellipsoid.

2.1.4.4 Other Factors

Several other factors affect the intensity of the diffracted beam. These include :-

a) the multiplicity factor *m*, which is dependent on the symmetry of the crystal lattice and reflects the number of planes in a unit cell with a given d-spacing but different Miller indices.

b) the polarisation factor *p*, which accounts for the fact that X-rays and neutrons are partially polarised on diffraction.

c) the Lorentz factor *L*, is dependent on the measurement technique used and the geometry of the experiment.

2.1.4.5 Rietveld Refinement and Residuals

In a Rietveld refinement, the program minimizes the quantity :-

$$\sum w_i(Y_i-Y_{ci})^2$$

where $w_i=1/Y_i$, the weight for the observed intensity Y_i.
Y_i=Observed intensity at the i'th step,
Y_{ci}=Calculated intensity at the i'th step,
and the sum is over all data points.

The quality of the fit of the model to the experimental data is measured in terms of the residual factors.

The weighted profile

$$R_{wp}=100[\sum_i w_i|Y_i-Y_{ci}|^2/\sum_i w_iY_i^2)]^{\frac{1}{2}}$$

the profile

$$R_p=100[\sum_i |Y_i-Y_{ci}|/\sum_i Y_i]$$

and the expected R-factor

$$R_e=100[N-P+C]/[\sum_i w_iY_i^2]^{1/2}$$

where $N\text{-}P\text{+}C$ is the number of observations - number of variables + number of constraints.

$X^2=R_{wp}^2/R_e^2$ is often used as an indication of the goodness of fit.

The Bragg R-factor reflects the quality of the fit of the integrated intensity data to the experimental data and is given by the expression :-

$$R_{Bragg}=100[\sum_i |I_{obs}-I_{calc}|/[\sum_i I_{obs}]$$

2.2 THERMAL ANALYSIS

Thermal analysis can be defined as the measurement of the changes in physical or chemical properties of a sample as a function of temperature. In particular, thermal analysis generally refers to measurement of enthalpy, heat capacity, mass and thermal expansion. Thermal analysis techniques are widely used in solid state chemistry to study solid state reactions, thermal decomposition and phase transitions.

Thermo-gravimetric analysis (TGA) and differential scanning calorimetry (DSC) were used in this work to investigate phase changes occurring in lithium transition-metal oxides.

2.2.1 Thermogravimetric Analysis

In this technique the change in weight of a sample is measured as a function of temperature or time. A small sample of material (typically a few milligrams) is heated at a constant rate and its weight is monitored continuously and recorded either on a chart recorder or a computer. A decomposition reaction typically appears as a weight loss which extends over a finite time period. The actual weight loss can be determined accurately and related to the chemical processes occurring. The temperatures at which the onset and completion of weight loss occur are dependent on the sample, the heating rate and the atmosphere in which the experiment is performed. The temperatures recorded are therefore related to the experimental conditions and do not necessarily correspond to equilibrium decomposition temperatures.

2.2.2 Differential Thermal Analysis (DTA) and Differential Scanning Calorimetry (DSC)

In differential thermal analysis the presence of a thermal event in a sample is detected by measuring its change in temperature relative to a standard. Typically a pan containing a few milligrams of the sample and a reference pan are placed on a common heating block. The block is heated at a constant rate and the temperature differential between the two pans is measured. Exothermic or endothermic events corresponding to phase changes, melting or solidification of the sample appear as peaks in the DTA trace.

In a DSC experiment the sample and reference pans are maintained at the same temperature throughout the experiment. The additional amount of heat that has to be supplied to the sample or reference pans to achieve this is measured accurately and can be used to calculate the enthalpy changes associated with the reactions.

2.3 CYCLIC VOLTAMMETRY

Cyclic voltammetry is a widely used technique for the study of electroactive species. It is a rapid means of studying the redox behaviour of a sample over a large potential range and is used in organic, inorganic, bio- and electrochemistry. Cyclic voltammetry is extremely useful for the study of intercalation compounds and has been used frequently by other investigators in this field[78-79].

In a cyclic voltammetry experiment the potential of the working electrode is cycled from an initial potential E_i to a potential limit E_1, at a constant rate. When the potential reaches E_1, the scanning direction is reversed and the potential is then changed in the opposite direction until a second voltage limit, E_2 is reached. This sequence can be repeated several times. The typical voltage profile for a cyclic voltammetry experiment is shown in Fig 2.5. The current response of the working electrode is measured and plotted versus the potential to yield a cyclic voltammogram as shown in Fig 2.6.

Cyclic voltammetry experiments require a signal generator to control the potential scan, a potentiostat to control the potential of the electrochemical cell, a current-voltage converter to measure the current generated, and a digital computer or chart recorder to display the voltammogram. A three-electrode cell is generally used. The potentiostat maintains the required potential between the reference electrode and the working electrode (sample of interest). The current is provided between the working electrode and the counter electrode. This arrangement prevents large currents passing through the reference electrode which would affect the potentials measured.

As the potential is changed from its initial value E_i to the upper limit E_1, a point will be reached where the potential is sufficiently high to cause the oxidation of the electroactive species at the electrode surface. The current then increases sharply but the electroactive species is depleted at the surface of the electrode. At some point the mass transport of the electroactive species to the electrode surface becomes rate-limiting and the current reaches a maximum. Thereafter, the current decays as the electrode becomes depleted of the electroactive species. When the scan direction is reversed the sample is reduced and the current for the reverse process is recorded.

If a reaction is reversible, the separation in the peak potentials of the anodic and cathodic peaks ΔE_p will be close to 58/n mV at 25°C, where n is the number of electrons

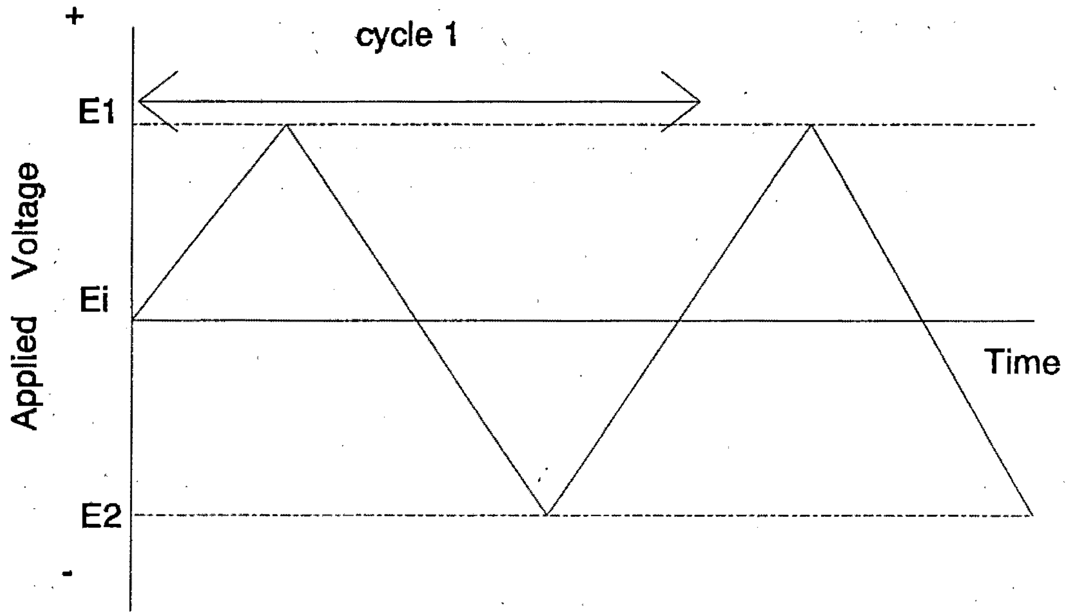

Figure 2.5 : Voltage profile for a cyclic voltammetry experiment

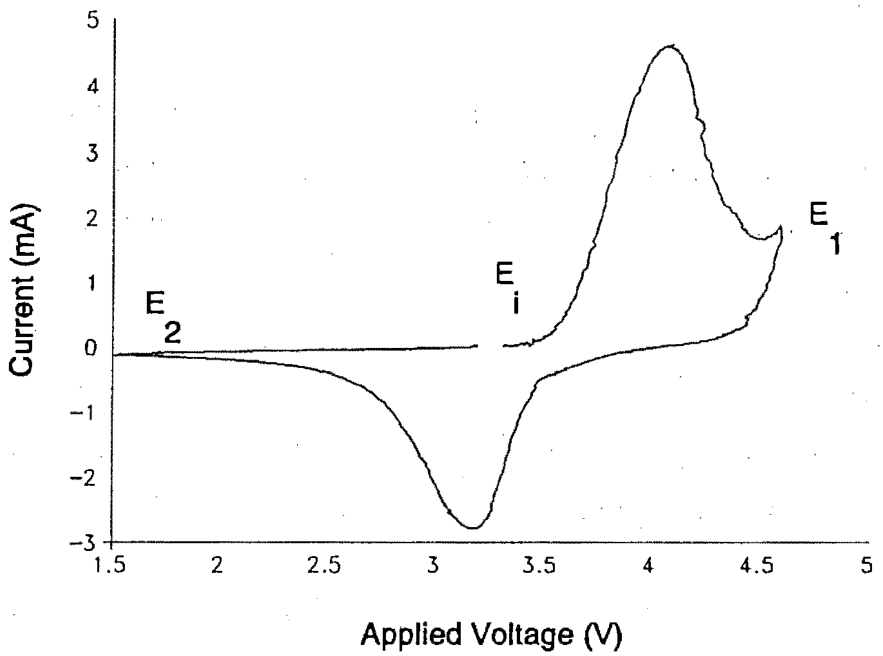

Figure 2.6 : Typical cyclic voltammogram

involved in the redox process. A reaction is termed electrochemically reversible if it is fast enough to maintain the concentrations of oxidised and reduced species in equilibrium with each other at the electrode surface.

The peak current for a reversible reaction is proportional to the square-root of the scan rate

$$i_p \propto \nu^{\frac{1}{2}}$$

where ν = scan rate (V/s), and for a fast, reversible reaction, the peak currents for forward and reverse reactions should be identical.

Most intercalation reactions are, at best, quasi-reversible and the redox peaks shift farther apart with increasing scan rate. Cyclic voltammetry of intercalation compounds can give information on :-

a) The number of steps involved in a reaction
b) The reversibility of the reactions occurring
c) The electrochemical potentials at which oxidation and reduction reactions occur
d) Some indication of the kinetics of the reactions

Cyclic voltammetry has the advantage of taking a fairly short time compared to, for example, galvanostatic cycling of intercalation compounds and is therefore a useful screening test for new materials.

In recent years the potentiodynamic step technique has been developed which can give greater resolution of phase changes and different reactions occuring during intercalation[80]. In this technique the voltage is changed in steps of typically 0.1 V over a specific range. At each step the current is measured until it decays to below a minimum value when the voltage is again incremented. The current is integrated for each voltage step and is plotted versus the voltage. The data thus obtained is equivalent to a very low rate cyclic voltammetry experiment but can be performed in a comparatively short time.

2.4 OPEN CIRCUIT VOLTAGE (OCV) CURVES

In a typical lithium intercalation cell the anode reaction can be described by :-

$$Li \rightarrow Li^{+} + e$$

and the cathode reaction by :-

$$ne + nLi^{+} + H \rightarrow Li_{n}H$$

where ***H*** is the host lattice e.g. MX_n. When ***n*** lithium ions are reacted with the host structure, the total charge transferred is ***ne***. The work done is

$$W=-\Delta G$$

where ***ΔG*** is the free energy change of the reaction and therefore:

$$\Delta G=-neE$$

or for molar quantities,

$$\Delta G=-nFE$$

where ***E*** is the open circuit voltage of the cell.

In the case of an intercalation reaction however, ***ΔG*** is also given by:-

$$\Delta G=(\mu_m(H)-\mu_m(Li))n$$

where $\mu_m(H)$ is the chemical potential of the Li atoms in the host lattice e.g. Li_xMX_n and $\mu_m(Li)$ the chemical potential of Li atoms in the metal. Thus

$$E=-\frac{(\mu_m(H)-\mu_m(Li))}{F}$$

for 1 mole of electrons. Since the chemical potential of the Li atoms in the metal is constant, the open-circuit voltage of the cell can be directly related to the chemical potential of the Li atoms in the host.

In practice, the open-circuit-voltage curves are recorded by charging/discharging an electrochemical cell to a known composition and allowing the voltage to equilibrate. This process is repeated several times to characterise the full composition range.

Since

$$\Delta G = -SdT + VdP,$$

it follows that

$$(\frac{\partial G}{\partial T})_P = -\Delta S$$

or

$$(\frac{\partial E}{\partial T})_P = \frac{\Delta S}{nF}$$

and

$$(\frac{\partial G}{\partial P})_T = \Delta V$$

or

$$(\frac{\partial E}{\partial P})_T = -\frac{\Delta V}{nF}$$

Open circuit voltages can have either positive or negative temperature coefficients depending on the sign of the entropy change associated with the cell reaction. For cell reactions involving only the solid state, the temperature coefficient is generally small and the voltage is virtually independent of applied pressure.

Under certain circumstances the open circuit voltage curves of electrochemical cells exhibit plateaus over certain composition ranges. This can be explained by consideration of the Gibbs phase rule :-

$$P + F = C + 2$$

where P is the number of phases present in equilibrium

F is the number of degrees of freedom or independent variables

and C is the number of components needed to describe the system.

For example, in the case of lithium intercalation into $LiMn_2O_4$, the reaction

$$xLi + LiMn_2O_4 \rightarrow xLi_2Mn_2O_4 + (1-x)LiMn_2O_4$$

has P=2 ($LiMn_2O_4$ and $Li_2Mn_2O_4$) and C=2 (Li and Mn_2O_4) i.e. F=2 (pressure and temperature). Under conditions of constant temperature and pressure, the voltage is therefore independent of the composition, giving rise to a plateau in the OCV (open-circuit-voltage) curve.

On the other hand in the reaction

$$xLi + TiS_2 \rightarrow Li_xTiS_2$$

the product is a solid solution for $0<x<1$ i.e P=1 (Li_xTiS_2) and C=2 (Li and TiS_2) i.e F=3 (temperature, pressure and composition), thus the voltage varies with the composition.

2.5 GALVANOSTATIC CYCLING AND POLARISATION

The OCV of an electrochemical cell gives information on the behaviour of the cell under conditions of zero current flow. However in order to determine the performance of a practical cell, a clear understanding must also be obtained of the change in the cell voltage when a finite current is drawn. The cells examined in this study were both charged and discharged under conditions of constant current i.e. galvanostatically.

The difference in potential between the OCV and the voltage under conditions of constant current flow is termed the polarisation.

For a discharge : $E_{cell} = E_{ocv} - E_{pol}$

and for a charge : $E_{cell} = E_{ocv} + E_{pol}$

The polarisation is the combined effect of several different factors.

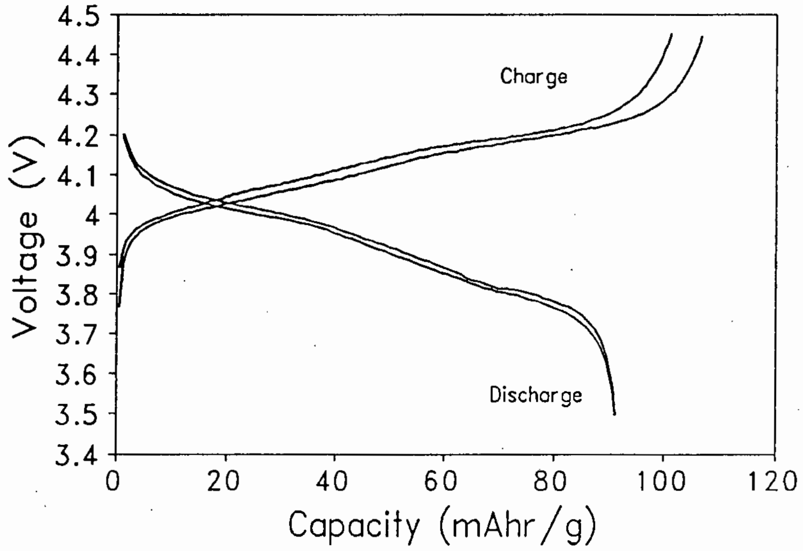

Figure 2.7 : Typical galvanostatic cycling curves of a rechargeable electrochemical cell (2 cycles).

2.5.1 Ohmic or "iR" losses

Ohmic losses are a result of the finite resistances of the electrolyte, separators and sometimes of the electrodes themselves. These effects are minimised by using high conductivity electrolytes, reducing the resistivities of electrodes e.g. by the addition of conductive diluents like carbon black and by optimising the cell geometry.

2.5.2 Overvoltage

Overvoltage is the difference in potential of an electrode when a finite current is flowing and when no current is flowing i.e.

$$\eta = E - E_{eq}$$

An electrode process is determined by charge transfer, interfacial reactions and mass transport of the electroactive species. All these factors contribute to the overpotential of the electrode. In practice, one particular process tends to be rate-limiting and largely determines the overvoltage. In intercalation electrodes at moderate current rates it is generally accepted that the rate-limiting process is the mass transport of the metal ions in the host lattice.

Fig 2.7 shows typical cycling curves for two cycles of an electrochemical cell recorded under conditions of constant current. The voltage difference between the charge and discharge curves gives a measure of the cell polarisation and this increases with increasing current density. The x-axis is typically expressed in specific capacity (mAhr/g) or alternatively in terms of the composition of the cathode. Repeated cycling of electrochemical cells gives an indication of the reversibility of the electrochemical reactions and is used to predict the performance of the cells in practical applications.

2.6 LITHIUM ION DIFFUSION RATES

The maximum current that can be drawn from an electrochemical cell containing an intercalation electrode is ultimately limited by the diffusion coefficient of the electroactive species in the host lattice. For high power applications a fast diffusion rate is required.

Measurement of Li ion diffusion rates in intercalation electrodes has been carried out by several investigators[15-19,81-83]. Many different techniques have been used and it is generally agreed that it is difficult to obtain values of the diffusion rate with a high degree of accuracy. Different methods applied to the same material have yielded reported diffusion rates which differ by as much as two orders of magnitude.

The diffusivity, which is identical to quantities which are called the component-, elementary- or self-diffusion coefficient, is a measure of the random motion of the particles of species n in the absence of a concentration gradient.

$$D_n = b_n kT$$

where b_n is the general mobility of species n (drift velocity per unit force) and k is

Boltzmann's constant.

In the presence of a concentration gradient, the diffusion of the electroactive species is enhanced by a factor K_T, the thermodynamic or Darken factor.

$$K_T=\frac{\partial \ln a_n}{\partial \ln c_n}$$

where a_n = the activity of species n and c_n is the concentration of species n.
The chemical diffusion coefficient is a combination of the diffusivity and the thermodynamic factor:-

$$\tilde{D}=D_n\frac{\partial \ln a_n}{\partial \ln c_n}$$

The chemical diffusion coefficient is the quantity that is determined directly by electrochemical measurement techniques.

The chemical diffusion coefficient of lithium ions in intercalation compounds can be measured by either AC or DC techniques.

2.6.1 DC Techniques

The most commonly used DC technique is the galvanostatic pulse technique. A short current pulse is applied to an electrochemical cell and the variation of the voltage is recorded as a function of time as the cell equilibrates. This technique was originally applied by Basu and Worrall to measure the Li ion diffusion rates in Li_xTaS_2 and Li_xTiS_2[81].

This technique is limited by several factors, namely :-

1) The electrode surface area has to be known accurately. For polycrystalline samples the active surface area is not necessarily equivalent to the geometric surface area but this is generally used as an approximation.

2) Fairly large local surface concentration of the mobile ions are sometimes applied which may result in local time-dependent variations in the enhancement factor and the chemical diffusion coefficient of the sample.

Honders and Broers[84] developed a variation of the galvanostatic pulse technique which uses very small currents for long times. Their technique also enables, under certain conditions, the simultaneous measurement of the chemical diffusion coefficient and the thermodynamic factor. This removes the need for knowledge of the shape of the OCV curve versus composition which is a possible source of error. Their technique also involves a measurement of the effective length of the diffusion path (i.e. the sample length) as opposed to the active surface area. As this can be determined with greater accuracy, the results are considered to be more reliable than those obtained by the Basu and Worrall technique.

The Galvanostatic Intermittent Titration Technique (GITT)[85] is another variation of the galvanostatic pulse technique which can be used to study the variation of the chemical diffusion coefficient with composition. A galvanostatic current pulse is applied to the electrochemical cell for a time τ and the voltage change as a function of time is recorded. This also results in a small change in stoichiometry and equilibrium cell voltage. If the voltage transient follows a square root of time law then the diffusion coefficient can be determined from the equation :-

$$\tilde{D}=\frac{4}{\pi\tau}(\frac{m_B V_M}{M_B S z})^2(\Delta E_s/\Delta E_t)$$

where

m_B = mass of species B

M_B = molecular weight of species B

τ = duration of pulse

S = contact area between sample and electrolyte

z = charge number

V_M = molar volume

$\Delta E_{s/t}$ = change of steady-state equilibrium and transient voltage

2.6.2 AC Impedance Technique

The AC impedance technique for the measurement of Li ion diffusion rates involves the application of a sinusoidal voltage to the electrochemical cell and the measurement of the resulting sinusoidal current. The frequency of the AC signal is varied over a wide range, typically 10^5 Hz - 1 mHz.

The AC response of a simple electrochemical cell can be described by the equivalent circuit shown in Fig 2.8. The Warburg impedance Z_x^* represents the impedance resulting from diffusion of the electroactive species and is given by:-

$$Z_\omega^* = A\omega^{-\frac{1}{2}} - jA\omega^{-\frac{1}{2}}$$

where ω = angular frequency

$j = \sqrt{-1}$

and A is a constant given by :-

$$A = \frac{V_M(\partial V/\partial x)}{\sqrt{2}zF\tilde{D}^{\frac{1}{2}}a}$$

where V_M = molar volume

$\partial V/\partial x$ = slope of OCV vs composition curve

F = Faraday's constant

a = electrode area

Fig 2.9 shows a typical plot of imaginary versus real impedance (complex plane representation) for the circuit illustrated in Fig 2.8. For diffusion controlled kinetics, the slope of the low frequency tail should be 45° [86].

AC impedance techniques typically use a very small perturbation voltage (10 mV-rms AC perturbation) which means that the system is maintained very close to equilibrium during a measurement. The other advantage of AC impedance is that it enables the separation

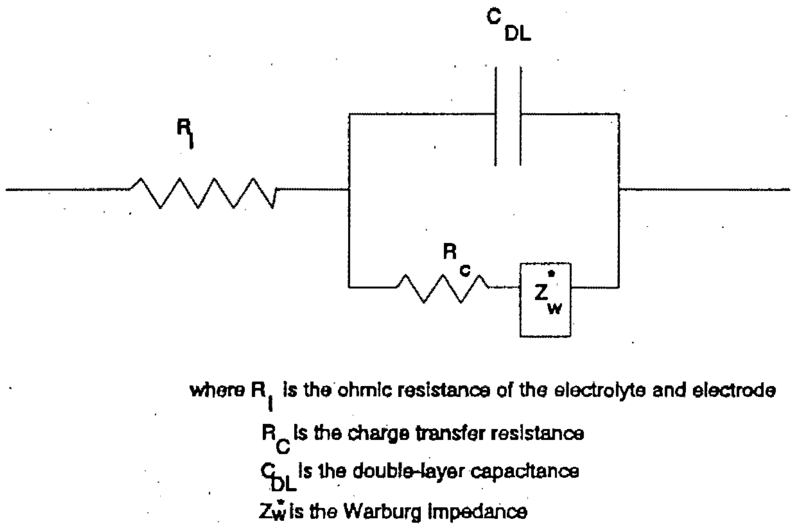

Figure 2.8 : Randles equivalent circuit for an electrochemical cell[87].

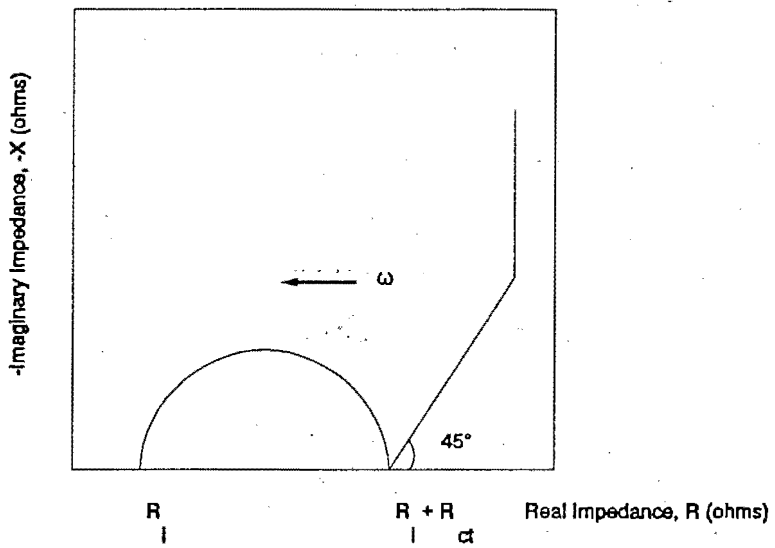

Figure 2.9 : Ideal complex plane impedance plot for an electrochemical cell.

of various effects which may complicate the Li ion insertion reaction e.g. formation of a surface layer on the electrode due to electrolyte decomposition.

The main drawback of AC impedance is that the interpretation of the spectra may be difficult for complex systems where the simple circuit of Fig 2.9. does not adequately describe the observed response.

CHAPTER 3

EXPERIMENTAL METHODS

This chapter gives general details of experimental methods used in this work for electrochemical evaluation, chemical insertion and removal of lithium, thermal analysis, diffusion rate determination and diffraction techniques. Specific details regarding individual sections of the work are given in the relevant chapters.

3.1 DIFFRACTION TECHNIQUES

3.1.1 Powder X-ray diffraction

Powder X-ray diffraction patterns were recorded on an automated Rigaku powder diffractometer using CuKα radiation monochromated with a graphite single crystal. Lattice parameters were determined against an internal Si standard using a least-squares method. Structure determinations were carried out using either the Wyriet program for Rietveld analysis[88,89] of X-ray powder diffraction data adapted for an IBM compatible personal computer or the Wiseman intensity refinement program[90]. Simulated X-ray powder diffraction patterns were generated using the Lazy Pulverix program[91]. X-ray samples were prepared by pressing approximately 100mg of sample material onto a glass slide covered by a thin layer of silicon vacuum grease.

3.1.2 Powder neutron diffraction

Time of flight powder neutron diffraction data were obtained at the Rutherford Appleton Laboratory in the U.K. The POLARIS high intensity diffractometer situated on the S1 beam line at ISIS was used. ISIS produces neutron pulses at a repetition rate of 50 Hz which are exploited in ISIS instruments by using the time-of-flight technique to measure neutron wavelengths. The instrument is situated 12 m from the ambient water moderator. Three ^3He detector banks simultaneously collect data at backscattering angles ($\Delta d/d \sim 5 \times 10^{-3}$), 90° ($\Delta d/d \sim 6 \times 10^{-3}$) and at low angles ($\Delta d/d \sim 6 \times 10^{-2}$).

The structures were refined with a profile refinement program modified to describe peak shape by a double-decay exponential convoluted with a Voigt function[92,93]. Neutron scattering amplitudes used in the refinements are listed in reference 94.

3.2 THERMAL ANALYSIS

DSC and DTA data were recorded on the Perkin Elmer instrument at the Chemistry Department, University of Cape Town. The temperature was scanned at a rate of 20°C/min and experiments were performed either in air or under a N_2 flow of 50 ml/min.

3.3 CHEMICAL LITHIATION AND DELITHIATION REACTIONS

3.3.1 Lithiation with LiI

In the past lithiation of transition-metal-oxides has commonly been carried using n-butyllithium[95-97]. This is an effective technique in many cases but n-butyllithium is highly reducing and the products with it have been found to be unstable in contact with the atmosphere. In addition the reaction has to be carried out under an inert atmosphere.

An alternative technique for lithiation of transition metal oxides is to use LiI as a lithiating agent. This system has been used successfully for $LiMn_2O_4$ spinels.[98] The chemistry of LiI in acetonitrile has been studied in detail[99]. The oxidation of I^- to I_2 occurs in two reversible steps:-

$$6I^- - 4e^- \rightarrow 2I_3^- : E_1^\circ \approx 3.0V \ vs \ Li/Li^+$$
$$2I_3^- - 2e^- \rightarrow 3I_2 : E_2^\circ \approx 3.7V \ vs \ Li/LI^+$$

Electrochemical insertion of Li into the spinel $LiMn_2O_4$ occurs at an open circuit voltage of close to 3 V versus Li/Li^+. The reduction of $Li_2Mn_2O_4$ by LiI occurs according to the following reaction:-

$$LiMn_2O_4 + 3x/2\ LiI \rightarrow Li_{1+x}Mn_2O_4 + x/2\ LiI_3$$

The reducing voltage of the (I_3^-/I^-) system was lowered below 3 V by varying the temperature and concentration of the starting species according to the Nernst equation[100] :-

$$E = E_1^{\circ} + RT/2F \log[I_3^-]/[I^-]^3$$

The complete reduction of $LiMn_2O_4$ to $Li_2Mn_2O_4$ was found to be possible using 1g of $LiMn_2O_4$ in 50 ml acetonitrile with a 6x excess of LiI. The mixture was heated in air under reflux to the boiling point of acetonitrile (82°C) for 3-4 hours. The product was filtered, washed repeatedly with acetonitrile to remove all traces of LiI and dried in air at 80°C.

Stoichiometric quantities of LiI were used if products of a specific composition were required.

3.3.2 Lithiation by reaction in a reducing atmosphere

Direct reaction of a lithium transition metal oxide with a lithium salt in a reducing atmosphere can produce a lithiated product. This technique was used to produce lithiated manganese oxides.

Samples of lithium manganese oxide ($LiMn_2O_4$) or manganese oxide (MnO_2) and lithium salt ($LiOH.H_2O$) were mixed in the required ratio (typically ball-milled in hexane). The resulting powder was then either heated in a tube furnace under H_2 or mixed with carbon (acetylene black) and heated under argon. Heating temperatures varied from 250°C - 620°C depending on the nature of the starting material. The apparatus used is illustrated in Fig 3.1. The sample was placed in a glass U-tube and a continuous flow of either hydrogen or argon gas was passed over the sample. The temperature was monitored by a thermocouple placed directly above the sample.

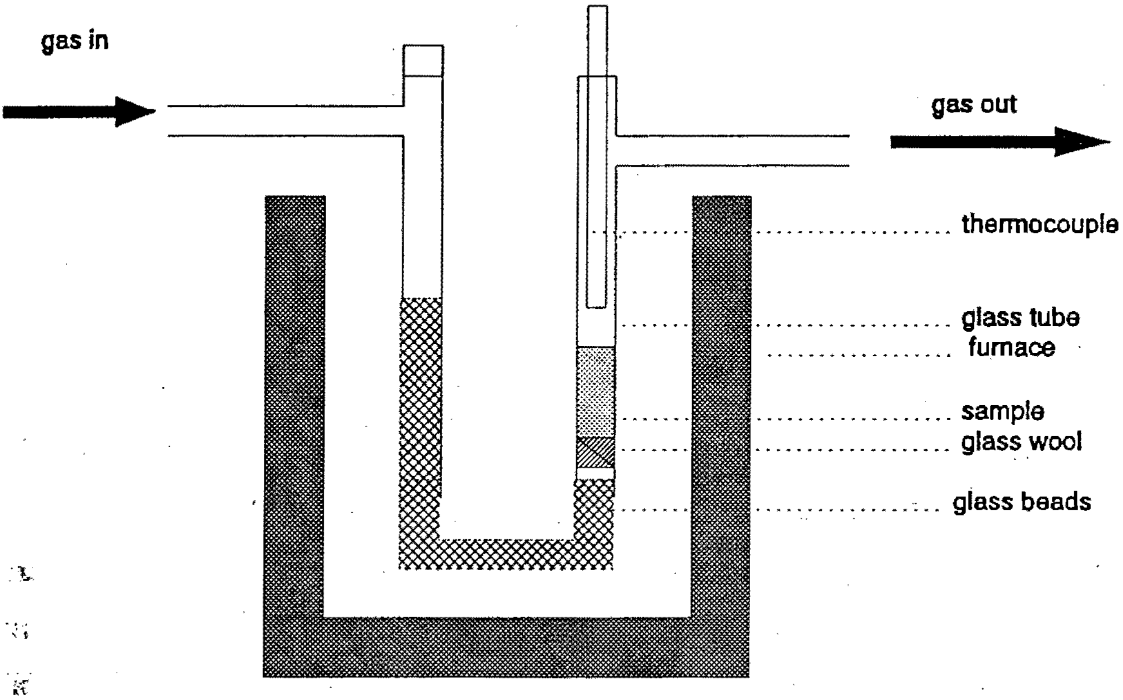

Figure 3.1 : Apparatus used for the lithiation of lithium manganese oxides in a reducing atmosphere.

3.3.3 Lithium extraction by acid treatment

Lithium was extracted from lithium transition metal oxides using H_2SO_4 according to the method described by Hunter[101]. Typically 1 g of the sample was added to 15 ml of H_2O with 1-5 ml of 5N H_2SO_4. The sample was stirred vigorously at room temperature for several hours to a few days depending on the final lithium concentration required.

The solid product was filtered, washed with water and dried in a drying oven. Lithium concentrations in the products were determined by atomic absorption spectroscopy.

3.4 ELECTROCHEMICAL METHODS

3.4.1 Electrochemical Cells

For all electrochemical methods the cells used were glass prismatic-type cells with either two or three electrodes (Fig 3.2). Two-electrode cells were used for galvanostatic cell cycling and open circuit voltage curve determinations. Three-electrode cells were used for AC impedance measurements of diffusion rates and for cyclic voltammetry experiments.

The cell consists of a glass body and a glass lid with a ground glass seal between them. The electrodes pass through the lid and are sealed into position with an epoxy resin. The anode and cathode current collectors are formed from stainless steel gauze. Lithium foil (Lithco) is pressed onto the current collectors to form the anode and reference electrodes (in the case of a three-electrode system). The cathode material was mixed with a conductive additive (acetylene black) and a binder to form the cathode mix.

Two different binders were used : teflon and ethylene propylene diene monomer (EPDM).

Teflon and acetylene black were mixed in a 1:2 mass ratio in a mortar and pestle. The cathode mix consisted of 20% by mass of this mixture and 80% of the active cathode material mixed in hexane in a mortar and pestle.

Alternatively, EPDM was dissolved in cyclohexane. A mixture of acetylene black and cathode material were added to the EPDM solution and the mixture was stirred. The cyclohexane was evaporated off and the mixture was sieved. The mass ratio of active material:AB:EPDM was typically 92:5:3 although this was optimised for the particular active material used.

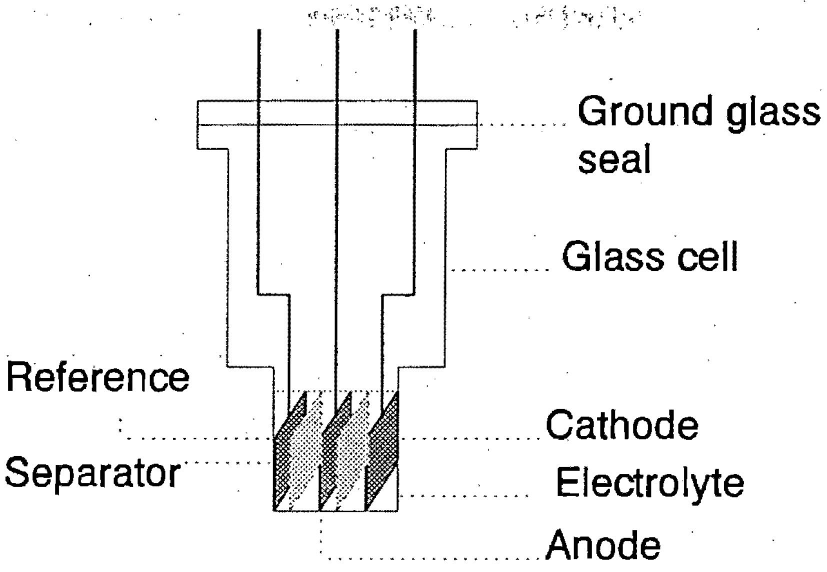

Figure 3.2 : Schematic diagram of an electrochemical cell.

Approximately 20mg of cathode mixture was pressed onto the ~1 cm^2 cathode current collectors at 30-60 kN to form the cathodes. The separators used were Cellgard microporous polypropylene grades 2400 or 3401.

3.4.2 Electrolytes

Two different electrolytes were used in this work : 1M $LiClO_4$ in propylene carbonate and 1M $LiClO_4$ in a 1:1 mixture of propylene carbonate (PC) and dimethoxyethane (DME).

The propylene carbonate was either used as received (Aldrich, 99% +, < 50 ppm H_2O) or dried over 4 Å molecular sieves and then distilled under vacuum (Aldrich, 99%). The DME (Merck, >99%) was refluxed over Na balls and then distilled under argon. The $LiClO_4$ (Merck GR or Aldrich) was dried under vacuum at 200°C for several hours. The electrolytes were made up and stored in a glove box under an argon atmosphere.

3.4.3 Cyclic Voltammetry

Three electrode cells assembled under an argon atmosphere were used for cyclic voltammetry experiments, with lithium metal as the reference and counter electrodes.

The working electrode was formed by pressing ~ 5-10 mg of the cathode mixture onto the cathode current collector. The electrolyte used for the cyclic voltammetry experiments was 1M $LiClO_4$ in 1:1 PC:DME.

The experiments were carried out using a Princeton Applied Research (PAR) model 173 potentiostat, linked to a PAR model 175 Universal Programmer. The data were recorded via an A/D converter card on a personal computer. The scan rates were varied between 0.1 mV/s and 1.0 mV/s.

3.4.4 Galvanostatic Cell Cycling

Two-electrode cells were used in the determination of all galvanostatic charge and discharge curves. The cells were assembled and cycled under an argon atmosphere. Cells were cycled galvanostatically using a custom built 16-channel cell cycler. Charge and discharge currents in the range 0.02-0.4 mA/cm^2 were used and the cells were cycled between preset upper and lower voltage limits. The voltage-time data were recorded continuously on a personal computer during cycling. A representative number of cells were tested to ensure reproducibility.

The theoretical specific capacity of the working electrodes is given by :-

$$\textit{Theoretical Specific Capacity} = \frac{F \ \Delta x}{M} \frac{1000}{3600} \ (mAh/g)$$

The specific capacity of the working electrode was calculated using the mass of active material in the cathode according to :-

$$\textit{Specific Capacity}\ (mAhr/g) = t(hrs)\ I(mA)\ /\ m(g)$$

where t = charge or discharge time, I = Current

M = Molar mass of active material

m = mass of active material

Δx = the change in the lithium content of the cathode Li_xMX_n

F = Faraday's constant

The lithium content of the cathode, x in Li_xMX_n, during cycling was calculated as :-

$$x = \frac{\text{Specific capacity}}{\text{Theoretical specific capacity}}$$

3.4.5 Open Circuit Voltage Data

Open circuit voltage (OCV) data were recorded using two electrode cells. The cells were charged or discharged galvanostatically at $20\mu A/cm^2$ for a predetermined time interval and then allowed to equilibrate until a stable voltage was reached. This process was repeated to characterise the full electrochemical curve.

Generally the counter electrode used was lithium foil but in the case of $LiCo_{0.9}Ni_{0.1}O_2$ the counter electrode was $LiMn_2O_4$. $LiMn_2O_4$ is suitable as a counter electrode for OCV measurements as it discharges at a constant voltage of 3.0V versus lithium over the composition range $0.06<x<1$ in $Li_{1+x}Mn_2O_4$. The overall voltage of the cell is reduced to fall within the electrolyte stability window of commonly used electrolytes reducing the risk of cell degradation during the long times needed to record OCV data.

3.4.6 AC Impedance Determination of Diffusion Rates

AC impedance measurements were carried out using a Solartron 1286 potentiostat and a 1255 frequency response analyzer. Both instruments were controlled by an IBM-compatible personal computer. Data were collected over the frequency range 10^{-3}-10^5 Hz using a 10 mV-rms AC perturbation. Chemical diffusion coefficients were calculated using the geometric surface area of the cathode as an approximation of the electrochemically active surface area. No acetylene black or binder was used in the cathodes to avoid any further source of error in the surface area determination. Approximately 5mg of active cathode material was pressed onto the stainless steel current collector at 30 to 60 kN to form the cathodes.

3.5 PARTICLE SIZE AND SURFACE AREA DETERMINATION

The particle size distributions were determined using a Leeds and Northrup Microtrac small particle analyzer. The suspension was dispersed ultrasonically before analysis.

BET surface areas were determined with a Micromeritex All Surface Area Analyzer. Samples were outgassed overnight and surface areas were determined using nitrogen gas at liquid nitrogen temperatures. Nitrogen gas is commonly used as a probe for surface area analysis and was used for all the surface area determinations in this work. However, it is recognised that the use of other gases as probes may give slightly different results in surface area determinations.

CHAPTER 4

LITHIUM COBALT OXIDES

4.1 INTRODUCTION

$LiCoO_2$ is typically synthesised at 800-900°C from oxide or carbonate precursors and is characterised by the trigonal space group $R\bar{3}m$[53,60]. The lithium and cobalt cations are essentially perfectly ordered into alternate layers of octahedral sites between the distorted cubic close packed oxygen planes.

The use of Li_xCoO_2 as an insertion electrode for lithium batteries was first proposed by Mizushima, Jones, Wiseman and Goodenough in 1980[62]. Due to the high oxidation potential of the Co^{3+}/Co^{4+} couple, this electrode offers the possibility of a secondary lithium cell with an average discharge voltage of approximately 4.0V. While this is an advantage from the point of view of the specific energy density of cells, the high voltages reached on charge are outside the stability window of many commonly used electrolytes. This prevented the immediate exploitation of Li_xCoO_2 as a cathode for lithium batteries. However continued research into alternative electrolytes and the use of carbon anodes has led to improvements in the performance of secondary cells using Li_xCoO_2 and SONY have recently introduced a trial product onto the market[11,66].

Synthesis of intercalation cathodes at moderate temperatures (300-450°C) typically results in products with smaller particle size and modified structure compared to the high temperature analogues. Recent research in the Li-Mn-O system has shown that electrodes with modified structures prepared at 350°C offer significantly better performance than their high-temperature analogues in rechargeable lithium cells[49,102-106]. In order to determine the effect of synthesis temperature on the structure and electrochemistry of $LiCoO_2$, a detailed study using synthesis temperatures of 400°C was initiated. In this chapter we report on the structural and electrochemical properties of $LiCoO_2$ prepared at 400°C.

4.2 EXPERIMENTAL

The standard, high temperature $LiCoO_2$, which will be referred to as HT-$LiCoO_2$, was prepared by heating a stoichiometric mixture of Li_2CO_3 (SAARCHEM) and $CoCO_3$ (BDH) in air at 900°C for 24 hours. The material was removed from the furnace, ground in a pestle and mortar and heated for a further 24 hours.

"Low temperature" $LiCoO_2$, which will be referred to as LT-$LiCoO_2$, was prepared at 400°C by reacting stoichiometric quantities of Li_2CO_3 and $CoCO_3$. Initially, the powders were thoroughly mixed in hexane in a pestle and mortar or alternatively ball-milled in hexane and thereafter heated in air at 50°C per hour to 400°C. The temperature was held at 400°C for approximately one week to form a single-phase LT-$LiCoO_2$ product.

Samples of LT-$LiCoO_2$ were also heated in air at 600°C and 900°C to investigate the stability of the low temperature phase.

Lithium was removed from $LiCoO_2$ both chemically and electrochemically. Chemical extraction was performed by adding 1g of $LiCoO_2$ to 15 ml H_2O and 1-5 ml of H_2SO_4 according to the reaction:-

$$2\ LiCoO_2 \rightarrow 2\ Li_{1-x}Co_{1-x/2}O_{2-x} + x\ Li_2O + x\ CoO \qquad 0 \leq x \leq 1$$

The samples were stirred continuously at ambient temperature for one hour to one week depending on the final lithium concentration required. The solution became pink indicating the partial dissolution of the cobalt ions. The samples were washed with H_2O and dried in air at 80°C for 48 hours. Lithium concentrations in delithiated samples were determined by atomic absorption spectroscopy. Lithium contents below $Li_{0.3}CoO_2$ could not be obtained by acid treatment.

Electrochemical delithiation was performed using 2-electrode prismatic cells with a 1M solution of $LiClO_4$ in propylene carbonate as electrolyte. The cathode consisted of 20-30 mg of $LiCoO_2$ compacted onto a stainless-steel grid and the anode was formed from lithium foil pressed onto a stainless-steel current collector. The cells were charged at a constant current of 20 microamps for the required length of time and thereafter allowed to equilibrate until a stable voltage was reached. (3-7 days)

Galvanostatic cell-cycling data were recorded using the method described in section 3.5.4. The cathode mixture used consisted of 80% by mass of active material and 20% of a 1:1 mixture of teflon and acetylene black. About 20 mg of the cathode mixture was pressed onto the stainless steel current collectors at 30 kN to form the cathodes.

The cyclic voltammetry experiments were performed as described in section 3.5.6.

4.3 RESULTS

4.3.1 X-ray Diffraction Data of LT-$LiCoO_2$

Characteristic X-ray diffraction profiles of HT-$LiCoO_2$ and two samples of LT-$LiCoO_2$ are shown in Figs. 4.1 (a -c) for the range $10° \leq 2\theta \leq 80°$. The LT-$LiCoO_2$ samples were initially indexed to a trigonal unit cell, (space group $R\bar{3}m$), by analogy with HT-$LiCoO_2$[53].

Table 4.1 shows the lattice parameters and *c/a* ratios obtained from a least squares refinement of the peak positions in the X-ray diffraction patterns. The lattice parameters of the HT-$LiCoO_2$ sample agree well with those reported in the literature (a= 2.8166(1)Å, c=14.052(1)Å[53]). It can be seen from Table 4.1 that the *c/a* ratios of LT-$LiCoO_2$ samples are 4.903(3) and 4.900(2), significantly different from that of HT-$LiCoO_2$ (c/a=4.989(1)). A *c/a* ratio of $\surd 24$=4.899 is the ideal ratio obtained when the oxygen anion lattice adopts cubic close packed symmetry.

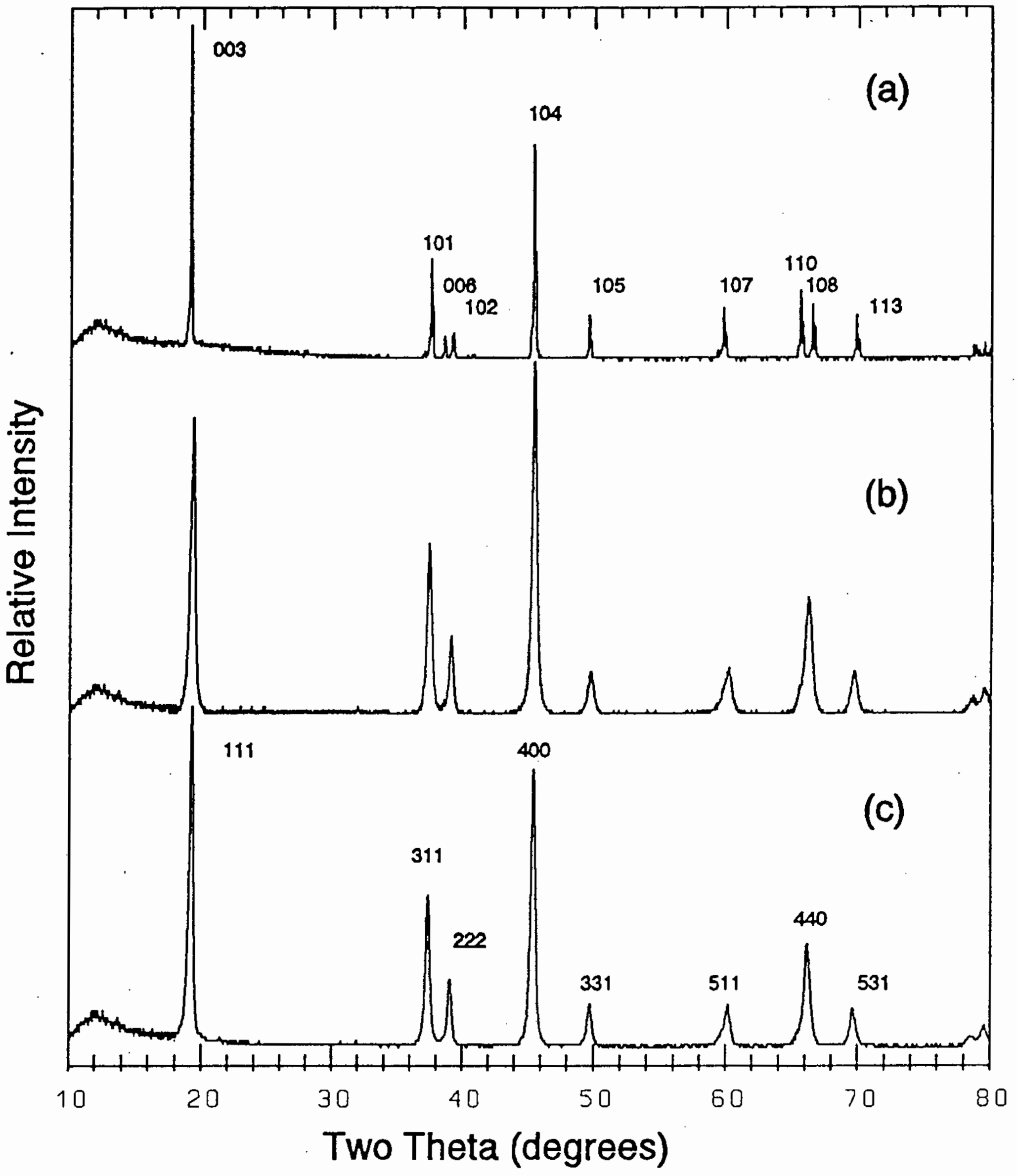

Figure 4.1 :Powder X-ray diffraction patterns of a) HT-$LiCoO_2$ (indexed to a trigonal unit cell), b)LT-$LiCoO_2$(Sample A) and c) LT-$LiCoO_2$(SampleB)(indexed to a fcc unit cell).

The *c/a* ratio of ~4.90 in LT-$LiCoO_2$ results in the overlap of several peaks in the X-ray diffraction pattern which are well-separated in HT-$LiCoO_2$, for example, the (0 0 6) and (1 0 2) and the (1 0 8) and (1 1 0) reflections (Fig. 4.1(a-c)).

There are also significant variations in the relative intensities of some of the peaks in HT-$LiCoO_2$ and LT-$LiCoO_2$, for example, the (003) and (104) reflections, which suggests that the cobalt ions adopt a different arrangement in the structures of the high-temperature and low-temperature compounds. This hypothesis is based on the fact that cobalt is a significantly heavier atom than lithium and is therefore a considerably stronger scatterer of X-rays. Any large change in the relative intensities of X-ray diffraction peaks is therefore most likely to be due to rearrangement of the cobalt ions.

TABLE 4.1

Lattice Parameters of HT-$LiCoO_2$ and LT-$LiCoO_2$

SAMPLE	*a* (Å)	*c* (Å)	*c/a*
HT-$LiCoO_2$	2.818(1)	14.060(1)	4.989(1)
LT-$LiCoO_2$ (Sample A)	2.830(1)	13.875(8)	4.903(3)
LT-$LiCoO_2$ (Sample B)	2.830(1)	13.868(4)	4.900(2)

As a consequence of the cubic symmetry of the LT-$LiCoO_2$ lattice and the resulting peak overlap, the X-ray diffraction patterns may also be indexed to the spinel space group Fd3m by analogy with the lithiated spinel $Li_2Ti_2O_4$. In this structure the lithium cations fully occupy the 16c octahedral sites and the titanium cations fully occupy the 16d octahedral sites of the spinel space group[107]. This alternative indexing is illustrated in Fig. 4.1(c).

The peaks in the X-ray diffraction patterns of LT-$LiCoO_2$ are significantly broader than those of HT-$LiCoO_2$. A similar trend in line broadening with temperature has been observed for Li-Mn-O spinels synthesised at 300°-500°C for X-rays[49,108] and neutrons[72] and can possibly be attributed to a scatter of interplanar spacing in the diffracting volume, usually described as strain.

4.3.2 Physical properties

The physical properties of the 400°C and 900°C products also differ significantly. Fig 4.2 and Table 4.2 show the particle size distribution and BET surface area of the two samples respectively. A significantly smaller particle size and larger surface area is found for the low temperature material. The colours of the two samples also differ. The LT-$LiCoO_2$ samples are dark brown compared to the blue-black colour of the high temperature material.

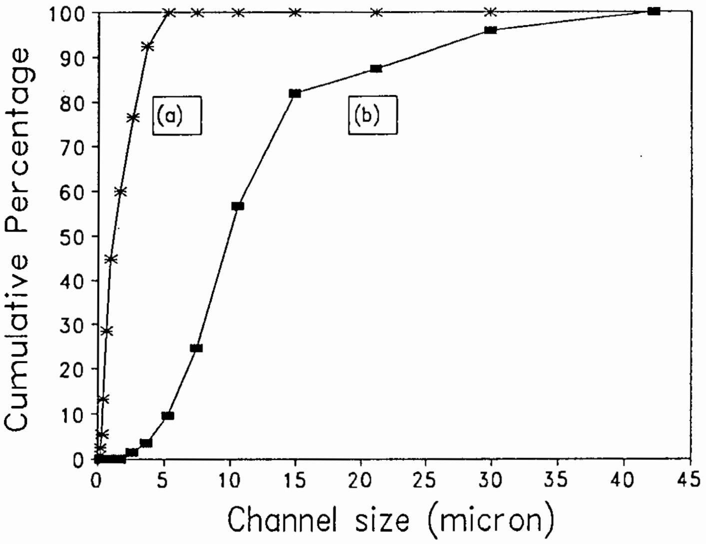

Figure 4.2 : Particle size distribution of (a) LT-$LiCoO_2$ and (b) HT-$LiCoO_2$

TABLE 4.2
Specific Surface Areas of HT-$LiCoO_2$ and LT-$LiCoO_2$

SAMPLE	SPECIFIC SURFACE AREA (m^2/g)
HT-$LiCoO_2$	0.7
LT-$LiCoO_2$	18.7

4.3.3 X-ray Diffraction Data of Delithiated LT-Li_xCoO_2 Samples ($1>x\geq0.3$)

Figs 4.3 (a-f) show X-ray diffraction patterns for several samples of delithiated LT-$LiCoO_2$. The samples in Fig 4.3 (a-e) were obtained by chemical delithiation (acid leaching), while that in Fig 4.3 (f) was obtained by electrochemical delithiation. Fig 4.4 (a and b) show the results for HT-$LiCoO_2$ delithiated chemically and Fig 4.4 (c) shows an electrochemically delithiated HT-Li_xCoO_2 sample. The sample in fig 4.4(c) shows enhanced intensities for (0 0 l) peaks due to preferential orientation as a result of the uniaxial pressure applied in the preparation of cathodes. Table 4.3 shows the lattice parameters and *c*/*a* ratios obtained by least squares refinement of the peak positions of LT-Li_xCoO_2 and HT-Li_xCoO_2 respectively. All samples were prepared by acid-leaching except where otherwise indicated.

In LT-Li_xCoO_2 samples, Table 4.3 shows that there is only a small change in the *a* and *c* lattice parameters on delithiation and that the *c*/*a* ratio remains constant at ~4.90 during this process maintaining the near-cubic symmetry. The intensity ratio of the (101)/(104) peaks of the $R\bar{3}m$ space group increases continuously as the lithium content decreases. In contrast, for HT-$LiCoO_2$, the *c*-axis expands rapidly on delithiation[109]. This can be seen, for example, from the increase in the separation of the (110) and (108) peaks on delithiation (Fig 4.4).

Table 4.3 Lattice Parameters of LT-Li_xCoO_2 and HT-Li_xCoO_2

SAMPLE	*a*(Å)	*c*(Å)	*c*/*a*
LT-$Li_{0.93}CoO_2$ (ex A)	2.8297(7)	13.870(4)	4.901(2)
LT-$Li_{0.71}CoO_2$ (ex B)	2.8304(4)	13.866(2)	4.899(1)
LT-$Li_{0.57}CoO_2$ (ex A)	2.8274(4)	13.852(2)	4.899(1)
LT-$Li_{0.40}CoO_2$ (ex B)	2.8273(2)	13.851(1)	4.899(1)
LT-$Li_{0.30}CoO_2$ (ex A)	2.8283(4)	13.857(3)	4.899(1)
LT-$Li_{0.5}CoO_2$ (elec)	2.8294(8)	13.861(4)	4.899(2)
HT-$Li_{0.93}CoO_2$	2.8159(3)	14.124(2)	5.016(1)
HT-$Li_{0.65}CoO_2$	2.818(7)	14.26(5)	5.06(2)
HT-$Li_{0.5}CoO_2$ (elec)	2.801(4)	14.25(3)	5.09(5)

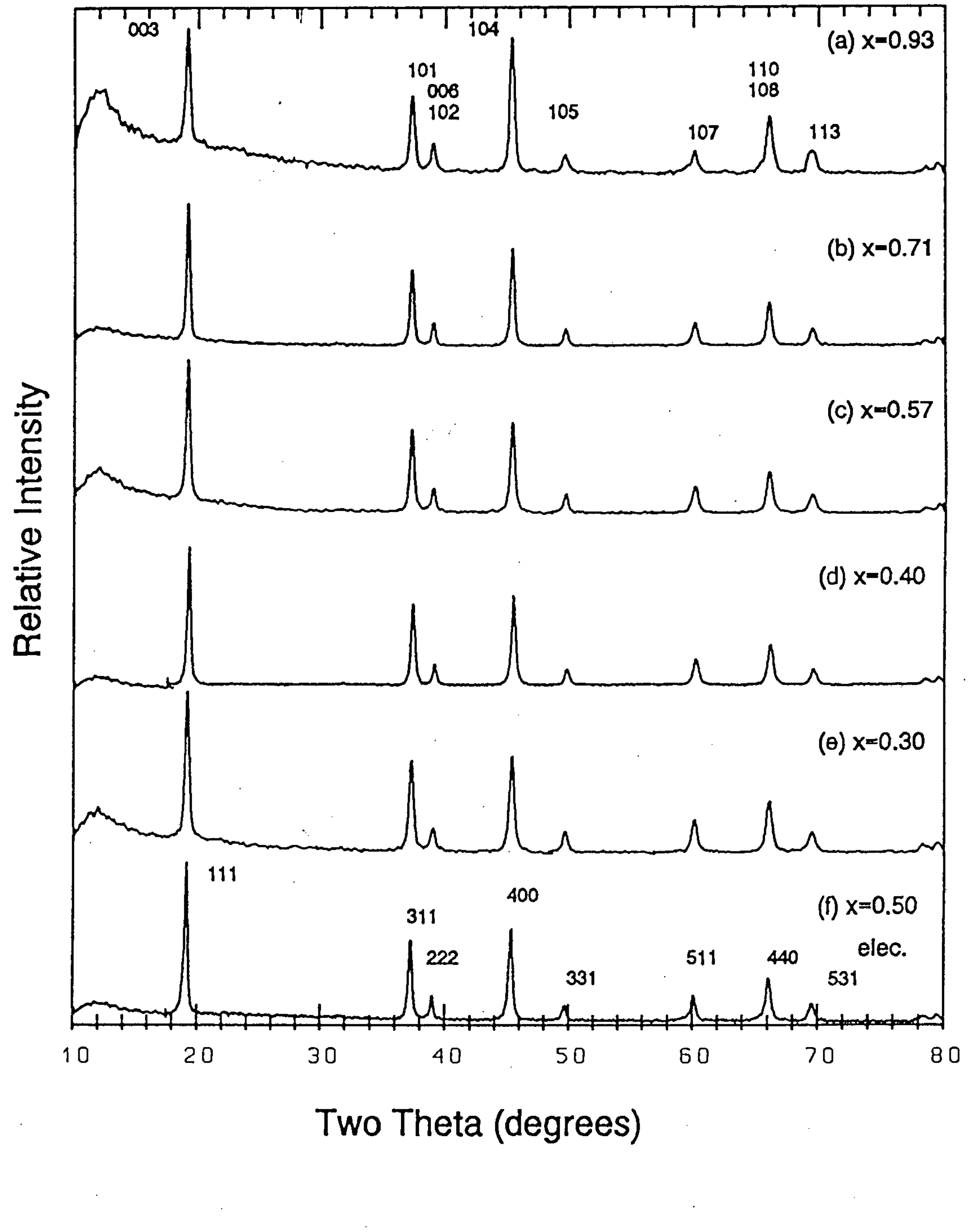

Figure 4.3 : Powder X-ray diffraction patterns of delithiated LT-$LiCoO_2$ samples. (a) indexed to a trigonal unit cell and (f) indexed to a fcc unit cell.

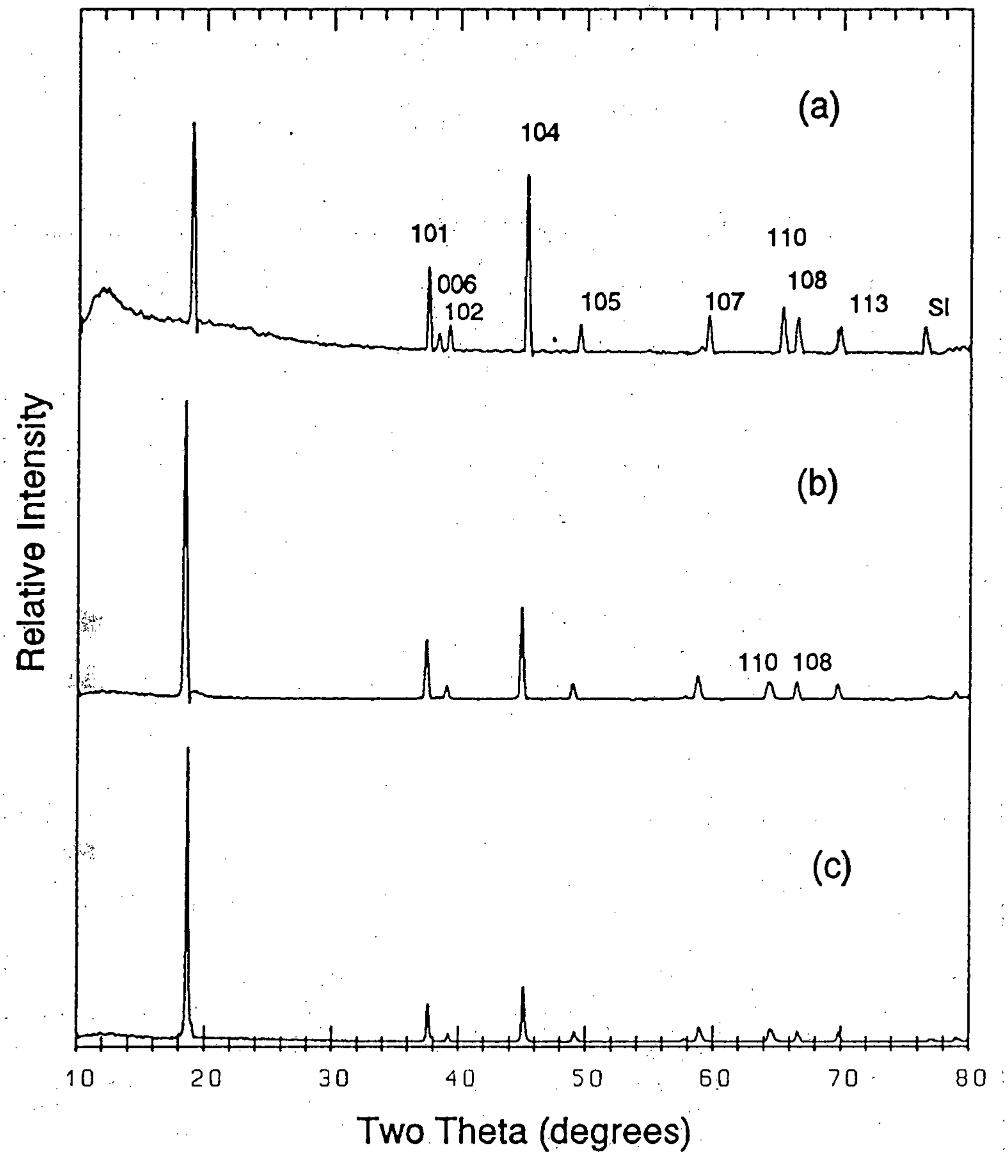

Figure 4.4 : X-ray diffraction patterns of delithiated HT-Li_xCoO_2 samples: a) x=0.93, b) x=0.65 and c) x=0.50 (electrochemically delithiated)

The X-ray diffraction profiles of LT-Li_xCoO_2 samples bear a close resemblance to those of LiM_2O_4 spinels where M=Ti[110], Mn[111] or V[50] and can again alternatively be indexed to a face-centred cubic unit cell (Fd3m symmetry). This is illustrated in Fig 4.3(f).

4.4 STRUCTURE DETERMINATION WITH X-RAY AND NEUTRON DIFFRACTION DATA

As discussed above, the near-cubic symmetry of LT-$LiCoO_2$ and delithiated products means that their diffraction patterns may be indexed either to a trigonal unit cell, by analogy with the high temperature material or to a face-centred cubic unit cell, by analogy with $Li[M_2]O_4$ spinel structures. As was noted earlier, the large intensity variations observed between HT-$LiCoO_2$ and LT-$LiCoO_2$ suggest a rearrangement of the cobalt cations in the crystal lattice of LT-$LiCoO_2$. The diffraction data of LT-$LiCoO_2$ (Sample A) and a chemically delithiated sample obtained by acid-leaching of sample B to a chemically determined composition $Li_{0.4}CoO_2$, obtained by both powder X-ray and neutron diffraction were refined in both the trigonal $R\bar{3}m$, and the prototypic spinel space group Fd3m.

Lithium is a light scatterer of X-rays due to its low atomic number and it is therefore difficult to refine lithium-ion positions from X-ray diffraction data. In the X-ray diffraction refinements of LT-$LiCoO_2$ the site occupancies of lithium and cobalt in crystallographically-equivalent octahedral sites were therefore allowed to vary simultaneously, while their sum was constrained to unity. The isotropic temperature factors obtained from the neutron diffraction refinements were used for the X-ray refinements; they were held constant in the refinement of the X-ray diffraction data. The positional parameter of the oxygen anions was also refined.

The neutron-scattering amplitudes of lithium (-0.203Å) and cobalt (+0.253Å) have similar magnitudes but differ in sign making neutron diffraction equally sensitive to both lithium and cobalt. The total observed neutron scattering from a particular crystallographic site can therefore be attributed to either :-

i) the presence of only cobalt or only lithium ions depending on the sign of the scattering, or

ii) to the presence of both cobalt and lithium ions such that the total scattering from the site remains the same.

This implies that it is not possible to determine the absolute cationic distribution of lithium cobalt oxides from neutron diffraction data but a narrow range of possible distributions can be defined. A favoured distribution may be selected based on other information regarding the sample, for example, the chemically-determined stoichiometry.

For the initial neutron diffraction refinements in this work, the lattice parameters used were those obtained from X-ray diffraction data. The isotropic temperature factors of the cobalt and lithium ions were refined independently of the site occupancies. The temperature factors of the oxygen anions were allowed to vary anisotropically. The positional parameter of the oxygen anions, z, was also refined.

Due to the greater sensitivity of neutron diffraction to the presence of lithium ions and the higher overall quality of the neutron diffraction data, the results of the neutron diffraction refinements are, in this study, regarded as being more reliable than those of the X-ray diffraction experiments.

4.4.1 Structure Determination of LT-$LiCoO_2$

The neutron-diffraction profiles of LT-$LiCoO_2$ refined in both the layered $R\bar{3}m$ and spinel Fd3m space groups are shown in Fig 4.5 (a and b) respectively. The analogous data for the refinements from X-ray diffraction data are given in Fig 4.6 (a and b).

Refinement in the Trigonal $R\bar{3}m$ Space Group

In the neutron-diffraction refinement of LT-$LiCoO_2$ in the $R\bar{3}m$ space group, the cobalt cations were allowed to occupy the 3b octahedral sites of the cobalt layer at (0 0 0.5), the 3a octahedral sites of the lithium layer at (0 0 0) and the two sets of crystallographically independent of 6c tetrahedral sites at (0 0 0.125) and (0 0 0.375).

Neutron-diffraction refinement of the standard HT-$LiCoO_2$ synthesised at 900°C, in the

TABLE 4.4(a)
Crystallographic Parameters for the Refinement of LT-$LiCoO_2$ (Sample A) from Neutron Diffraction Data

a = 2.826(1)Å c = 13.890(1)Å Space Group: $R\bar{3}m$ c/a = 4.915(2)

ATOM	SITE	POSITION			OCCU-PANCY	B_{11}/B_{ISO}	B_{22}	B_{33}	B_{12}
		x	y	z					
Li(1)	3a	0	0	0	0.94 (1)	1.6(1)	-	-	-
Li(2)	3b	0	0	0.5	0.04 (2)	0.9(1)	-	-	-
Co(1)	3a	0	0	0	0.06 (1)	1.6(1)	-	-	-
Co(2)	3b	0	0	0.5	0.96 (2)	0.9(1)	-	-	-
Co(3)	6c	0	0	0.375	0.01 (1)	0.9(1)	-	-	-
Co(4)	6c	0	0	0.125	0.00 (1)	0.9(1)	-	-	-
O	6c	0	0	0.2402 (1)	1.00	1.10(3)	1.10 (3)	1.21 (5)	0.55 (1)

<u>R Factors</u> R_p = 4.92%, R_{wp} = 4.67%, R_{exp} = 1.61%.

χ^2 = 8.385 for 1559 observations and 25 basic variables.

TABLE 4.4(b)
Crystallographic Parameters for the Refinement of LT-$LiCoO_2$ (Sample A) from X-ray Diffraction Data

a = 2.824(1)Å c = 13.888(1)Å Space Group: $R\bar{3}m$ c/a=4.918(2)

ATOM	SITE	POSITION			OCCU-PANCY	B_{ISO}
		x	y	z		
Li(1)	3a	0	0	0	0.95 (1)	1.6
Li(2)	3b	0	0	0.5	0.05 (1)	0.9
Co(1)	3a	0	0	0	0.05 (1)	1.6
Co(2)	3b	0	0	0.5	0.95 (1)	0.9
O	6c	0	0	0.2459(1)	1.00	1.13

<u>R Factors</u> R_p = 13.60%, R_{wp} = 17.97%, R_{exp} = 18.03%, R_{Bragg} = 10.74%

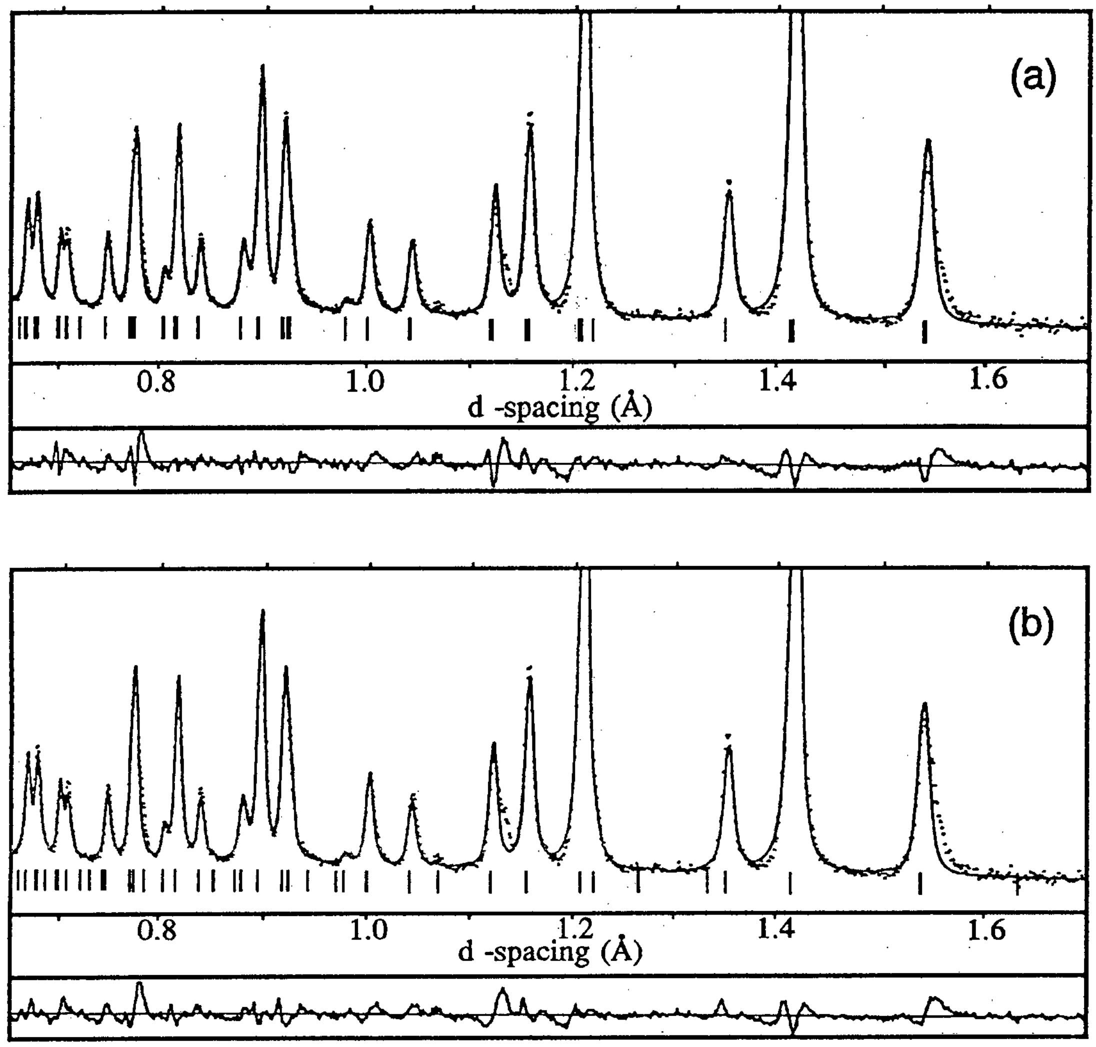

Figure 4.5 : The observed and calculated neutron diffraction profiles of LT-$LiCoO_2$ (Sample A) using a) the R$\bar{3}$m space group and b) the Fd3m space group.

$R\bar{3}m$ space group has shown that the 3a octahedral sites are occupied only by lithium cations and the 3b sites only by cobalt cations[60]. In contrast, neutron refinement of the LT-$LiCoO_2$ structure gave a favoured cation arrangement $(Li_{0.94}Co_{0.06})_{3a}[Co_{0.96}Li_{0.04}]_{3b}O_2$ with about 6% of the cobalt cations in the lithium-rich layers and approximately 4% of the lithium ions in the cobalt-rich layers. The occupancy of cobalt in the tetrahedral sites at (0 0 0.125) and (0 0 0.375) was found to be insignificant as expected for a rock salt structure. The overall composition refined to $Li_{0.98}Co_{1.02}O_2$ in excellent agreement with the expected stoichiometry (Table 4.4(a)).

The oxygen positional parameter z, refined to 0.2402(1) and not to 0.25 , the latter value corresponding to an ideally cubic close packed structure. This indicates a distortion of the anion lattice from cubic symmetry which results in a compression of the CoO_6 octahedra and an elongation of the LiO_6 octahedra. The c/a ratio also refined to 4.915(2) as opposed to the value of 4.899 which is expected for ideal cubic close packing, indicating that in LT-$LiCoO_2$ the oxygen array is not quite ideally cubic close packed.

The results of the Rietveld profile refinement of the X-ray diffraction data of LT-$LiCoO_2$ in the $R\bar{3}m$ space group are in excellent agreement with those of the neutron diffraction refinement, confirming the presence of a small amount of cobalt (5%) in the lithium-rich layer. The oxygen positional parameter refined to 0.2459(1) with c/a=4.918(2) again confirming the slight distortion of the lattice from ideal cubic symmetry (Table 4.4(b)). The c/a ratio is slightly larger than that found by least squares refinement of the X-ray peak positions (p66). The profile refinement data is considered to be the most accurate.

Refinement in the Spinel Space Group, Fd3m

For the refinement of the structure of LT-$LiCoO_2$ or LT-$Li_2Co_2O_4$ from neutron diffraction data in the Fd3m spinel space group both the lithium and cobalt cations were allowed to occupy both the 16c octahedral sites of the lattice at positions (0 0 0) and 16d octahedral sites at (0.5 0.5 0.5). A small amount of positive scattering from the tetrahedral 8a sites at (0.125 0.125 0.125) was observed. The oxygen positional parameter was also refined.

TABLE 4.5(a)

Crystallographic Parameters for the Refinement of LT-$LiCoO_2$ (Sample A) from Neutron Diffraction Data.
a = 8.002(1)Å Space Group: Fd3m

ATOM	SITE	POSITION x	y	z	OCCUPANCY	B_{11}/B_{iso}	B_{22}	B_{33}
Li(1)	16c	0	0	0	0.96(3)	1.7(1)	-	-
Li(2)	16d	0.5	0.5	0.5	0.01(2)	0.8(1)		
Co(1)	16d	0.5	0.5	0.5	0.99(2)	0.8(1)		
Co(2)	16c	0	0	0	0.02(3)	1.7(1)	-	-
Co(3)	8a	0.125	0.125	0.125	0.06(3)	1.7(1)		
O	32e	0.2588 (1)	0.2588 (1)	0.2588 (1)	1.00	1.15(1)	1.15(1)	1.15(1)

<u>R Factors</u> R_p = 5.44%, R_{wp} = 5.48%, R_{exp} = 1.62%.

χ^2 = 11.5 for 1559 observations and 19 basic variables.

TABLE 4.5(b)

Crystallographic Parameters for the Refinement of LT-$Li_2Co_2O_4$ (Sample A) from X-ray Diffraction Data
a = 7.994(1)Å Space Group: Fd3m

ATOM	SITE	POSITION x	y	z	OCCUPANCY	B_{ISO}
Li(1)	16d	0.5	0.5	0.5	0.06(1)	0.9
Li(2)	16c	0	0	0	0.95(1)	1.6
Co(1)	16d	0.5	0.5	0.5	0.94(1)	0.9
Co(2)	16c	0	0	0	0.05(1)	1.6
O	32e	0.2538 (3)	0.2538 (3)	0.2538 (3)	1.00	1.13

<u>R Factors</u> R_p = 15.29%, R_{wp} = 19.86%, R_{exp} = 18.76%, R_{Bragg} = 9.55%

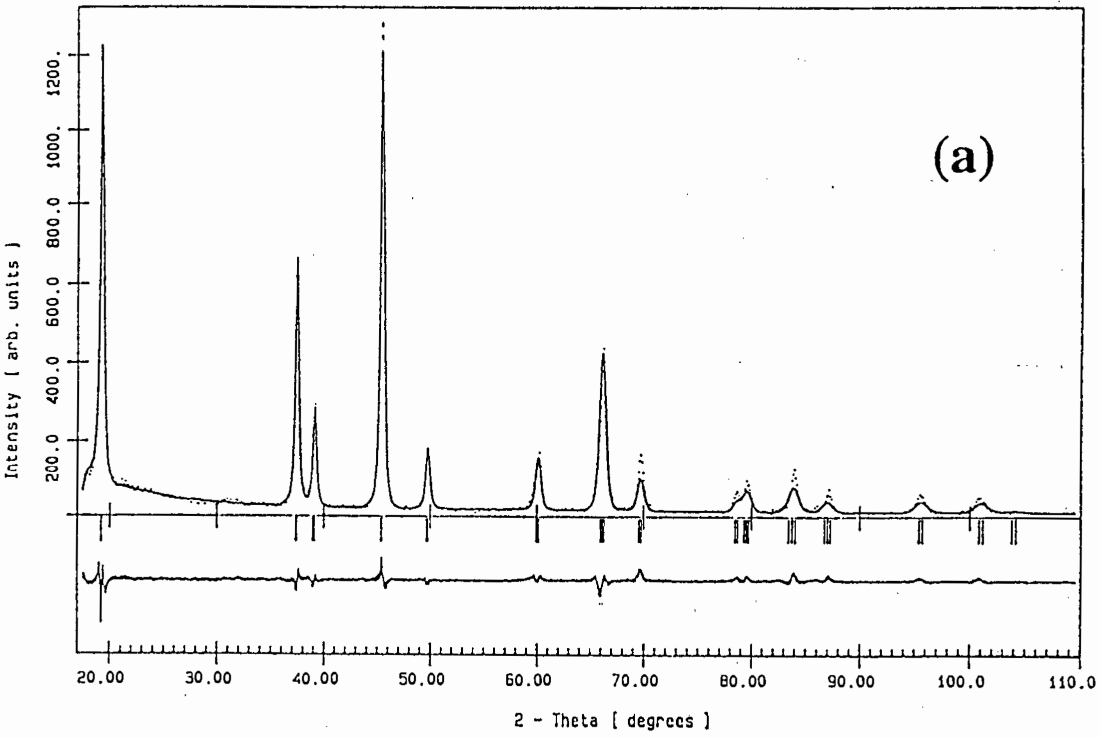

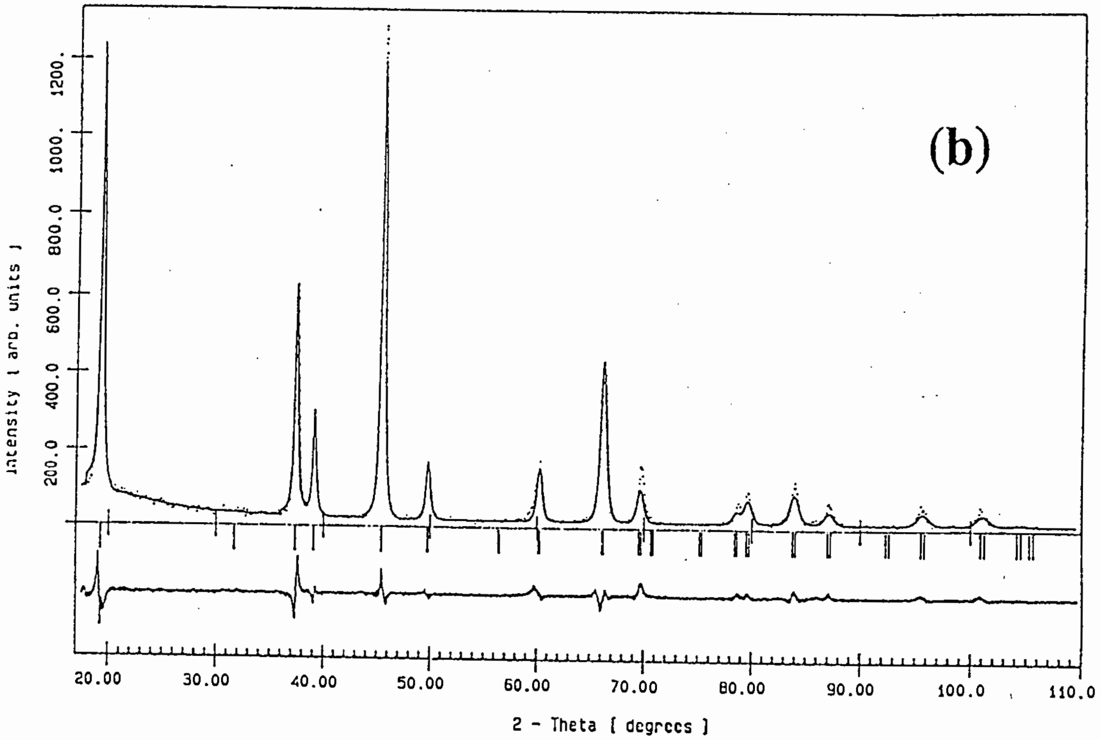

Figure 4.6 : The observed and calculated X-ray diffraction profile of LT-$LiCoO_2$ (Sample A) using a) the $R\bar{3}m$ space group and b) the Fd3m space group.

The refined cation distribution was $(Li_{1.96}Co_{0.04})_{16c}[Co_{1.98}Li_{0.02}]_{16d}O_4$ or $Li_{1.98}Co_{2.02}O_4$ which is very close to the ideal $A_2B_2O_4$ stoichiometry. The neutron diffraction refinement showed that there was a very small amount of cobalt in the tetrahedral sites (Table 4.5a). The occupation of tetrahedral sites by cobalt cations is unlikely as it would require cobalt ions to occupy face sharing 8a and 16c sites and would also result in a significant deviation from the chemically determined stoichiometry.

With Fd3m symmetry, the lattice constant refined to 8.002(1)Å and the oxygen positional parameter refined to 0.2588(1)Å. It should, however, be noted that strictly speaking the lattice constant of a cubic unit cell cannot be obtained ideally in this space group because of the slight deviation from ideal cubic close packing of the anion lattice; a c/a ratio of 4.915(2) was found by neutron refinement in the trigonal space group above.

The X-ray refinement of LT-$Li_2Co_2O_4$ with Fd3m symmetry with all cations occupying octahedral sites gives a cation distribution $(Li_{1.9}Co_{0.1})_{16c}[Li_{0.12}Co_{1.88}]_{16d}O_2$ or $Li_{2.02}Co_{1.98}O_4$ in reasonable agreement with the neutron diffraction data. The refined composition is, however, in excellent agreement with the expected chemical composition.

4.4.2 Discussion

Synthesis of $LiCoO_2$ at 400°C yields a compound (LT-$LiCoO_2$) with near-cubic symmetry which can be indexed to either a trigonal unit cell ($R\overline{3}m$ space group) or to a face-centred unit cell (Fd3m space group). The near-cubic symmetry ($c/a=4.90$) is maintained even after extensive delithiation. The rapid c-axis expansion with decreasing lithium content observed for perfectly layered HT-$LiCoO_2$ is not found for LT-$LiCoO_2$. In fact, the lattice parameters vary very little with lithium content.

The neutron-diffraction refinement of LT-$LiCoO_2$ with $R\overline{3}m$ symmetry shows that the lithium and cobalt cations are not perfectly ordered into alternate layers of octahedral sites in the distorted cubic-close-packed crystal lattice as is the case in $LiCoO_2$ synthesised at 900°C. In fact, in LT-$LiCoO_2$ about 6% of the cobalt cations are situated in the predominantly lithium layer of octahedral sites and vice versa. The cobalt cations in the predominantly lithium layer would provide an additional electrostatic binding energy between the layers and this could explain the reduction of the *c/a* ratio from 4.989(1) for HT-$LiCoO_2$ to 4.915(2) for LT-$LiCoO_2$ and the retention of the near-cubic symmetry (*c/a*=4.90) on delithiation.

$LiNiO_2$ also has $R\bar{3}m$ symmetry and has *c/a*=4.930(4)[55]. It has been reported that the $LiNiO_2$ material is difficult to synthesise with the ideal stoichiometry and compounds of the form $Li_{1-x}Ni_{1+x}O_2$ are commonly formed [58,59]. The additional Ni ions are of necessity situated in the lithium layer and the *c/a* ratio of these compounds approaches 4.90 as x increases. The neutron-diffraction refinement showed that the LT-$LiCoO_2$ material was slightly lithium deficient with a stoichiometry $Li_{0.98}Co_{1.02}O_2$ and the near-cubic symmetry of LT-$LiCoO_2$ is therefore consistent with $LiNiO_2$. However, despite the non-stoichiometry and imperfect layering, the c-axis of Li_xNiO_2 expands significantly on delithiation to give *c/a*=5.07(1) for x=0.5[51], in contrast to that of LT-Li_xCoO_2.

The X-ray and neutron diffraction data for LT-$LiCoO_2$ can be refined in both $R\bar{3}m$ and Fd3m space groups with similar R-factors. Figs 4.7 (a and c) show idealised diagrams of the layered and lithiated spinel structures; the two structures are significantly different. In the ideal layered structure the Li and Co cations are completely ordered into alternate close-packed layers perpendicular to only one of the 4 equivalent cubic {111} directions while in the spinel structure of $Li_2Co_2O_4$, there is a 3:1 ratio of Co cations in alternate layers of octahedral sites perpendicular to each of the 4 cubic {111} directions.

However, if the *c/a* ratio of the layered structure is chosen to be 4.90 and the oxygen *z* co-ordinate to be 0.25 (6c sites), then the oxygen framework is identical to that of the spinel structure with the oxygen anions at positions (0.25 0.25 0.25) i.e. u=0.25. The cation sites are also in the same positions in both structures. Under these conditions both the Fd3m and $R\bar{3}m$ space groups give identical powder diffraction patterns for X-rays and neutrons. This is illustrated in Table 4.6(a) which shows the observed and calculated X-ray diffraction intensities for the two space groups[91]; the crystallographic parameters used in the simulation are given in Table 4.6(b). This surprising result has been explained recently by Rossen el at[112].

In a powder diffraction experiment the scattered intensity obtained can be described as a sum of contributions of atom-pairs where the sum extends over all atoms in the structure. The summation can alternatively be expressed in terms of contributions from the nearest-neighbour shell, next-nearest-neighbour shell etc., where the separation between atom pairs is constant in a shell. Since the oxygen lattice is identical in both the layered and spinel structures (if $c/a=4.90$, $z=0.25$ and $u=0.25$), then the contribution to the scattered intensity from O-O, Li-O and Co-O pairs will be identical in both cases. Only the cation-cation pairs may be different. Rossen et al showed that the number and type of cation-cation contacts is the same in both structures out to the third shell and concluded that the cation-cation contacts are the same for all shells in the two structures. The scattered intensity of the two structures is therefore identical resulting in identical powder diffraction patterns for neutrons or X-rays.

In the case of ideal cubic close packing only a single crystal experiment would be able to distinguish between the two structures. For example, the peak at about 19° 2θ corresponds to the (111) spinel peak or the (003) layered peak. The (111) spinel peak consists of the sum of contributions of 8 reciprocal lattice points (±(111), ±(-111), ±(1-11), ±(11-1)), each with the same magnitude of the structure factor. The (003) layered peak is made up of the contributions of 2 reciprocal lattice points ±(003) each with a structure factor four times the magnitude of that of a single (111) reciprocal lattice point. A single crystal experiment would easily be able to show the existence of either 2 or 8 reciprocal lattice points.

It is therefore not possible to distinguish between the layered and spinel structures for LT-$LiCoO_2$ based only on powder diffraction data in the case of ideal cubic close packing of the anion lattice. However, the *c/a* ratio of LT-$LiCoO_2$ refined from X-ray and neutron diffraction data in the $R\bar{3}m$ space group is 4.91-4.92 which reflects a slight distortion from cubic symmetry. The R-factors for the refinement of the structure in the $R\bar{3}m$ space group (Neutrons : $R_p=4.92\%$, $R_{wp}=4.67\%$, X-rays : $R_p=13.60\%$, $R_{wp}=17.97\%$, $R_{Bragg}=10.74\%$) are also consistently lower than those for the Fd3m space group (Neutrons : $R_p=5.44\%$, $R_{wp}=5.48\%$, X-rays : $R_p=15.29\%$, $R_{wp}=19.86\%$, $R_{Bragg}=9.55\%$). It is therefore concluded that the layered $R\bar{3}m$ structure in which a small fraction (6%) of the cobalt ions resides in the lithium layer, is to be preferred to the lithiated spinel structure $Li_2[Co_2]O_4$.

Table 4.6(a): Observed intensities and intensities calculated with the Lazy-Pulverix program for $LiCoO_2$ in the $R\bar{3}m$ and Fd3m space groups.

Iobs	$R\bar{3}m$ h k l	$R\bar{3}m$ Icalc	Fd3m h k l	Fd3m Icalc
1000	0 0 3	1000	1 1 1	1000
0	-	0	2 2 0	0
579	1 0 1	549	3 1 1	549
224	0 1 2 0 0 6	202	2 2 2	202
1228	1 0 4	932	4 0 0	933
157	0 1 5	221	3 3 1	221
1			4 2 2	0
252	1 0 7 0 0 9	150	5 1 1 3 3 3	150
605	1 1 0 0 1 8	436	4 4 0	436
184	1 1 3 1 1 -3	130	5 3 1	130
0			6 2 0	0
187	0 2 1 1 1 6 1 1 -6 1 0 10 2 0 2	42 91	5 3 3 2 2 6	42 91
165	0 2 4 0 0 12	118	4 4 4	117
77	2 0 5 0 1 11	60	1 1 7 1 5 5	60
84	1 1 9 0 2 7	70	1 3 7 3 5 5	70
71	2 0 8	53	0 0 8	53
15	1 0 13	20	3 3 7	20

Table 4.6(b) Crystallographic Parameters for Lazy-Pulverix Simulation

Space Group : R$\bar{3}$m *a*=2.826Å, *c*=13.8474Å *c*/*a*=4.90

ATOM	SITE	POSITION x y z	B_{iso}	OCCUPANCY
Li	3a	0 0 0	1.0	1.0
Co	3b	0 0 0.5	1.0	1.0
O	6c	0 0 0.25	1.0	1.0

Space Group : Fd3m *a*=7.997Å

ATOM	SITE	POSITION x y z	B_{iso}	OCCUPANCY
Li	16c	0 0 0	1.0	1.0
Co	16d	0.5 0.5 0.5	1.0	1.0
O	32e	0.25 0.25 0.25	1.0	1.0

4.4.3 Structure Determination of LT-$Li_{0.4}CoO_2$

The neutron-diffraction profile of LT-$Li_{0.4}CoO_2$ refined in both the layered R$\bar{3}$m and spinel Fd3m space groups is shown in Fig 4.8(a and b) respectively. The analogous data for the refinements from X-ray diffraction data are given in Fig 4.9 (a and b).

Refinement in the Trigonal R$\bar{3}$m Space Group

For the refinement of the neutron powder diffraction pattern of $Li_{0.4}CoO_2$ with R$\bar{3}$m symmetry the cobalt cations were again allowed to occupy both the 3b octahedral sites

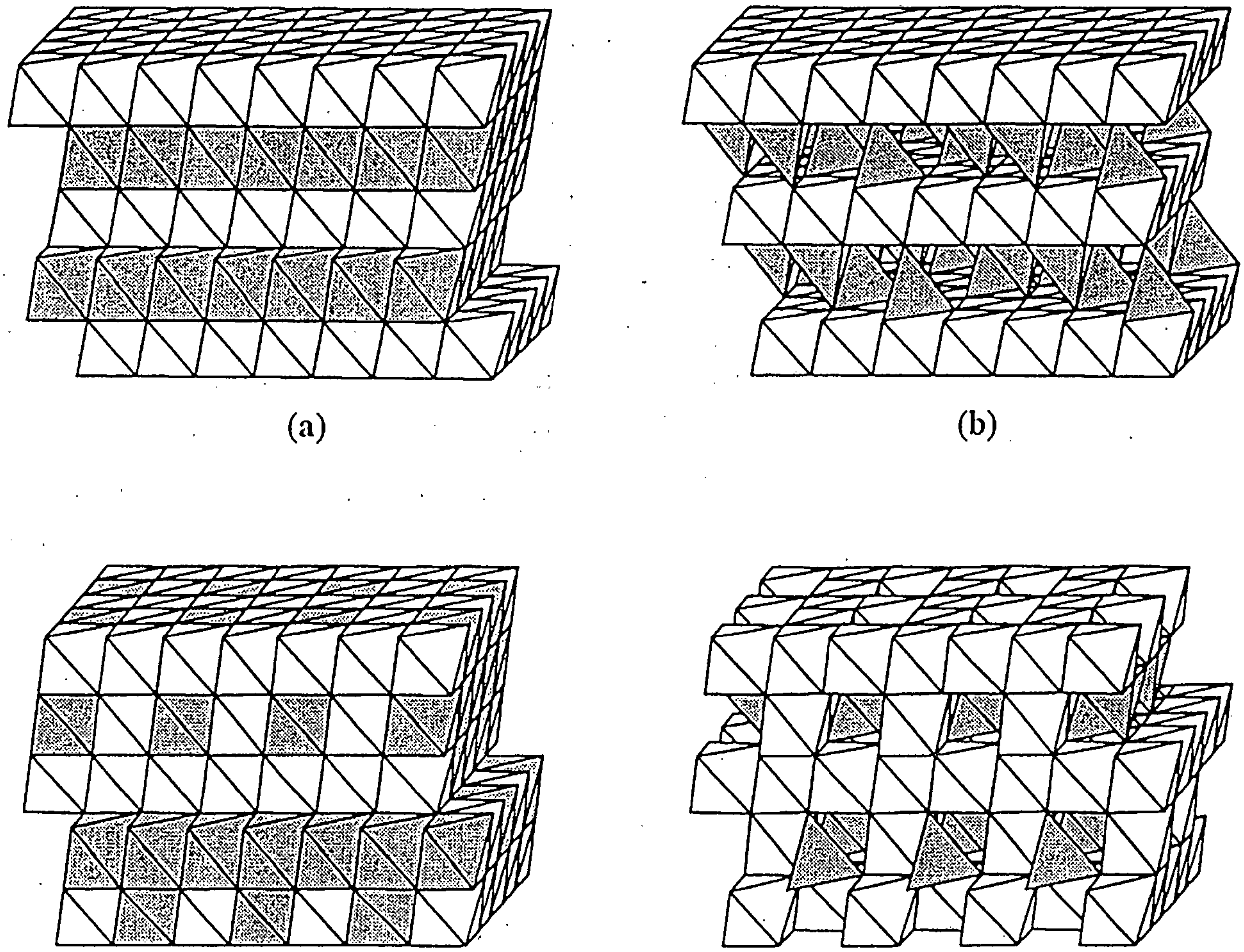
(a) (b) (c) (d)

Figure 4.7 : Idealised structures of a) $LiCoO_2$ layered, b) $Li_{0.5}CoO_2$ layered, c) $Li_2Co_2O_4$ spinel and d) $LiCo_2O_4$ spinel.

Shaded octahedra are cobalt occupied and clear octahedra are lithium occupied.

of the cobalt layer and the 3a octahedral sites of the lithium layer. The best fit to the experimental data was obtained when the cobalt cations were allowed to occupy the 3a and 3b octahedral sites and the lithium ions were allowed to occupy the 3a sites of the lithium layer and the 6c tetrahedral sites of the lithium layer at (0 0 0.375).

The favoured arrangement of the lithium and cobalt ions in the tetrahedral and octahedral sites of the structure is $(Li_{0.09}Co_{0.01})_{3a}\{Li_{0.40}\}_{6c}[Co_{0.99}]_{3b}O_2$ (Table 4.7(a)). This shows the somewhat surprising result that 80% of the remaining lithium cations are situated in the 6c tetrahedral sites of the original lithium layer with the other 20% in the 3a sites. The amount of cobalt in 3a sites is significantly less than that in the fully lithiated LT-$LiCoO_2$ material, 1% as opposed to 6%. The *c*/*a* ratio refines to 4.899(2) as expected for an ideally cubic close packed lattice but the oxygen positional parameter refines to 0.2377(1) significantly different from the ideal value of 0.25. The overall composition of the structure is $Li_{0.49}CoO_2$ which is in reasonable agreement with the chemically-determined composition.

For the X-ray diffraction refinement of LT-$Li_{0.4}CoO_2$ in the $R\bar{3}m$ space group the occupancies of the lithium ions in the layered structure were taken directly from the neutron diffraction refinement above. The results of the X-ray diffraction refinement confirm the presence of some scattering from the tetrahedral 6c sites of the lithium layer and the reduction of the amount of cobalt in the original lithium layer (Table 4.7(b)).

Refinement in the Spinel Space Group, Fd3m

In the neutron-diffraction refinement of the LT-$Li_{0.4}CoO_2$ data with Fd3m symmetry (Table 4.8(a)), the lithium cations were allowed to occupy both the 8a tetrahedral sites and the 16c and 16d octahedral sites. The cobalt cations were situated in the 16d octahedral sites at (0.5 0.5 0.5). The favoured cation distribution refined to $Li_{0.94}Co_{1.94}O_4$ or $\{Li_{0.83}\}_{8a}(Li_{0.06})_{16c}[Co_{1.94}Li_{0.06}]_{16d}O_4$ with lattice parameter a=7.991(1)Å. This represents a spinel structure with cobalt ions predominantly occupying the 16d sites and lithium ions mainly occupying 8a sites with a minor proportion in the 16c and 16d sites.

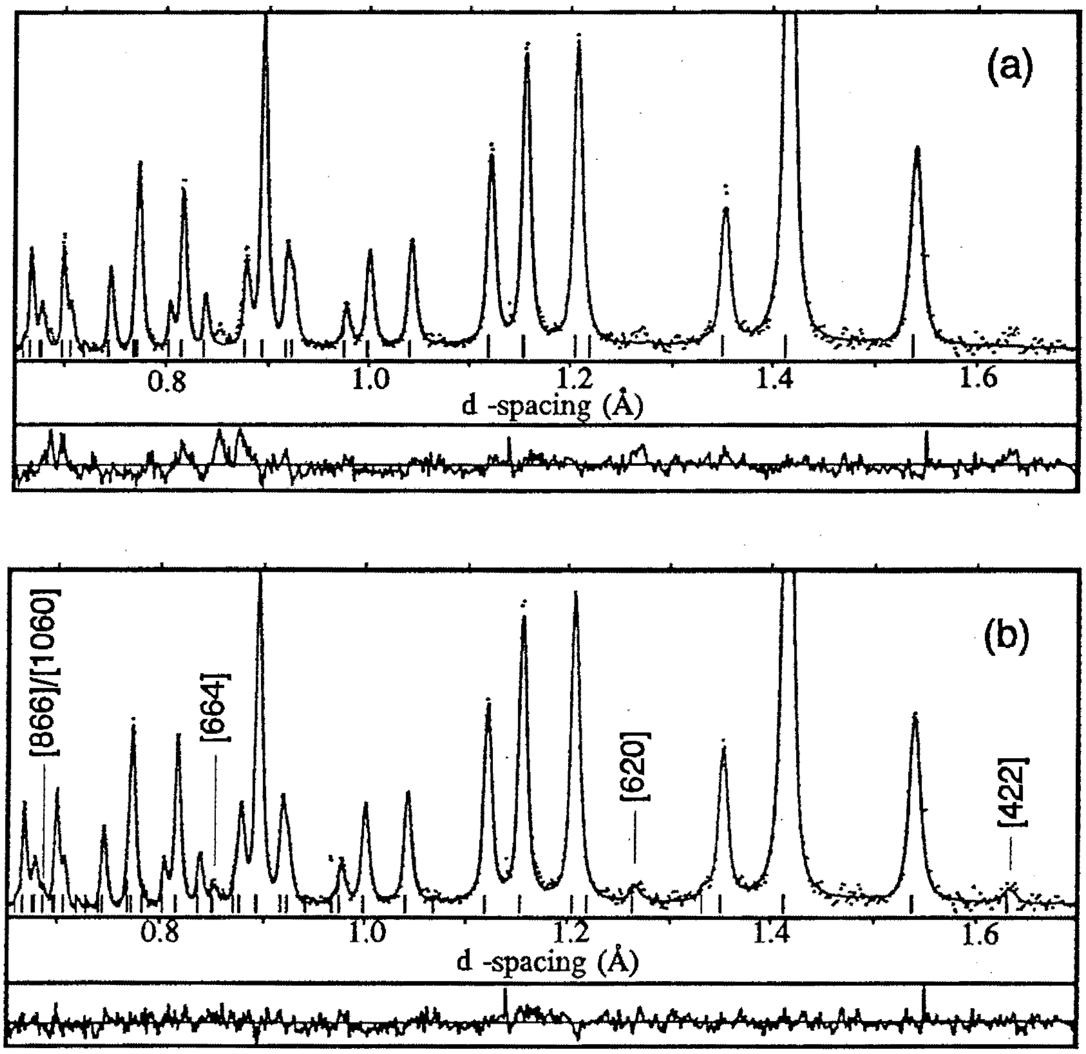

Figure 4.8 : Observed and calculated neutron diffraction profiles of LT-$Li_{0.4}CoO_2$ using a) the $R\bar{3}m$ and b) the Fd3m space groups.

TABLE 4.7(a)

Crystallographic Parameters for the Refinement of LT-$Li_{0.4}CoO_2$ from Neutron Diffraction Data

a = 2.825(1)Å c = 13.840(1)Å Space Group: R$\bar{3}$m c/a = 4.899(2)

ATOM	SITE	POSITION x y z	OCCU-PANCY	B_{11}/B_{iso}	B_{22}	B_{33}	B_{12}
Li(1)	3a	0 0 0	0.09(1)	0.96(5)	-	-	-
Li(2)	6c	0 0 0.375	0.20(1)	0.96(5)	-	-	-
Co(1)	3a	0 0 0	0.01(1)	0.96(5)	-	-	-
Co(2)	3b	0 0 0.500	0.99(1)	0.96(5)	-	-	-
O	6c	0 0 0.2377(1)	1.00	1.96(4)	1.96(4)	0.96(3)	0.98(2)

R Factors R_p = 3.49% $R_{wp}{}^2$ = 3.21% R_E = 1.65%

χ^2 = 3.78 for 1559 observations and 22 basic variables.

TABLE 4.7(b)

Crystallographic Parameters for the Refinement of LT-$Li_{0.4}CoO_2$ from X-ray Diffraction Data

a = 2.825(1)Å c = 13.846(1)Å Space Group: R$\bar{3}$m c/a = 4.901(2)

ATOM	SITE	POSITION x y z	OCCUPANCY	B_{iso}
Li(1)	3a	0 0 0	0.09	0.96
Li(2)	6c	0 0 0.375	0.20	0.96
Co(1)	3a	0 0 0	0.02(1)	0.96
Co(2)	3b	0 0 0.5	0.99(1)	0.96
O	6c	0 0 0.2437(3)	1.00	1.63

R Factors R_p = 12.40% R_{wp} = 15.88% R_E = 16.98% R_{Bragg}=10.82%

TABLE 4.8(a)
Crystallographic Parameters for the Refinement of LT-$Li_{0.4}CoO_2$ from Neutron Diffraction Data

a = 7.991(1)Å Space Group: Fd3m

ATOM	SITE	POSITION			OCCU-PANCY	B_{11}/B_{iso}	B_{22}	B_{33}
		x	y	z				
Li(1)	8a	0.125	0.125	0.125	0.83(3)	1.7(1)	-	-
Li(2)	16c	0	0	0	0.03(1)	1.7(1)	-	-
Li(3)	16d	0.5	0.5	0.5	0.03(1)	0.9(1)	-	-
Co	16d	0.5	0.5	0.5	0.97(1)	0.9(1)	-	-
O	32e	0.2629 (1)	0.2629 (1)	0.2629 (1)	1.00	1.35(2)	1.35 (2)	1.35 (2)

<u>R Factors</u> R_p = 3.49% $R_{wp}{}^2$ = 3.21% R_E = 1.65%

χ^2 = 3.78 for 1559 observations and 22 basic variables.

TABLE 4.8(b)
Crystallographic Parameters for the Refinement of LT-$Li_{0.4}CoO_2$ from X-ray Diffraction Data

a = 7.992(1)Å Space Group: Fd3m

ATOM	SITE	POSITION			OCCUPANCY	B_{iso}
		x	y	z		
Li(1)	8a	0.125	0.125	0.125	0.8	0.96
Co(1)	16d	0.5	0.5	0.5	0.99(1)	0.96
Co(2)	16c	0	0	0	0.03(1)	0.96
O	32e	0.2566 (3)	0.2566 (3)	0.2566 (3)	1.00	1.63

<u>R Factors</u> R_p = 11.74% R_{wp} = 15.53% R_E = 17.71% R_{Bragg}=8.35%

For the refinement of the X-ray diffraction data of LT-$Li_{0.4}CoO_2$ in the Fd3m space group the lithium ions were assumed to occupy only the 8a tetrahedral sites and the cobalt cations were refined on both the 16c and 16d octahedral sites of the structure. The cationic distribution refined to $\{Li_{0.8}\}_{8a}(Co_{0.06})_{16c}[Co_{1.98}]_{16d}O_4$ or $Li_{0.8}Co_{2.04}O_4$. (Table 4.8(b)).

4.4.4. Discussion

The equivalence of the powder diffraction data of Li_xCoO_2 compounds with Fd3m and $R\bar{3}m$ symmetry is destroyed by the presence of lithium in the tetrahedral sites of the structure. The neutron diffraction refinement of LT-$Li_{0.49}CoO_2$ in the $R\bar{3}m$ space group showed that 80% of the remaining lithium ions were in the 6c tetrahedral sites of the lithium layer at (0 0 0.375); the remaining 20% were in the octahedral sites of the original lithium layer at (0 0 0.125). This result is surprising because of the short intersite distance (1.73 Å) between the lithium in 6c tetrahedra and the cobalt in face-sharing 3b octahedra.

In the spinel Fd3m space group the 8a tetrahedra share faces with two empty 16c octahedra. The separation between the 8a tetrahedral sites and occupied 16d octahedral sites is 3.20Å while between the 16d and 16c octahedral sites it is 2.79Å making the 8a tetrahedral sites energetically favourable in an AB_2X_4 spinel.

Comparison of the refinement results for LT-$Li_{0.4}CoO_2$ in the two space groups for both X-rays and neutrons shows slightly lower R-factors for the refinement with the Fd3m space group. In particular, the value of χ^2 is 2.21 for Fd3m compared to 3.78 for $R\bar{3}m$ for the neutron diffraction refinements. Examination of the neutron diffraction profile (Fig 4.8) shows several minor peaks which correspond to characteristic spinel reflections which are absent in the $R\bar{3}m$ space group e.g (6 6 4), (6 2 0) and (4 2 2). This clearly indicates that the spinel model of the LT-$Li_{0.4}CoO_2$ sample is favoured over the layered model.

It is therefore concluded that the layered $R\bar{3}m$ structure with some lithium in the cobalt-

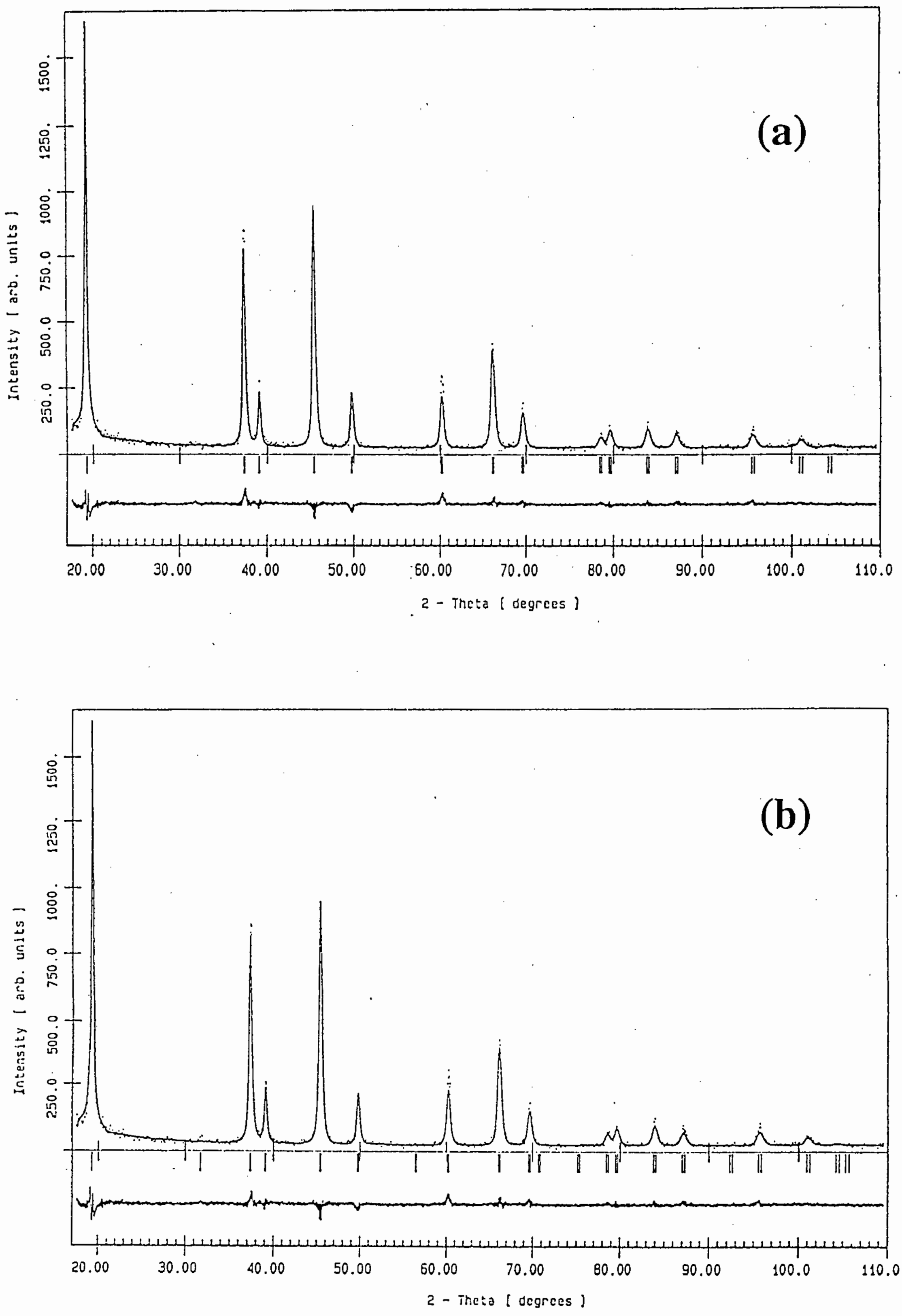

Figure 4.9 : Observed and calculated X-ray diffraction profiles of LT-$Li_{0.4}CoO_2$ using a) the $R\bar{3}m$ and b) the Fd3m space groups .

rich layers and some cobalt in the lithium-rich layers is preferred for the sample of LT-$LiCoO_2$ studied, while the chemically delithiated product LT-$Li_{0.4}CoO_2$ has a spinel Fd3m structure. This implies that a structural transformation occurs when the sample is chemically delithiated.

Transformation from a layered to a spinel structure involves the migration of a quarter of the cobalt cations from the 3b octahedra of the cobalt-rich layer via the face-sharing tetrahedra to the 3a octahedra of the lithium-rich layer and a rearrangement of the lithium ions. This transformation has been demonstrated with the isostructural layered $LiMO_2$ compounds (M=V or Ni), where moderate heating (200-400°C) of delithiated $Li_{0.5}MO_2$ compounds results in the formation of the spinels LiV_2O_4[50] and $LiNi_2O_4$ [51,52].

The structure of an electrochemically delithiated product has not been determined due to the difficulty in obtaining sufficiently large samples for neutron diffraction analysis. Although the X-ray diffraction profiles of chemically and electrochemically delithiated products are very similar in terms of both peak position and intensity (Figs 4.3(d) and (f)), the above structure determinations demonstrate that an unequivocal identification of the spinel structure is only possible from neutron diffraction data.

The chemical delithiation process takes place according to the reaction :-

$$3\ LiCoO_2 \rightarrow Li[Co_2]O_4 + CoO + Li_2O \quad (20-30°C)$$

in which both CoO and Li_2O dissolve in the acidic environment. The reaction mechanism is expected to be similar to that which occurs in the formation of λ-MnO_2 from $LiMn_2O_4$ in an acid environment[47]. It seems likely that the chemical delithiation mechanism facilitates the transformation of the structure to spinel in the case of LT-Li_xCoO_2.

$LiVO_2$ has the $R\bar{3}m$ structure and is isostructural with HT-$LiCoO_2$. It has been found however that on delithiation the layered structure of $LiVO_2$ is not maintained[57]. Approximately a third of the vanadium cations appear to migrate from the 3b sites of the original vanadium layer, via the tetrahedral sites, to the 3a sites of the predominantly lithium layer and thus stabilise the structure. The migration of the vanadium cations from 3b to 3a octahedral sites is clearly evident from the marked decrease in the intensity of the (003) peak as the lithium content decreases. In the case of vanadium it has been proposed that the disproportionation of V^{4+} to V^{3+} and V^{5+} could explain the mobility of vanadium in the structure; the V^{5+} (d^0) cation has no octahedral or tetrahedral CFSE making it equally stable in tetrahedral and octahedral sites.

In Li_xNiO_2, no change in the (003) peak intensity has been found on delithiation which suggests that nickel ions are not displaced to the original lithium-rich layer at ambient temperature[52]. The Ni^{2+}, Ni^{3+} and Ni^{4+} ions all have a strong octahedral site preference. In this case the displacement only occurs at 250°C when spinel formation is reported to occur.

In LT-$LiCoO_2$ no dramatic change in the (003) peak intensity is observed as the lithium content decreases in either electrochemically or chemically delithiated samples. The transition from layered to spinel structures appears to occur rapidly in chemically delithiated samples without the intermediate phase of a disordered layered structure with a large number of cobalt atoms in the lithium-rich layer. This rapid transition is believed to be associated with a concomitant dissolution of Co^{2+} ions from the surface of the particles as LT-$LiCoO_2$ is delithiated. This demonstrates for the first time that the spinel $LiCo_2O_4$ is stable and can be prepared at low temperatures (20-30°C).

4.5 ELECTROCHEMICAL DATA

4.5.1 Electrochemical Curves

Fig. 4.10 shows the electrochemical curves for the initial lithium extraction\insertion in Li/LT-Li_xCoO_2 cells, as well as data for Li/HT-Li_xCoO_2 cells for comparison. Curve (a) shows data recorded allowing a 7 day equilibration time per data point and curve (b) shows data recorded with a 48 hour equilibration time. Curve (a) shows a rapid initial voltage increase followed by a voltage plateau at 3.61V between $x=0.2$ and $x=0.95$ in Li_xCoO_2. Curve (b) confirms the existence of the voltage plateau for $0.5<x<0.95$ but shows an increasing voltage with decreasing x in the range 0.2<x<0.5. Very large polarisation voltages were recorded in this range and the cell had not equilibrated after 48 hours. This indicates that the removal of lithium from the structure becomes increasingly difficult as x decreases.

The OCV data for Li/LT-$LiCoO_2$ cells contrast with those for Li/HT-$LiCoO_2$ cells. The data recorded for this work are only reported to x=0.4 (curve (d) in Fig 4.10); for x<0.4 polarisation voltages >4.5V were obtained resulting in degradation of the cell. The results obtained are in excellent agreement with the OCV curve reported by Mizushima et al[62] for a Li/HT-$LiCoO_2$ cell (Fig4.10(c)) and show an OCV which increases steadily as the lithium content decreases to reach 4.5V at x=0.2.

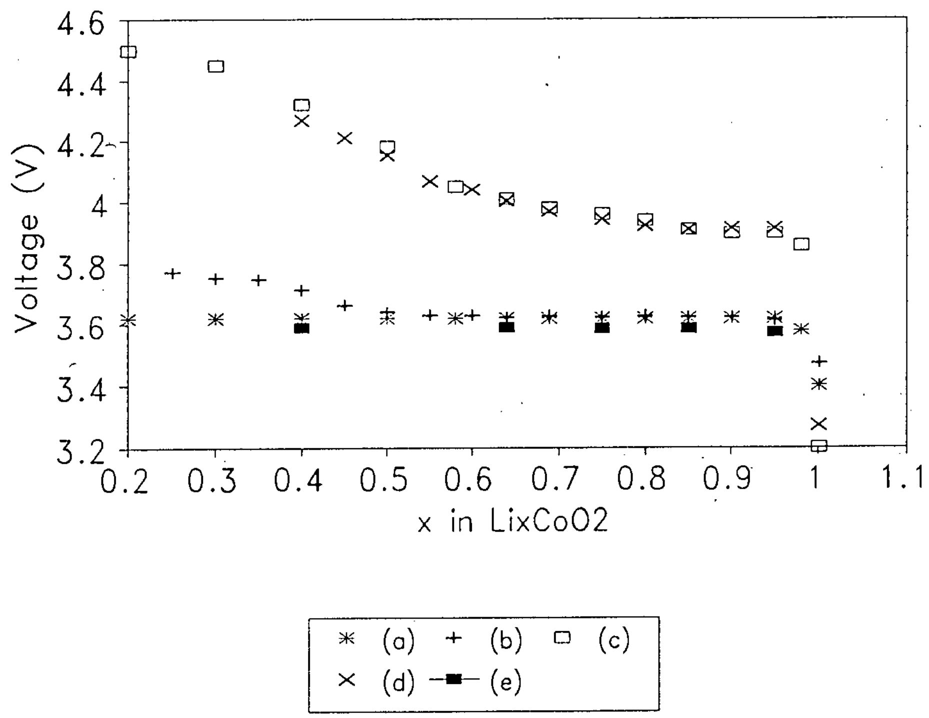

Figure 4.10 : OCV curves for a) LT-$LiCoO_2$ (7 day) b) LT-$LiCoO_2$ (2 day), c) HT-$LiCoO_2$[62], d) HT-$LiCoO_2$ (this work) and e) LT-$Li_{0.4}CoO_2$ (acid-leached).

In an independent study, OCV measurements of an Li/LT-Li_xCoO_2 cell, using chemically-prepared LT-$Li_{0.4}CoO_2$ as the initial cathode, showed a constant voltage plateau at 3.59V for $0.4 \leq x \leq 0.95$ on discharge (Fig 4.10(e)).

The plateau in the OCV curves of Li/LT-Li_xCoO_2 cells can be attributed to the co-existence of two phases in the cathode over the corresponding composition range. In the light of the structural study (Section 4.4), it seems most likely that the two phases are a layered LT-$LiCoO_2$ phase with some lithium in cobalt-rich layers and some cobalt in lithium-rich layers and a spinel-like $LiCo_2O_4$ phase. The spinel nature of an **electrochemically-delithiated** product has, however, yet to be confirmed.

The two-phase nature of LT-Li_xCoO_2 cathodes results in a significantly lower voltage over the entire composition range compared to the high temperature analogue. One of the major limitations in the application of HT-$LiCoO_2$ cathodes in lithium cells is the high voltages reached on charge which are outside the electrochemical stability window of most commonly used electrolytes. LT-Li_xCoO_2 cathodes are therefore of significant interest as possible alternatives to HT-$LiCoO_2$ electrodes.

4.5.2 Cyclic Voltammetry

The structural refinement of LT-Li_xCoO_2 suggested that, when delithiated chemically, the structure transforms from a layered structure to a spinel-type structure. It is therefore of interest to compare the cyclic voltammogram of LT-Li_xCoO_2 with the cyclic voltammogram of a Li/$Li_xMn_2O_4$ cell which has been characterised in detail[72,113-114] (Fig.4.11) and which is typical of the behaviour of stoichiometric spinel cathodes. Peak 1 corresponds to the removal of lithium from the octahedral sites and peaks 2 and 3 correspond to the removal of lithium from tetrahedral sites. The peaks corresponding to removal of lithium from tetrahedral and octahedral sites are separated by ~1V. This is also the case for LiV_2O_4 spinels[115]. The small peak at 3.8V on the anodic scan (peak 4) has been attributed to the removal of lithium from the octahedral 16d sites of the spinel structure. In the case of $LiMn_2O_4$ the insertion and removal of lithium from tetrahedral and octahedral sites is reversible.

The cyclic voltammogram of LT-Li_xCoO_2 recorded against a pure lithium anode at 0.5mV/s and charged to an upper voltage limit of 4.6V is shown in Fig 4.12. No peaks were found on an initial cathodic scan. On the initial anodic scan a large peak was

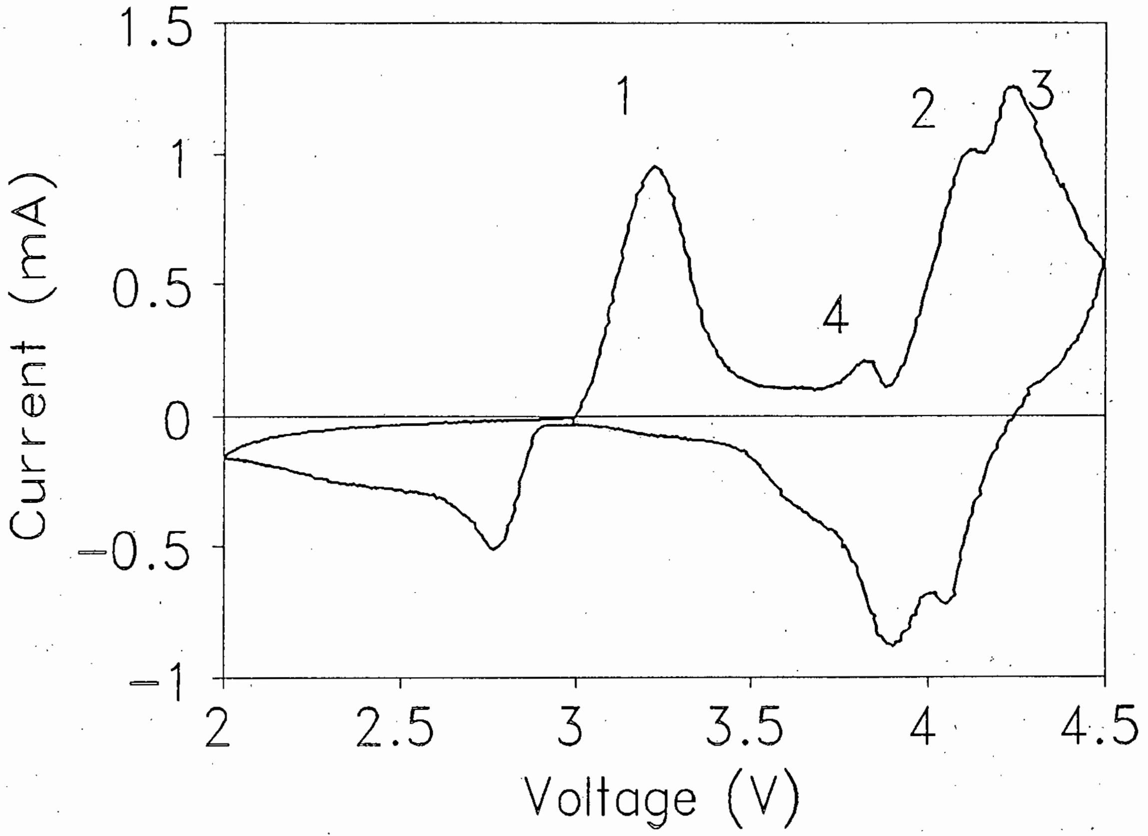

Figure 4.11 : Cyclic voltammogram of a Li/$LiMn_2O_4$ cell (0.1 mV/s).

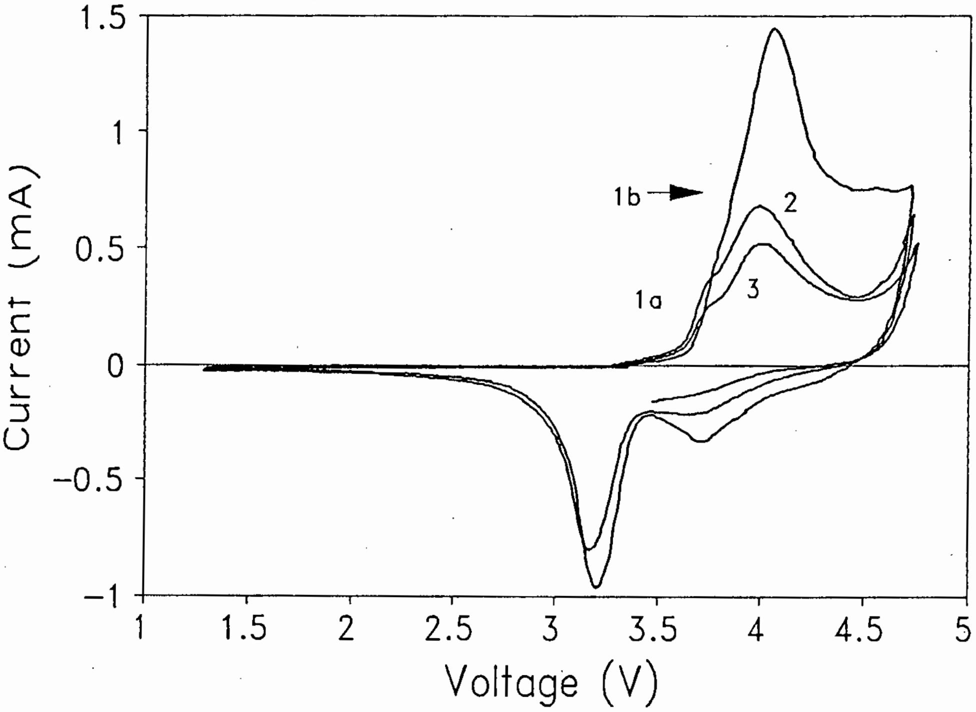

Figure 4.12 : Cyclic voltammogram of a Li/LT-$LiCoO_2$ cell (0.5 mV/s).

observed at ~4.0V (peak 1 in fig 4.12) and was attributed to a) the removal of lithium from the octahedral sites of the structure and b) the removal of further lithium from the octahedral sites and the generation of a "quasi-spinel" phase in which lithium ions are located mainly in the tetrahedral sites of the structure. On subsequent anodic scans two anodic peaks are clearly resolved. The peak at 3.7V on the cathodic scan is attributed to lithium insertion into the tetrahedral sites of the structure, while the peak at 3.2V is attributed to re-insertion of lithium into the octahedral sites. In the case of LT-$LiCoO_2$ the peaks associated with lithium insertion into the tetrahedral and octahedral sites of the structure are separated by only 0.5V. This suggests that electrochemical delithiation of LT-Li_xCoO_2 results in a "quasi-spinel" structure in which the distribution of cobalt and lithium cations in the structure is intermediate between that of the $R\bar{3}m$ structure and that of the Fd3m spinel structure. The rapid drop in the CV peak intensities on cycling indicate that the spinel-like structure is unstable on cycling. This result is consistent with data obtained from the investigations of the rechargeability of Li/LT-Li_xCoO_2 cells which will be reported in the following section.

The structural transformation of LT-Li_xCoO_2 to the "quasi-spinel" structure should be evident from the cyclic voltammograms of Li/LT-Li_xCoO_2 cells. Fig 4.13(a) shows the first two cycles of a Li/LT-Li_xCoO_2 cell cycled to an upper voltage limit of 3.7V. The cathodic peak at ~3.45V corresponds to re-insertion of lithium into the octahedral sites of the structure. The insertion and removal of lithium appears to be reversible in this voltage range. On raising the upper voltage limit to 3.75V and 3.8V on cycles 3 and 4-5 respectively, the cathodic peak shifts to lower voltage and a second anodic peak appears at ~3.7V (Fig 4.13(b)). This effect becomes more pronounced when the upper voltage limit is raised to 4.0V on cycles 6-8 (fig.4.13(c)). This suggests that on charging to voltages >3.7V a change in the lattice occurs which changes the energies of the lithium sites.

The cyclic voltammogram of the chemically-prepared LT-$Li_{0.40}CoO_2$,(which has been shown by neutron diffraction refinement to have a spinel structure $Li_{0.94}Co_{1.94}O_4$), recorded versus a lithium anode (Fig. 4.14) shows that no lithium is extracted from the tetrahedral sites of the structure on the initial anodic scan below 4.6V. The cyclic

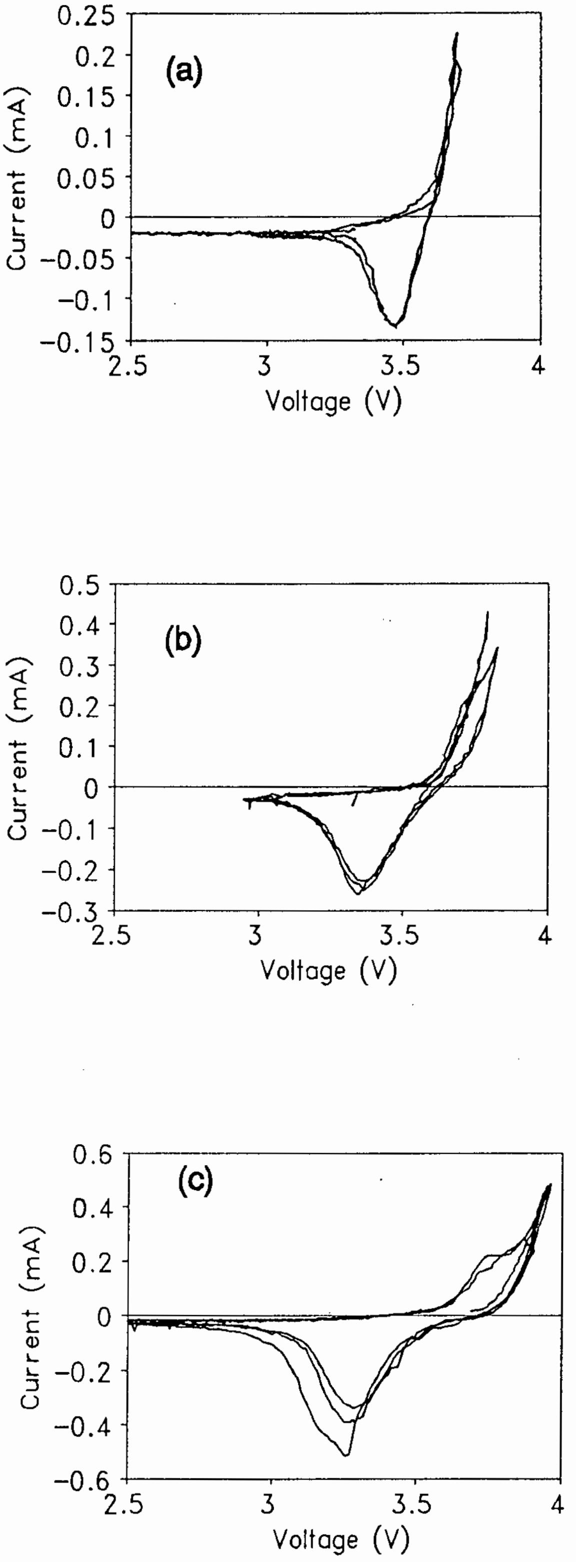

Figure 4.13 : Cyclic voltammograms of a Li/LT-$LiCoO_2$ cell cycled a) cycles 1 and 2 to 3.7V, b) cycle 3 to 3.75V, cycles 4 and 5 to 3.8V and c) cycles 6,7 and 8 to 4.0V. (0.5mV/s)

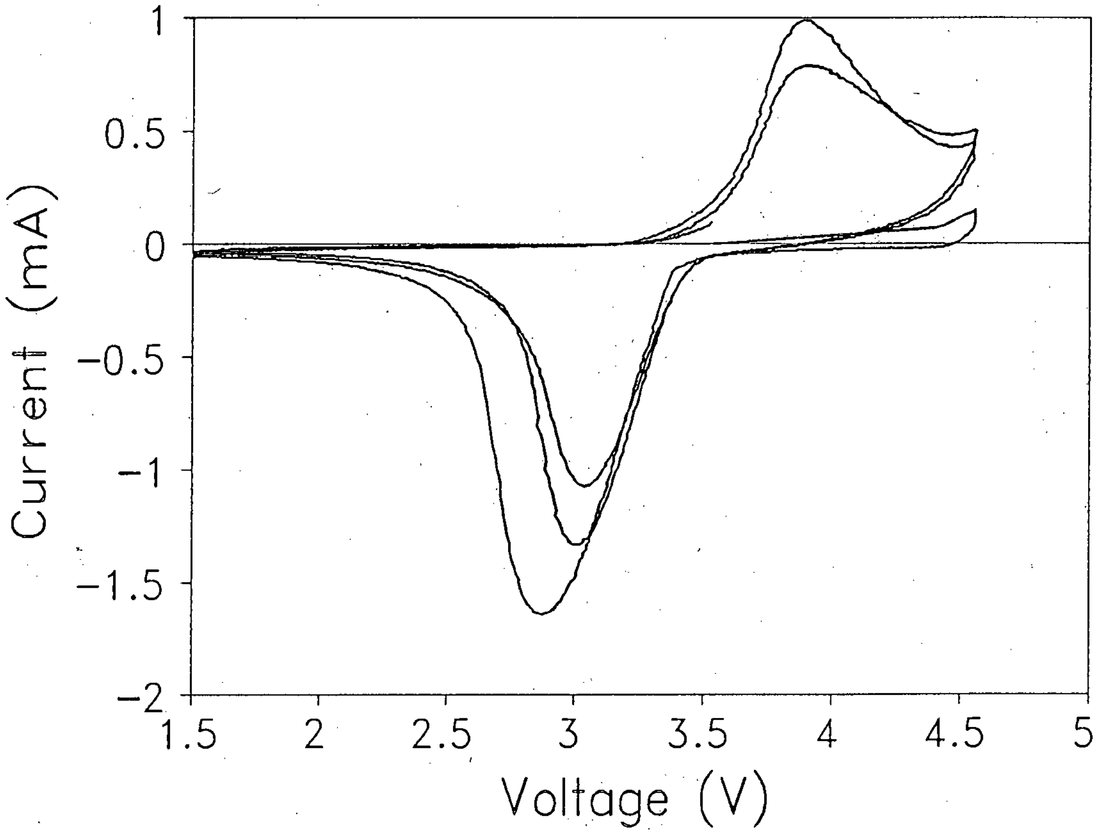

Figure 4.14 : Cyclic voltammogram of a Li/LT-$Li_{0.4}CoO_2$ cell (chemically delithiated) (0.5mV/s)

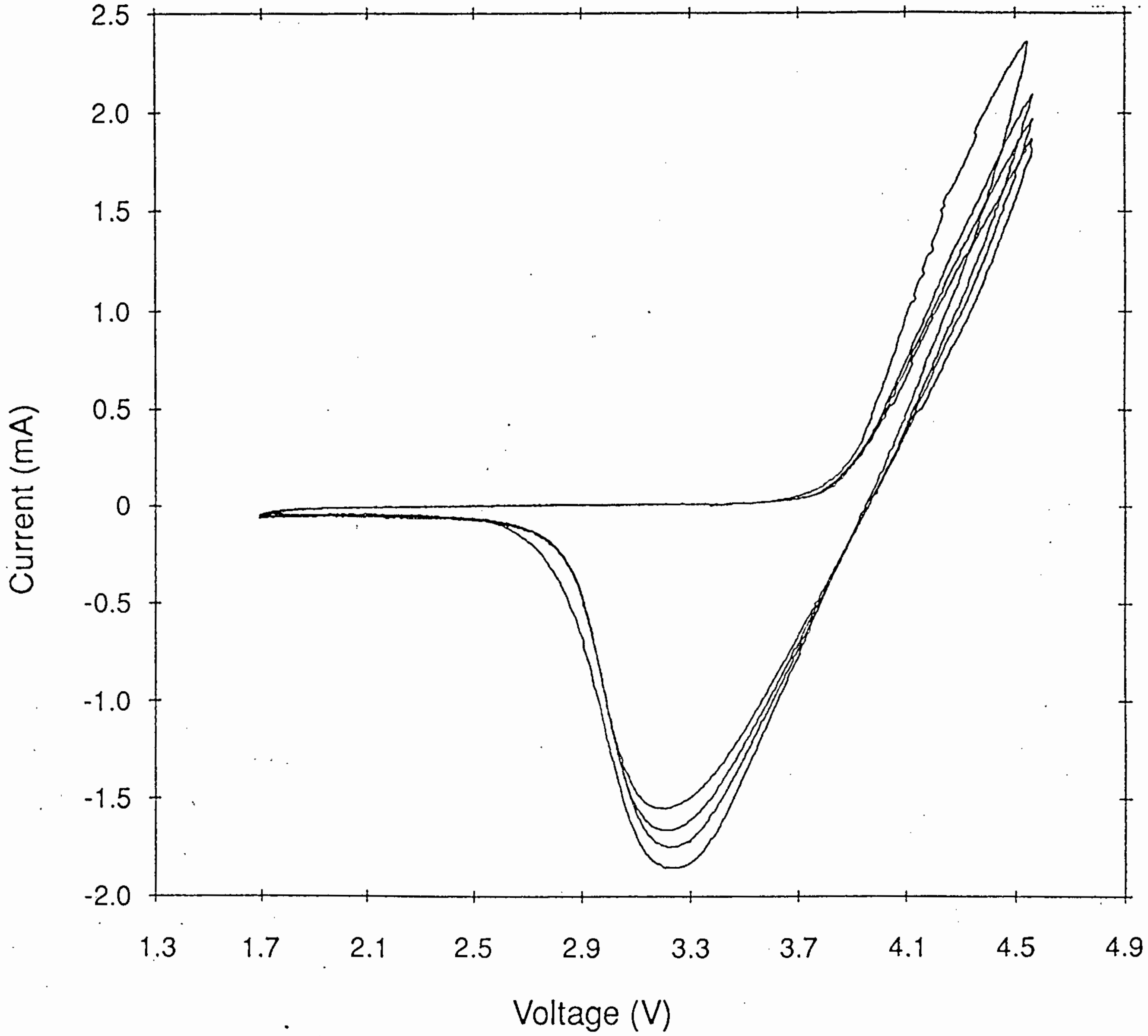

Figure 4.15 : Cyclic voltammogram of a Li/HT-Li_xCoO_2 cell (0.5mV/s)

voltammogram shows a single step insertion and removal of lithium which corresponds to insertion and removal of cations from the octahedral 16c sites of the lattice. In $LiMn_2O_4$ and LiV_2O_4 spinels, extraction of lithium from the tetrahedral sites of the lattice occurs at a voltage approximately 1V higher than extraction of lithium from the octahedral sites. By analogy, lithium extraction from the tetrahedral sites of a $LiCo_2O_4$ spinel would only be expected to occur at ~4.6V. This very high voltage is outside the electrochemical stability window of the electrolytes used.

The cyclic voltammogram of a Li/HT-Li_xCoO_2 cell recorded at 0.5 mV/s is shown in Fig 4.15 for comparison. It shows one-step processes for lithium insertion and extraction. The subtle structural changes that occur on delithiation of HT-$LiCoO_2$ are only visible in cyclic voltammograms recorded at very low rates. The voltages of the anodic and cathodic peaks are significantly higher than those of LT-Li_xCoO_2 in agreement with the OCV data obtained from electrochemical cells (Fig. 4.10).

4.5.3 Galvanostatic Cycling

The first charge and discharge curves of a Li/LT-$LiCoO_2$ cell recorded between 3.2 and 3.9V versus lithium (current densities : 0.1 mA/cm^2 on charge and 0.2 mA/cm^2 on discharge and electrolyte : 1M $LiClO_4$ in 1:1 PC/DME) are shown in Fig 4.16. The results indicate that ~0.46 lithium ions can be removed from the LT-$LiCoO_2$ structure below 3.90V corresponding to a final composition of $Li_{0.54}CoO_2$ or $Li_{1.08}Co_2O_4$ which is close to the stoichiometric spinel composition. However only about 0.24 lithium ions can be re-inserted on discharge to 3.2V. Subsequent cycles showed a very low capacity of approximately 20mAhr/g corresponding to $\Delta x \approx 0.1$ in Li_xCoO_2. Raising the upper voltage limit to 4.2V (Fig 4.17) failed to improve the capacity retention on cycling.

Fig 4.18 shows the corresponding data for HT-$LiCoO_2$ (current densities : 0.1 mA/cm^2 on charge, 0.2 mA/cm^2 on discharge, electrolyte : 1M $LiClO_4$ in PC).

Two differences between the cycling data of LT-$LiCoO_2$ and HT-$LiCoO_2$ cells are evident. Firstly significant capacity is obtained below 3.9V on charge for LT-Li_xCoO_2 in contrast to the high temperature analogue where most of the capacity is obtained above 4V. The average discharge voltage of the LT-Li_xCoO_2 sample is also significantly lower than that of the high temperature analogue. Secondly a very large polarisation voltage of ~0.4V is observed between the charge and discharge curves of LT-Li_xCoO_2 cells. This contrasts with the small polarisation found for Li/HT-Li_xCoO_2 cells (~0.1V). This suggests slow kinetics for the lithium insertion and extraction reactions in LT-Li_xCoO_2 which may possibly be attributed to a number of factors, for example, lower electronic conductivity or lower lithium ion diffusion rates in LT-Li_xCoO_2 compared with HT-Li_xCoO_2 or structural instability in LT-Li_xCoO_2.

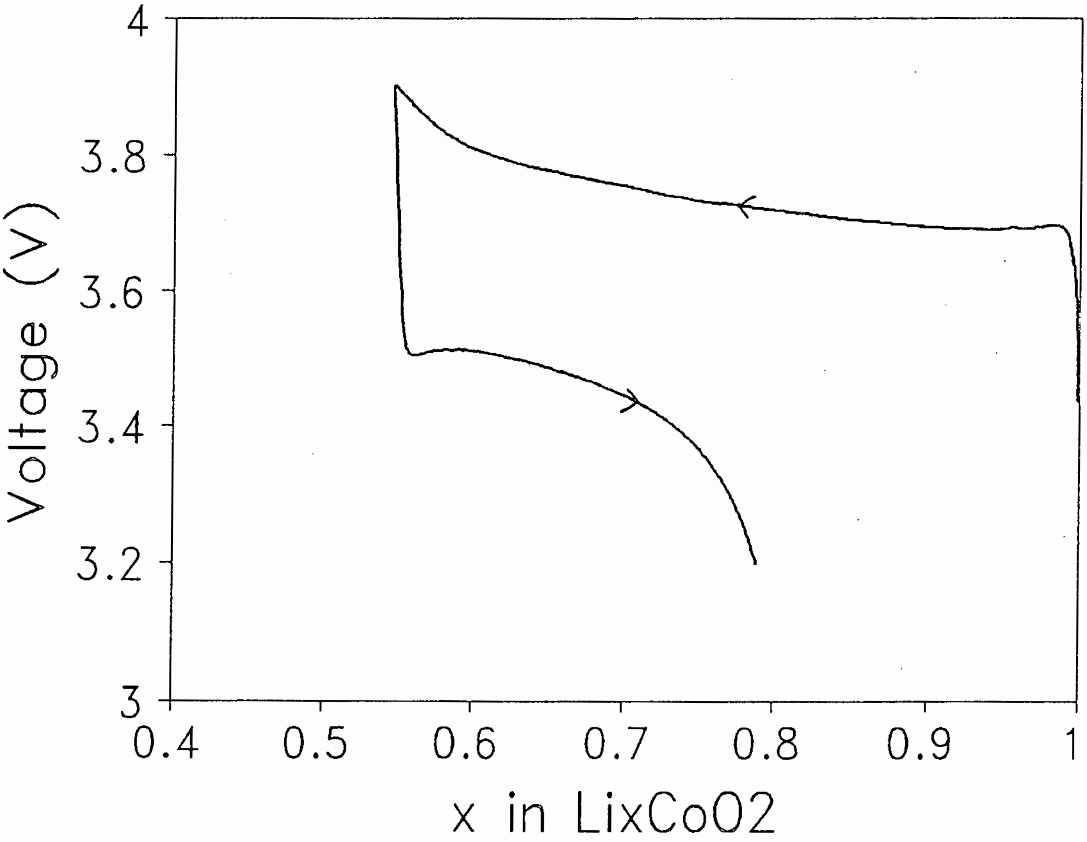

Figure 4.16 : First charge and discharge curves of a Li/LT-$LiCoO_2$ cell. (2.5-3.9V)

Fig 4.19 shows the cycling curves recorded for a Li/LT-$Li_{0.5}CoO_2$ cell using a chemically delithiated sample as the cathode (current densities : 0.1mA/cm^2 on charge, 0.2mA/cm^2 on discharge). The cell was discharged initially to a voltage of 2.5V versus lithium and then cycled between 2.5 and 3.9V. A discharge capacity of 107mAhr/g, corresponding to re-insertion of 0.38 lithiums, was obtained on the first discharge but capacity was lost very rapidly on cycling as was the case for the fully lithiated sample. Fig 4.20 shows the cycling data obtained using a very low current density of 0.02mA/cm^2. This illustrates that approximately 0.5 lithiums can be inserted and extracted from the lattice at this current density on the first cycle; on the second cycle, the capacity of the electrode is reduced by approximately 12%. The polarisation is also considerably reduced at this low rate.

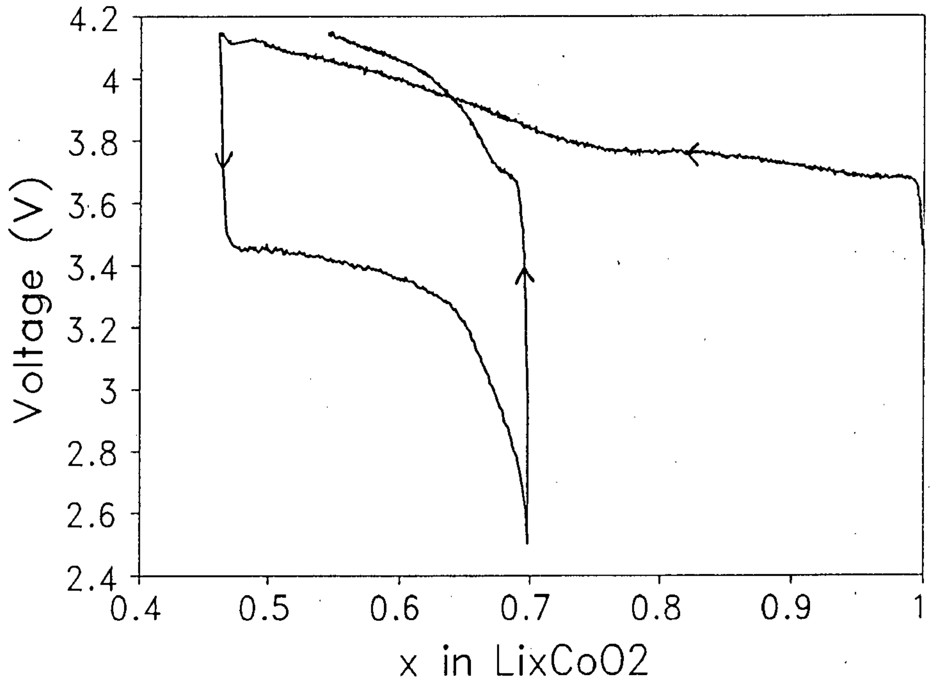

Figure 4.17 : First charge and discharge and 2nd charge curves of a Li/LT-Li_xCoO_2 cell. (2.5-4.2V).

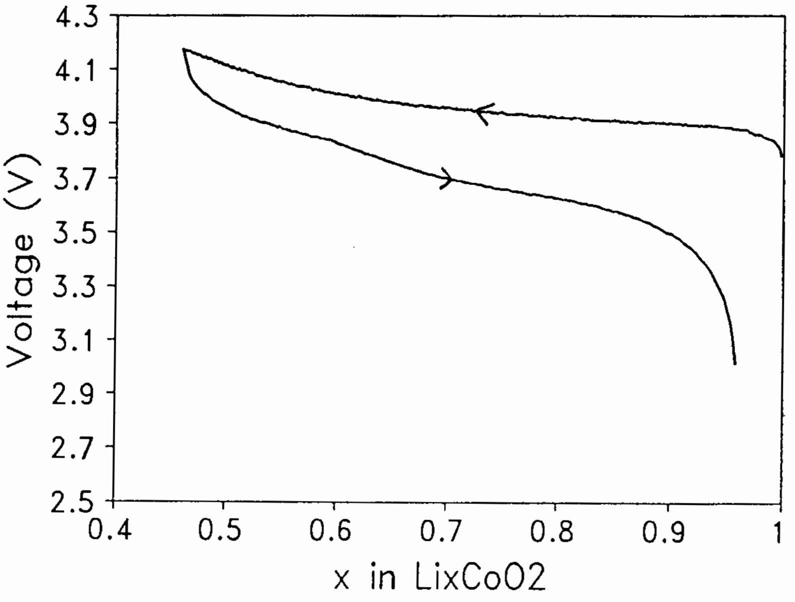

Figure 4.18 : First charge and discharge curves of a Li/HT-Li_xCoO_2 cell.

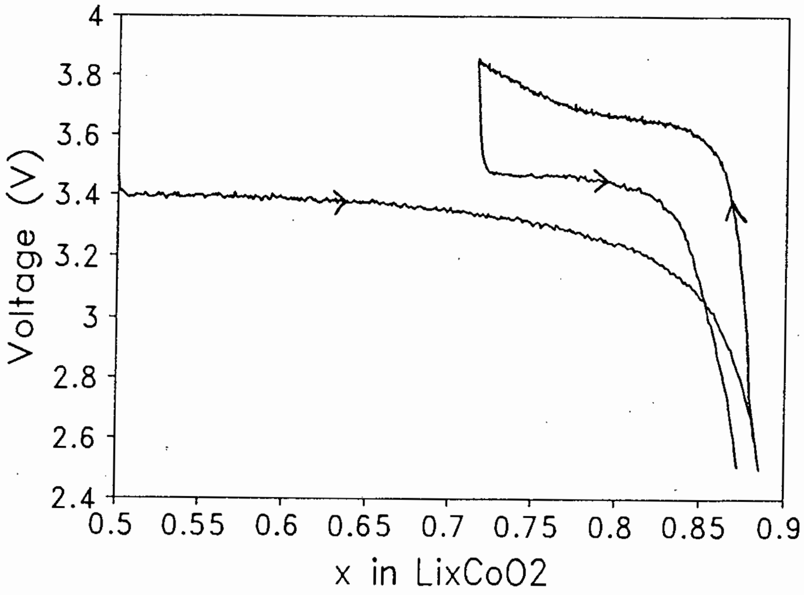

Figure 4.19 : First discharge and charge and 2nd discharge curves of a Li/LT-$Li_{0.5}CoO_2$ cell.

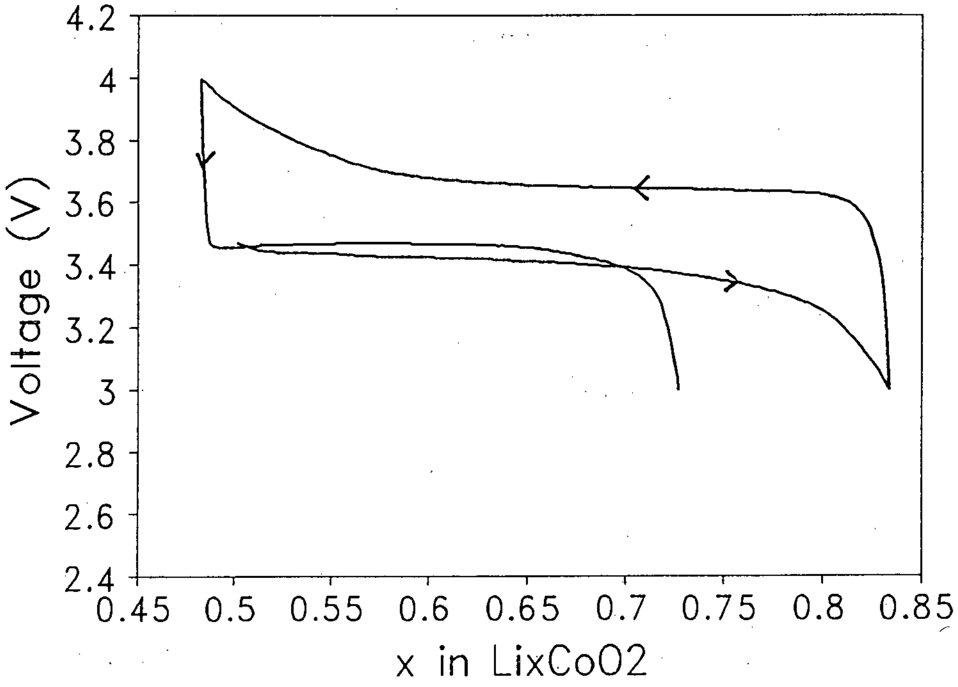

Figure 4.20 : First discharge and charge and 2nd discharge curves of a Li/LT-$Li_{0.5}CoO_2$ cell (0.02 mA/cm^2).

4.6 LITHIUM DIFFUSION RATES

An attempt was made to measure the chemical diffusion coefficient of lithium in LT-$LiCoO_2$ using the AC impedance technique. The observed complex plane impedance response is illustrated in Fig.4.21. The AC impedance spectrum does not show the response expected for a simple Randles circuit (Section 2.6). The semi-circle at high frequency is flattened and the low frequency tail is poorly defined and not at an angle of 45°. The AC impedance spectrum of a HT-Li_xCoO_2 cell for x=0.5 is illustrated in Fig.4.22, for comparison. The calculated chemical diffusion coefficient in this case was $4.6x10^{-8}$ cm^2s^{-1} in excellent agreement with the data of Bruce et al[16].

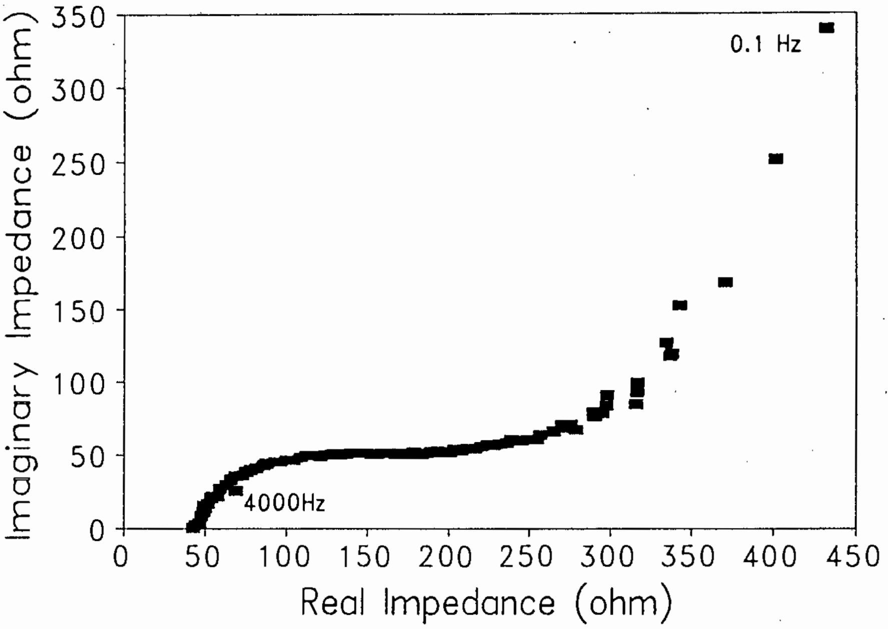

Figure 4.21 : Complex plane impedance spectrum of a Li/LT-$Li_{0.9}CoO_2$ cell.

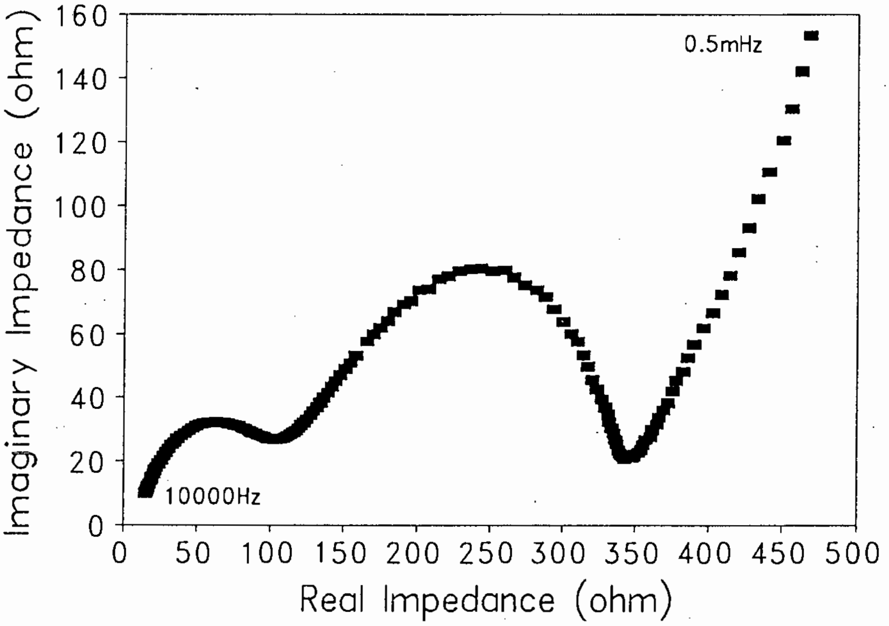

Figure 4.22 : Complex plane impedance spectrum of a Li/HT-$Li_{0.5}CoO_2$ cell. OCV=4.05V, Surface Area=$2.9\times10^{-5}m^2$, dV/dx=0.82, A_w=10.2

As discussed in previous sections the LT-Li_xCoO_2 cathode is two-phase over the composition range $0.95>x>0.2$. The difficulty in measuring diffusion rates in two-phase systems has been discussed by Honders et al[116] with reference to the Ag_xNiPS_3 system. When a phase transition is fast no overvoltage response can be observed in the two-phase region and when the phase transition is slow, it is assumed that the kinetic properties of the phase that accommodates the guest ions most readily will be measured. If the two processes interfere then the impedance of the cell also includes terms containing the rate constants of the phase transitions and it is not possible to formulate the mathematics of the problem. This was found to be the case for Ag_xNiPS_3 and it appears that a similar problem occurs in the case of LT-Li_xCoO_2.

The diffusion rate of lithium in LT-Li_xCoO_2 is expected to be significantly lower than that in HT-Li_xCoO_2. The rapid lithium ion mobility observed in Li_xCoO_2 and Li_xNiO_2 compounds has been attributed to the almost perfect layering of the lithium and transition metal cations into alternate layers of octahedral sites in the crystal lattice as well as to the c-axis degree of freedom in the $R\bar{3}m$ structure[16]. LT-Li_xCoO_2 has a structure in which about 6% of the cobalt cations occupy the lithium-rich layers and these large transition metal cations would be expected to impede the diffusion of lithium ions in the lithium layer. In a similar fashion, interlayer-Ti atoms in the CdI_2 structure of $Ti_{1+x}S_2$ have been found to impede the motion of lithium ions in the lattice[117].

The formation of a "quasi-spinel" structure on delithiation involves the formation of a structure intermediate between the ideal layered $R\bar{3}m$ and the framework structure of interconnected 8a and 16c interstitial sites of the Fd3m spinel space group. Although the Li-ion diffusion in an ideal spinel lattice may be anticipated to be rapid, for example in $LiMn_2O_4$ $\tilde{D}=1\times10^{-9}$ cm^2/s [15], the imperfect "quasi-spinel" does not have a well-defined network of sites for lithium ion diffusion, thereby accounting for the observed sluggishness of lithium in the structure.

4.7 THERMAL ANALYSIS

Figs.4.23 (a-c) show the TGA curves for HT-$LiCoO_2$, LT-$LiCoO_2$ and LT-$Li_{0.4}CoO_2$ (prepared chemically). The TGA curve for the HT-$LiCoO_2$ shows no peaks which is indicative of the stability of this well-ordered layered $LiCoO_2$ structure. The TGA curve for the LT-$LiCoO_2$ material shows a weight loss of 1.65 % between 110 and 350 °C. The origin of this weight loss is uncertain; for T<200°C it is believed to be due to the loss of surface water and, for 200°C<T<750°C to loss of oxygen. Oxygen non-stoichiometry has been found in lithium manganese oxides synthesised at 300-400°C and the excess oxygen is lost when the materials are heated to elevated temperatures, e.g.

$$Li_2Mn_4O_9 \rightarrow 2\ LiMn_2O_4 + 0.5\ O_2$$

It is therefore possible that synthesis of LT-$LiCoO_2$ at 400°C may result in a product that is very slightly oxygen rich, i.e. in which the valency of the cobalt cations is $3+\delta$. This could, however, not be detected in the neutron-diffraction experiments.

Figs 4.24(a-c) shows the X-ray diffraction patterns obtained for the LT-$LiCoO_2$ starting material and that of samples heated to 600 and 900°C respectively. The structure of the LT-$LiCoO_2$ transforms to that of the HT-$LiCoO_2$ as the temperature is raised. When the sample is heated to 600°C, the X-ray diffraction pattern shows the onset of the splitting of the (006) and (012), and the (110) and (108) peaks, indicative of a loss of the pseudo-cubic symmetry of LT-$LiCoO_2$. The product obtained after heating the LT-$LiCoO_2$ to 900°C has the HT-$LiCoO_2$ structure.

The TGA curve of the LT-$Li_{0.4}CoO_2$ material shows a slow initial drop in mass followed by a rapid drop at 350°C of 6.8%. Figs 4.25(a-d) show the X-ray diffraction patterns of LT-$Li_{0.4}CoO_2$ heated to several different temperatures. It appears that heating the sample to temperatures below 200°C does not alter the crystal structure. However, heating to temperatures greater than 200°C results in a two-phase material with the decomposition of the starting material to yield a Co_3O_4 spinel-type material, in which Co^{2+} ions replace Li^+ ions on the tetrahedral sites, as evident from the appearance of the (220) spinel peak at approximately 32° 2θ.

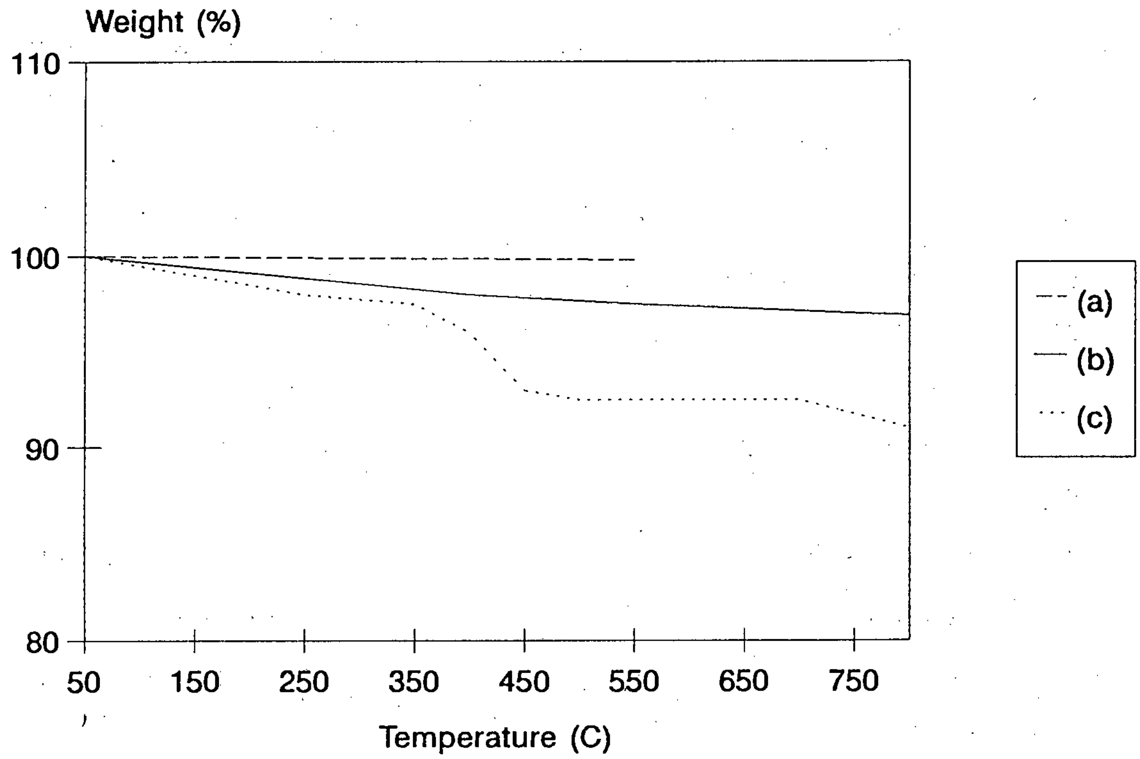

Figure 4.23 : TGA results for a) HT-$LiCoO_2$, b) LT-$LiCoO_2$ and c) LT-$Li_{0.4}CoO_2$ (chemically delithiated).

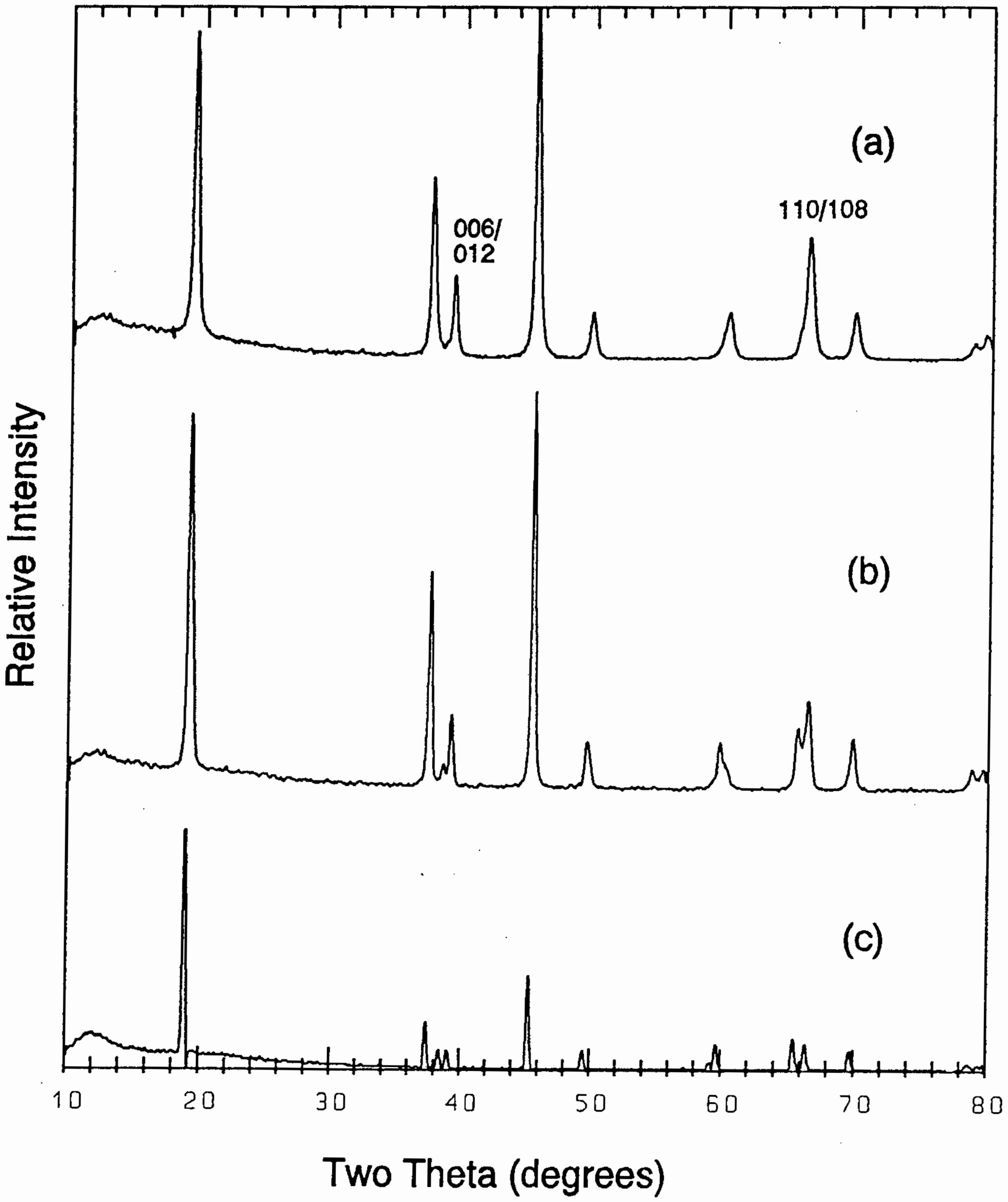

Figure 4.24 : X-ray diffraction patterns of a) $LiCoO_2$ (400°C) b) $LiCoO_2$ (600°C) and c) $LiCoO_2$ (900°C)

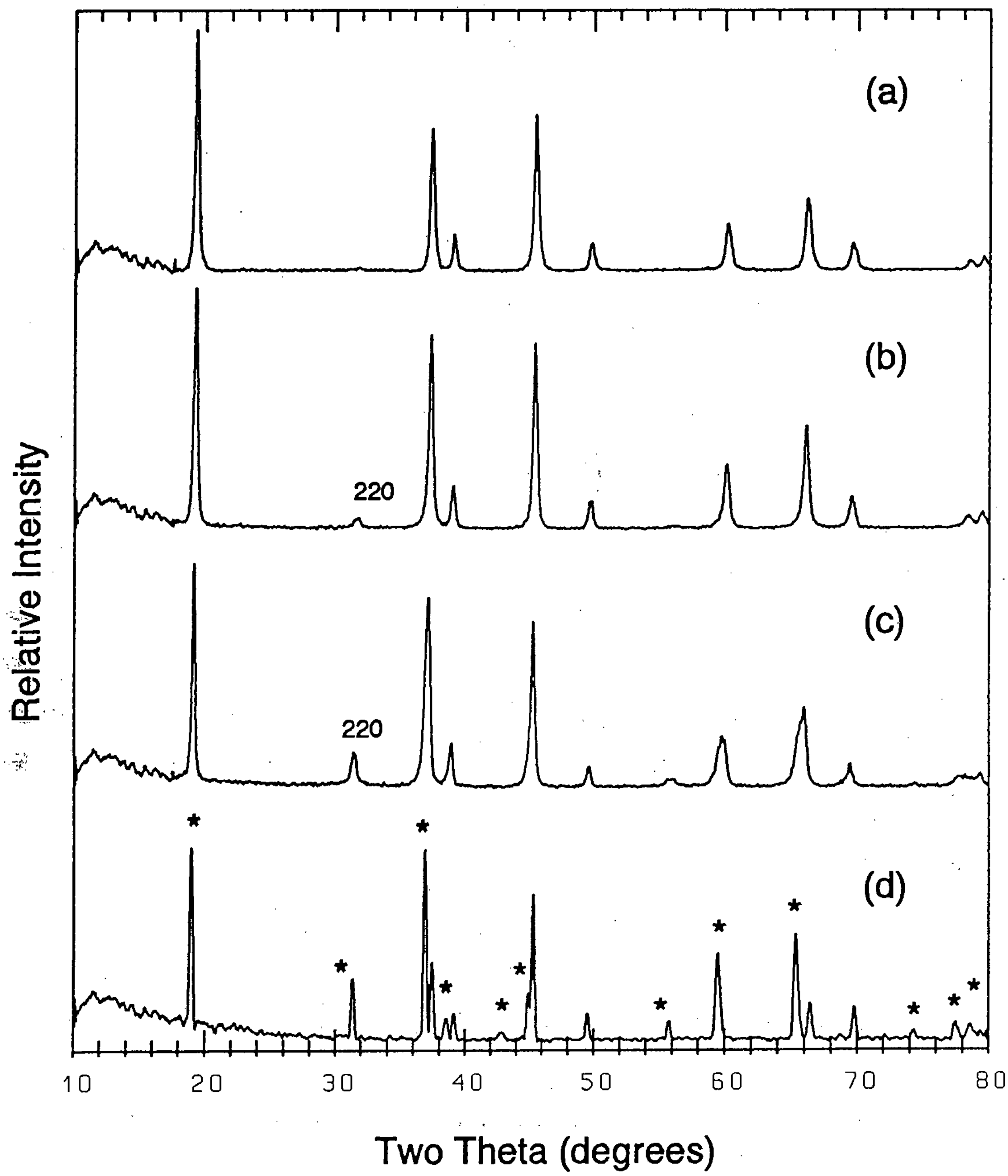

Figure 4.25 : Powder X-ray diffraction patterns of a) LT-$Li_{0.4}CoO_2$ and LT-$Li_{0.4}CoO_2$ heated to b) 250°C, c) 300°C and d) 900°C respectively. *=Co_3O_4 peaks.

If the decomposition reaction which occurs at 350°C is:-

$$Li_{0.4}CoO_2 \rightarrow 0.2\ Co_3O_4 + 0.4\ LiCoO_2 + 0.2\ O_2$$

then the expected weight loss is 6.8%, which is in fairly good agreement with the observed weight loss of 7.8%. The X-ray diffraction pattern of LT-$Li_{0.4}CoO_2$ heated to 900°C clearly shows a two-phase mixture of Co_3O_4 and $LiCoO_2$. (Fig 4.25(d))

4.8 CONCLUSIONS

A novel form of lithium-cobalt-oxide, LT-$LiCoO_2$, has been synthesised at 400°C. This compound demonstrates, for the first time, the existence of significant disorder (6%), of the lithium and cobalt cations in the 3a and 3b octahedral sites of the $R\bar{3}m$ lattice of $LiCoO_2$. The standard, high-temperature $LiCoO_2$, HT-$LiCoO_2$, contains, at most, 2% of cobalt cations in the lithium layers of octahedral sites in the $R\bar{3}m$ lattice[62] (3a sites).

The structural modification of LT-$LiCoO_2$ has a profound effect on its electrochemical properties. HT-$LiCoO_2$ delivers most of its capacity above 4V on charge. LT-$LiCoO_2$, by contrast, gives a two-phase constant-voltage plateau at 3.6V in the OCV curve, for $0.2<x<0.95$ in Li_xCoO_2. This 0.4V drop in operating voltage makes LT-$LiCoO_2$ cathodes attractive as electrodes in rocking-chair cells. One of the major disadvantages of HT-$LiCoO_2$ cathodes are their high voltages versus lithium at low lithium contents (>4V versus lithium) which are outside the electrolyte stability window of most commonly used electrolytes. LT-$LiCoO_2$ cathodes, operating at lower voltages, are therefore potentially more stable on prolonged cycling in organic electrolytes.

Neutron diffraction refinement of the structure of a chemically delithiated sample, LT-$Li_{0.4}CoO_2$, has shown that it is spinel-like. This is the first indication that a normal $LiCo_2O_4$ spinel, isostructural with LiM_2O_4 spinels (M=Mn,V and Ni), may be synthesised. Although the B_2X_4 framework exists in other cobalt spinels, for example, Co_3O_4 and $ZnCo_2O_4$, the normal $LiCo_2O_4$ spinel has not been reported, until now.

The lattice constant obtained for the LT-$Li_{0.4}CoO_2$ ($Li_{0.8}Co_2O_4$) spinel, a=7.991Å, is somewhat smaller than that of other stoichiometric LiM_2O_4 spinels e.g. $LiMn_2O_4$, a=8.242(1)Å[47], LiV_2O_4 a=8.240(1)Å[45] and $LiNi_2O_4$ a=8.190(1)Å[52]. The structural study did, however, show that the B_2X_4 framework in the LT-$Li_{0.4}CoO_2$ compound was not ideal; some lithium cations were found to occupy the 16d sites of the spinel lattice.

The chemically-delithiated LT-$Li_{0.4}CoO_2$ compound with the spinel structure, showed fairly good reversibility when cycled versus lithium at low current rates in the range $0.5 \leq x \leq 0.85$ in Li_xCoO_2. The discharge voltage was ~3.4V over almost the entire composition range. This represents a significant increase in average discharge voltage compared to the spinel $Li_xMn_2O_4$ which discharges at ~3.0V $1 \leq x \leq 2$. A spinel cathode with an average discharge voltage of 3.4V could be useful as a cathode in rocking-chair cells as its discharge voltage is well within the electrolyte stability window of organic electrolytes.

The cycling data obtained with LT-Li_xCoO_2 cathodes does not, as yet, compare favourably with that of HT-$LiCoO_2$ cathodes in terms of specific capacity and reversibility. Further work is required to stabilise the spinel framework in LT-Li_xCoO_2 compounds before they can be regarded as practical alternatives to HT-$LiCoO_2$ cathodes in rocking-chair cells. One possible way of achieving this is to dope LT-$LiCoO_2$ with other transition metal cations, for example, nickel. This possibility is explored in the following chapter.

CHAPTER 5

LITHIUM COBALT NICKEL OXIDES

5.1. INTRODUCTION

$LiCoO_2$ and $LiNiO_2$ synthesised at 800-900°C have been investigated as cathodes for rechargeable lithium batteries. However both of these materials have disadvantages. Li_xCoO_2, as discussed in Chapter 4, has a very high voltage versus lithium at low lithium contents which is outside the electrochemical stability window of most electrolytes.[66] $LiNiO_2$ on the other hand has a lower voltage versus lithium and cycles below 4.0V for $0.5<x<1.0$ avoiding problems of electrolyte oxidation[67]. Nickel is also more abundant than cobalt and, as a cathode material, is already familiar within the battery industry since nickel oxyhydroxide electrodes are used in nickel-cadmium cells. In Li/Li_xNiO_2 cells, it has been shown that lithium may be extracted from $LiNiO_2$ to yield lithium deficient Li_xNiO_2 phases while retaining the rocksalt structure, at least for $0.5<x<1.0$ [51]. In this respect, Li_xNiO_2 electrodes have been shown to be promising candidates for rocking-chair cells using carbon anodes[67]. However, it is comparatively difficult to synthesise $LiNiO_2$ with the desired stoichiometry; products are generally lithium deficient and can be characterized by the formula $Li_{1-x}Ni_{1+x}O_2$ [55,58].

$LiCo_{1-y}Ni_yO_2$ $(0<y<1)$ compounds have been studied to overcome the difficulties associated with pure cobalt or nickel compounds by combining the advantages of both systems.

$LiCo_{1-y}Ni_yO_2$ compounds synthesised at high temperatures have been studied by several previous investigators. Ohzuku et al[68] reported on a range of samples with $0\leq y\leq 0.5$ synthesised from carbonates in air at 900°C for 24 hours. They report that for $y=0.5$ a product isostructural with $LiCoO_2$ but with slightly larger lattice parameters (a=2.849(1)Å and c=14.152(1)Å) is synthesised and for $0<y<0.5$ mixtures of $LiCoO_2$ and $LiCo_{0.5}Ni_{0.5}O_2$ are formed. The working voltage of $Li_xCo_{0.5}Ni_{0.5}O_2$ is approximately 0.5 V lower than that of Li_xCoO_2 in the latter half of the discharge curve.

Delmas and Saadoune[118] have studied the system $LiCo_{1-y}Ni_yO_2$ ($0 \leq y \leq 1$) and report that a solid solution was obtained for the whole y range by firing stoichiometric mixtures of Li_2CO_3, NiO and Co_3O_4, firstly in air at 500°C for a few hours, and then for 48 hours under oxygen at 800-1000°C, depending on the y-value. All the compounds have $R\bar{3}m$ symmetry although the possibility of partial disorder of lithium ions and transition metal ions in alternate layers of octahedral sites cannot be discounted. The reversibility of samples with y=0.7-0.9 was reported and was shown to be superior to that of $LiNiO_2$.

An extensive study of $LiCo_{1-y}Ni_yO_2$ compounds for $0.5 \leq y \leq 1.0$ has been published in the patent literature indicating their superior cycling performance compared to either $LiCoO_2$ or $LiNiO_2$ [119].

As discussed in Chapter 4 synthesis of $LiCoO_2$ at 400°C leads to the formation of a novel $LiCoO_2$ phase, LT-$LiCoO_2$ (LT=low temperature), with a modified structure and significantly different electrochemical properties compared to HT-$LiCoO_2$ prepared at 900°C (HT=high temperature). In this study, the effect of nickel dopants on the structural and electrochemical properties of LT-$LiCoO_2$ is investigated. In particular, the aim of the study is to enhance the cycling stability of the compounds in lithium cells by the addition of nickel dopants. Compounds in the solid-solution $LiCo_{1-y}Ni_yO_2$ ($0 \leq y \leq 0.5$) synthesised at 400°C are investigated.

The possibility of synthesising a LT-$LiNiO_2$ compound isostructural with LT-$LiCoO_2$ is also examined.

5.2 EXPERIMENTAL

Cobalt-nickel compounds, $LiCo_{1-y}Ni_yO_2$, were synthesised by reacting stoichiometric quantities of Li_2CO_3, $CoCO_3$ and $Ni(NO_3)_2.6H_2O$ in air at 400°C for 2 to 5 days for the range $0<y \leq 0.5$. The precursors were mixed in hexane in a mortar and pestle or, in the

case of $LiCo_{0.9}Ni_{0.1}O_2$, ball-milled, prior to firing.

Samples of LT-$LiCo_{0.9}Ni_{0.1}O_2$ and LT-$LiCo_{0.8}Ni_{0.2}O_2$ were also heated to 900°C for 24 hours to form the high temperature analogues.

Samples of LT-$LiCo_{0.9}Ni_{0.1}O_2$ and LT-$LiCo_{0.8}Ni_{0.2}O_2$ were chemically delithiated by acid-leaching; 1g of the sample was added to 15ml of H_2O and 5ml of 5N H_2SO_4 and the mixture was stirred at room temperature for 3 hours. The samples were filtered, washed with distilled water and dried in a drying oven at 80°C for 24 hours. Lithium, cobalt and nickel contents in the delithiated samples were determined with atomic absorption spectroscopy.

Lithium nickel oxides were prepared by reacting $LiNO_3$ and $Ni(NO_3)_2.6H_2O$ with a 1:1 Li:Ni ratio. The salts were initially dissolved in about 50ml of water. The water was evaporated to dryness. Three samples were then prepared by heating the mixture at 400°C for 24 hours (Sample A), 800°C for 3 hours (Sample B) and 800°C for 24 hours (Sample C) respectively.

Two-electrode prismatic Li/LT-$LiCo_{1-y}Ni_yO_2$ cells were galvanostatically charged and discharged. The anodes consisted of lithium foil pressed onto a stainless steel current collector. The cathodes were prepared by intimately mixing a 1:2 teflon:acetylene black mixture (TAB) with $LiCo_{1-y}Ni_yO_2$ materials to give an active cathode content of 80 weight percent. The current density on charge was 0.1 mA/cm^2 and on discharge 0.2mA/cm^2. The electrolyte used was 1M $LiClO_4$ in 1:1 propylene carbonate : dimethoxyethane.

Open-circuit-voltage (OCV) data for a cell containing a LT-$LiCo_{0.9}Ni_{0.1}O_2$ electrode were recorded against a $LiMn_2O_4$ spinel anode which also served as a reference electrode. The suitability of $LiMn_2O_4$ as a constant voltage, reference electrode is discussed in Section 3.4.5. Approximately 25 mg of $LiMn_2O_4$ and about 10 mg of $LiCo_{0.9}Ni_{0.1}O_2$, both mixed with TAB, were used for the anode and cathode, respectively. Lithium was extracted intermittently from the cathode by charging the cell for 1 hour at 0.02 mA and thereafter allowing the cell to equilibrate for five hours, until a composition $Li_{0.01}Co_{0.9}Ni_{0.1}O_2$ was reached.

5.3. RESULTS

5.3.1 X-ray diffraction of LT-$LiCo_{1-y}Ni_yO_2$ samples

Powder X-ray diffraction patterns of LT-$LiCo_{1-y}Ni_yO_2$ compounds for y=0.0, 0.1, 0.2, 0.3 and 0.5 are shown in Fig 5.1 (a-e). LT-$LiCo_{0.9}Ni_{0.1}O_2$ (Fig. 5.1 b) appears to be an essentially single-phase product which is similar to LT-$LiCoO_2$ (Fig. 5.1a) both in peak positions and in the relative intensities of the peaks. For $y \geq 0.2$ (Fig. 5.1 c,d and e) a second phase becomes evident in the X-ray diffraction patterns. This phase is attributed to a disordered rock salt compound in the system $Li_yNi_{1-y}O$ ($0<y<0.3$). Peaks of the second phase are indicated with an asterisks in Fig 5.1e. The lattice parameter of the rock salt compound refined to a=4.156Å, which corresponds to $y \approx 0.11$ [120]. It is possible, however, with improved mixing of the starting materials, for example, by ball-milling, that the concentration of the $Li_yNi_{1-y}O$ phase can be reduced in the final product.

Fig 5.2 shows the powder X-ray diffraction patterns of the high temperature $LiCo_{1-y}Ni_yO_2$ (y=0.1 and 0.2) compounds. Both samples show a small rocksalt impurity of the type $Li_yNi_{1-y}O$ as found in the low temperature samples indicating that less than the desired amount of nickel was incorporated into the $LiCo_{1-y}Ni_yO_2$ structure. This confirms the recent report that it is difficult to synthesise single phase $LiCo_{1-y}Ni_yO_2$ compounds with high cobalt content at high temperatures[118].

All samples were indexed to a trigonal unit cell ($R\bar{3}m$) by analogy with HT-$LiCoO_2$ and HT-$LiNiO_2$. The *a* and *c* lattice parameters of the nickel-doped compounds are given in Table 5.1. Nickel doping of low temperature compounds results in a marginal increase in the *a* and *c* lattice parameters. In these materials the nickel and cobalt cations are in the low spin state and the Co^{3+} (t_2^6) ion is smaller than the Ni^{3+} ($t_2^6e^1$) ion. The *c/a* ratio is 4.90 within experimental error, that is, the ratio expected for an ideal cubic close packed lattice, in sharp contrast to the values obtained for HT-$LiCo_{1-y}Ni_yO_2$ compounds. This suggests that the structures adopted by LT-$LiCo_{1-y}Ni_yO_2$ samples are similar to the structure of LT-$LiCoO_2$ (see Section 4.4). Equivalent lattice parameters for a face-centred cubic unit cell (Fd3m) are given in Table 5.1 for low temperature samples.

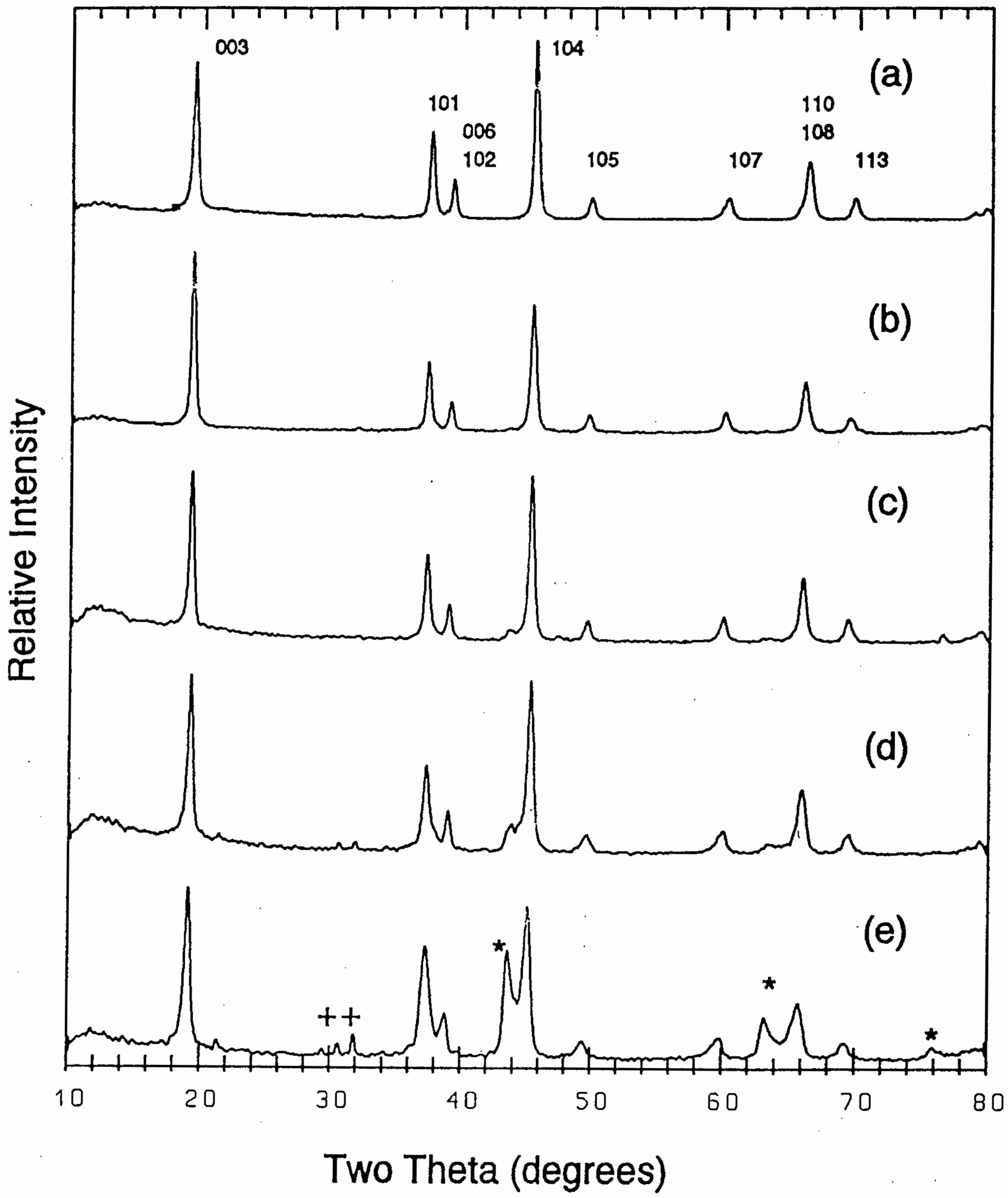

Figure 5.1 : X-ray diffraction patterns of LT-$LiCo_{1-y}Ni_yO_2$ samples a) y=0, b) y=0.1, c) y=0.2, d) y=0.3 and e) y=0.5. *=$Li_yNi_{1-y}O$, +=impurity.

It has been shown that for HT-$LiCo_{1-y}Ni_yO_2$ samples the *c* and *a* lattice parameters increase with y and the *c/a* ratio decreases with y to approach 4.90 for $LiNiO_2$; this effect is most marked for y>0.2. It has been postulated that the decrease in *c/a* ratio is due to disorder in the Li/trivalent ion distribution in alternate layers of octahedral sites as y increases[118]. This trend was not evident from the results of this study for high temperature samples probably due to incomplete incorporation of the nickel ions into the layered structure at high temperature.

TABLE 5.1

Crystallographic Parameters of Lithium Cobalt-Nickel Oxides from X-ray Data

Nominal Composition	R$\bar{3}$m			Fd3m
	a(Å)	*c*(Å)	*c/a*	*c*(Å)
LT-$LiCoO_2$	2.830(1)	13.868(4)	4.901(2)	8.006(1)
LT-$LiCo_{0.9}Ni_{0.1}O_2$	2.833(1)	13.881(5)	4.901(3)	8.014(1)
LT-$LiCo_{0.8}Ni_{0.2}O_2$	2.834(1)	13.889(5)	4.900(2)	8.019(1)
LT-$Li_{0.4}Co_{0.9}Ni_{0.1}O_2$	2.826(1)	13.845(5)	4.899(2)	7.993(1)
LT-$Li_{0.4}Co_{0.8}Ni_{0.2}O_2$	2.825(1)	13.837(7)	4.898(3)	7.989(1)
HT-$LiCoO_2$	2.818(1)	14.060(1)	4.989(2)	-
HT-$LiCo_{0.9}Ni_{0.1}O_2$	2.813(1)	14.046(2)	4.993(2)	-
HT-$LiCo_{0.8}Ni_{0.2}O_2$	2.817(1)	14.057(2)	4.990(2)	-

Fig 5.3 shows the powder X-ray diffraction patterns of two chemically delithiated samples of LT-$Li_xCo_{1-y}Ni_yO_2$ y=0.1 and y=0.2 respectively. The near-cubic symmetry of the materials is retained on delithiation as is the case for LT-$LiCoO_2$ samples (Section 4.3.3) but in contrast to the behaviour of HT-$LiCoO_2$ and $LiNiO_2$ where an increase in the *c/a* ratio is observed with decreasing lithium content. Table 5.2 shows the results of chemical analysis of the LT-$Li_xCo_{1-y}Ni_yO_2$ samples, lattice parameters are given in Table 5.1.

Chemical analysis shows a very slight decrease in the cobalt content of the chemically-delithiated $Li_xCo_{1-y}Ni_yO_2$ compounds from the stoichiometric amount. This was attributed to preferential dissolution of cobalt ions (as CoO) to nickel from the lattice during acid-leaching.

TABLE 5.2

Chemically determined composition of LT-$Li_xCo_{1-y}Ni_yO_2$ compounds

Nominal Composition	Li	Co	Ni	Calculated Composition
$Li_xCo_{0.9}Ni_{0.1}O_2$	2.9	54.9	6.3	$Li_{0.4}Co_{0.8}Ni_{0.1}O_2$
$Li_xCo_{0.8}Ni_{0.2}O_2$	3.0	49.2	10.9	$Li_{0.4}Co_{0.7}Ni_{0.2}O_2$

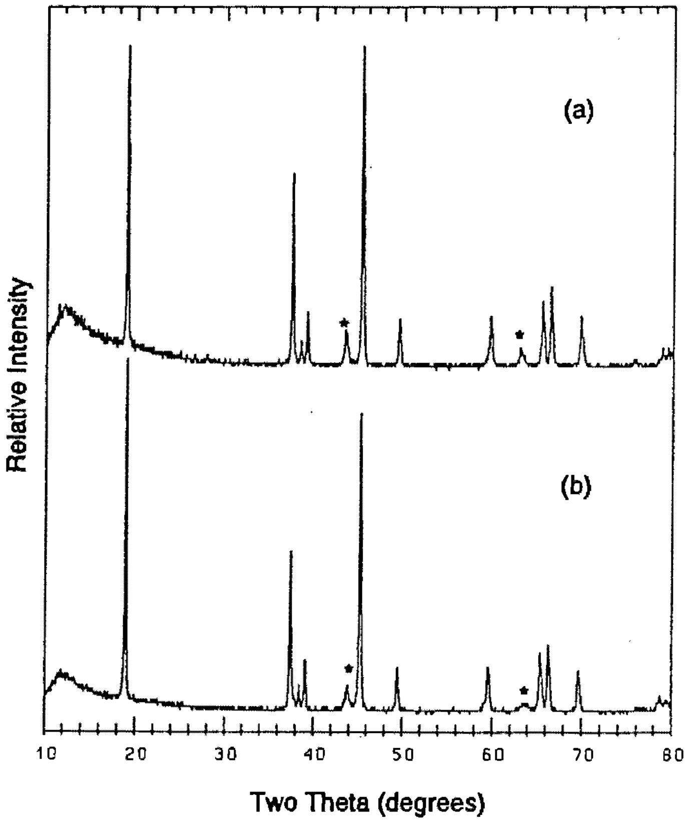

Figure 5.2 : Powder X-ray diffraction patterns of HT-$LiCo_{1-y}Ni_yO_2$ samples a) y=0.1, b) y=0.2. *=$Li_yNi_{1-y}O$

The possibility of synthesising LT-$LiNiO_2$, the nickel analogue of LT-$LiCoO_2$, was also investigated. The product obtained by reaction of $LiNO_3$ and $Ni(NO_3).6H_2O$ at 400°C was a single-phase rock salt compound with refined lattice parameter a=4.177Å, coincident with that of NiO (Fig 5.4a). The unreacted $LiNO_3$, that had apparently

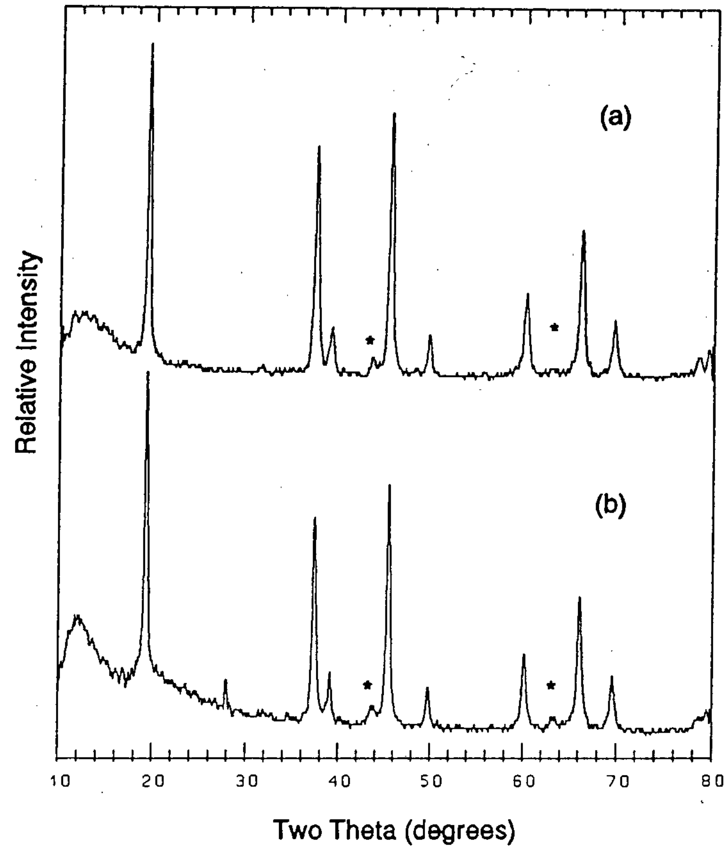

Figure 5.3 : Powder X-ray diffraction patterns of a) LT-$Li_xCo_{0.9}Ni_{0.1}O_2$ and b) LT-$Li_xCo_{0.8}Ni_{0.2}O_2$. *=$Li_yNi_{1-y}O$

decomposed at 400°C, could not be detected in the X-ray diffraction pattern. Goodenough et al.[120] have shown that a random cation distribution can be found in $Li_yNi_{1-y}O$ samples for $y<0.3$ but that at higher y values the lithium and nickel ions begin to separate into alternate layers, particularly when high synthesis temperatures are used (800°C to 840°C).

When the product shown in Fig. 5.4a was heated to 800°C in air for three hours (Sample B), a single phase product with nominal $LiNiO_2$ stoichiometry was formed (Fig. 5.4b). The difficulty involved in synthesising stoichiometric $LiNiO_2$ products has been discussed by several authors [55,58]. The products formed are generally lithium-deficient with composition $Li_{1-x}Ni_{1+x}O_2$. Fig 5.4c shows the powder diffraction pattern of Sample C obtained by heating Sample A at 800°C for 24 hours. The dramatic difference observed in the (102,006)/(101) intensity ratio between Sample B and Sample C indicates a decrease in the Li/Ni ratio with prolonged reaction at elevated temperature. Several authors have reported difficulty in obtaining the desired stoichiometry due to lithium

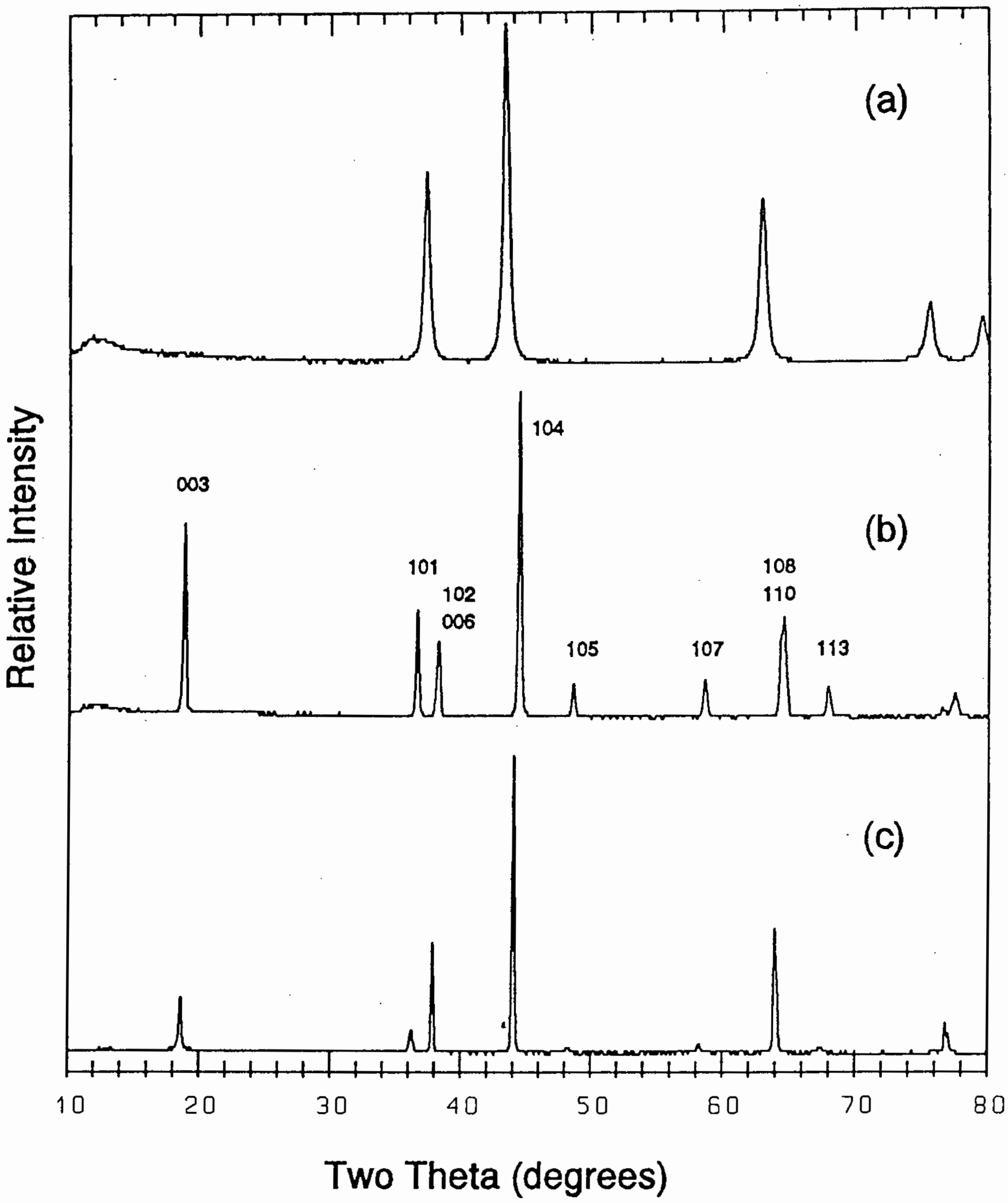

Figure 5.4 : Powder X-ray diffraction pattern of $LiNiO_2$ a) Sample A 400°C, b) Sample B 800°C and c) Sample C 800°C.

volatilisation at high temperatures [59,121].

Dahn et al[41] have demonstrated that the stoichiometry of $Li_xNi_{1-x}O_2$ samples may be calculated from the unit cell volume or from the intensity ratio of the (102,006) peak to that of the (101) peak. Preferred orientation effects in layered compounds could, however, lead to erroneous results. The lattice constants, *c/a* ratio, intensity ratios and derived compositions for samples B and C are given in Table 5.3. These data demonstrate the reduction in the *c/a* ratio of $Li_{1-x}Ni_{1+x}O_2$ compounds with increasing x due to the presence of nickel ions in the lithium-rich layers [58,121].

TABLE 5.3

Lattice parameters and composition of $Li_{1-x}Ni_{1+x}O_2$ compounds

Sample	*a* (Å)	*c* (Å)	*c/a*	I(101)/I(006,102)	**Derived* Composition**
B	2.887(1)	14.221(1)	4.926(2)	0.81(1)	$Li_{0.91}Ni_{1.09}O_2$
C	2.907(1)	14.253(5)	4.903(2)	2.67(1)	$Li_{0.73}Ni_{1.27}O_2$

* Composition obtained from intensity ratio from data of Dahn et al[41].

TABLE 5.4

Crystallographic Parameters of $Li_{0.9}Ni_{1.1}O_2$ (Sample B) from Neutron Diffraction Data

Space Group $R\bar{3}m$ a = 2.887(1)Å, c = 14.221(1)Å c/a = 4.926(2)

ATOM	SITE	POSITION			OCCU- PANCY	B_{11}	B_{22}	B_{33}	B_{12}
		x	y	z					
Li(1)	3a	0	0	0	0.87	1.6(1)	-	-	-
Ni(1)	3a	0	0	0	0.13	0.86(8)	-	-	-
Ni(2)	3b	0	0	0.5	0.97(1)	0.25(1)	-	-	-
Li(2)	3b	0	0	0.5	0.03(1)	0.25(1)	-	-	-
O	3c	0	0	0.242(1)	1.000	0.96(2)	0.53(3)	0.53(3)	0.48(1)

R Factors: R_p = 3.58% R_{wp} = 2.95% R_{exp} = 2.32%

χ^2 = 1.61 for 2080 observations and 24 basic variables.

5.3.2 Structure Determination of $LiNiO_2$

The structure of the sample with nominal composition $LiNiO_2$ (Sample B) was determined from powder neutron diffraction data. Lithium and nickel ions were permitted to occupy both 3a and 3b octahedral sites of the trigonal lattice, space group $R\bar{3}m$. The total occupancy of each octahedral site was, however, constrained to unity. Isotropic temperature factors were assigned to the lithium and nickel ions, whereas the oxygen ions were allowed to vary anisotropically. The neutron-scattering amplitudes used in the structure refinement were $b(Li)=-0.2030 \times 10^{-12}$ cm, $b(Ni)=1.0300 \times 10^{-12}$ cm and $b(O)=0.5805 \times 10^{-12}$ cm. The initial lattice parameters used in the refinement were those obtained from X-ray diffraction data.

The observed and calculated powder neutron diffraction profiles of the $LiNiO_2$ sample are shown in Fig 5.5. The refined cation distribution was found to be $(Li_{0.87}Ni_{0.13})_{3a}[Li_{0.03}Ni_{0.97}]_{3b}O_2$ (Table 5.4) giving an overall stoichiometry $Li_{0.9}Ni_{1.1}O_2$. This is in excellent agreement with the stoichiometry derived from the intensity ratio of (101) to (006/102) peaks (Table 5.3). This gives a mean oxidation state for nickel of 2.82 emphasising the difficulty in completely oxidising Ni^{2+} to Ni^{3+} at 800°C. The excess nickel ions were found to occupy the octahedral sites of the lithium-rich layer confirming the recent X-ray data reported by Morales et al[58]. The *c/a* ratio refined to 4.92(2).

5.4 ELECTROCHEMICAL EVALUATION OF LT-$LiCo_{1-y}Ni_yO_2$

5.4.1 Electrochemical Curve

A plot of the OCV versus composition of a $Li_{1+x}Mn_2O_4/Li_{1-x}Co_{0.9}Ni_{0.1}O_2$ cell is given in Fig 5.6. The use of $Li_{1+x}Mn_2O_4$ as a constant voltage, reference electrode is discussed in section 3.4.5. The data show a plateau in the OCV curve for the range $0.1<x<0.6$ at 0.64 V vs $Li_{1+x}Mn_2O_4$ (or 3.61 V vs pure lithium) indicating a two-phase region. For $x>0.6$ the OCV value increases to reach 1.0 V at $x=0.95$ (or 3.97 V vs pure lithium). This behaviour is similar to that reported for a Li/LT-Li_xCoO_2 cell (Fig 4.10) which delivered a constant OCV of 3.61 V versus lithium for the range $0.05<x<0.95$ when long equilibration times (7 days) were used. However, when short equilibration times were

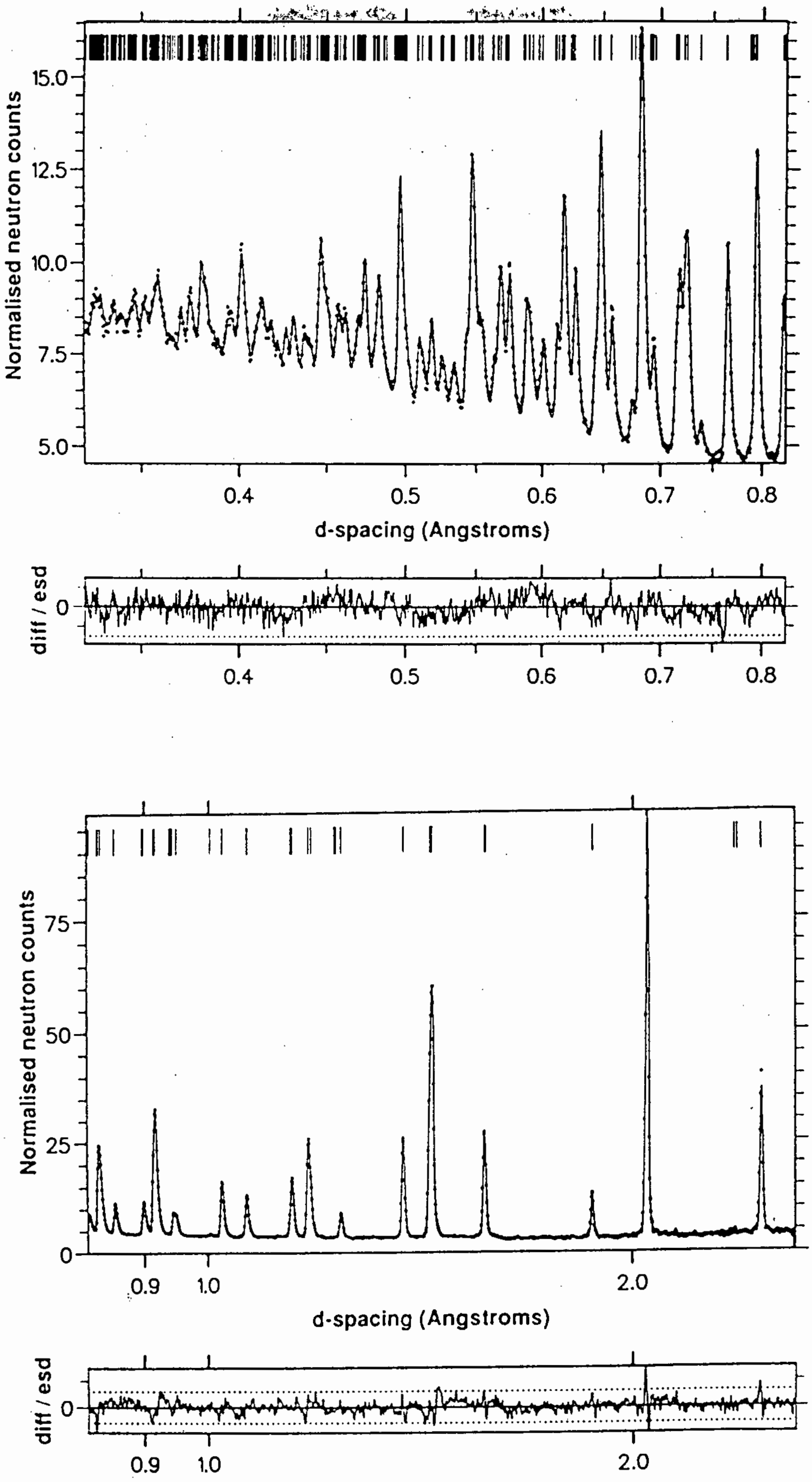

Figure 5.5 : The observed and calculated neutron diffraction profiles of $LiNiO_2$ (Sample B).

used in Li/LT-Li_xCoO_2 cells the two-phase region did not extend beyond x=0.5. The two-phase region in Li/LT-Li_xCoO_2 cells (Chapter 4) has been attributed to a defect rock salt phase in which the cations are located only in octahedral sites and a phase with quasi-spinel character, in which the lithium cations are located in tetrahedral- as well as octahedral sites.

Nickel doping at the 10% level does not depress the open circuit voltage of Li/LT-Li_xCoO_2 cells to any measurable degree.

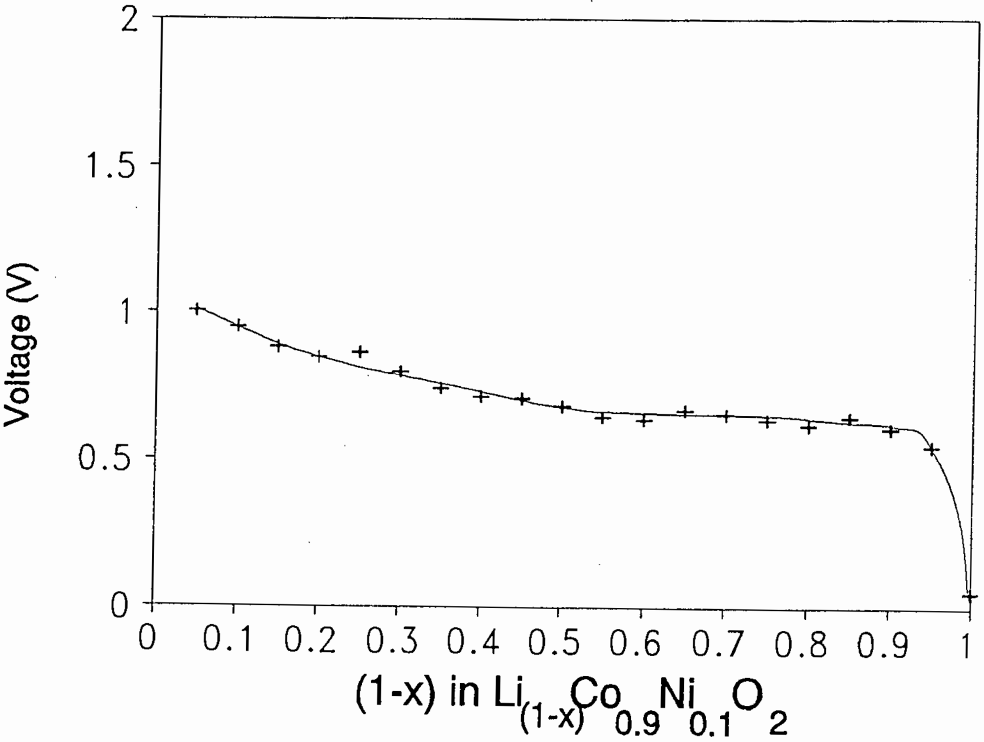

Figure 5.6 : Electrochemical curve of a $Li_{1+x}Mn_2O_4$/LT-$Li_{1-x}Co_{0.9}Ni_{0.1}O_2$ cell.

5.4.2 Cyclic Voltammetry

The cyclic voltammograms of Li/LT-$LiCo_{0.9}Ni_{0.1}O_2$ (Fig. 5.7a) and Li/LT-$LiCo_{0.8}Ni_{0.2}O_2$ (Fig. 5.7b) cells show essentially single step insertion and removal of lithium from the crystal lattice. Very little evidence of the quasi-spinel phase observed in the CV's of Li/LT-$LiCoO_2$ samples, is found. The single-step nature of the insertion and extraction reactions is similar to that found for a chemically-delithiated LT-$Li_{0.4}CoO_2$ sample (Fig

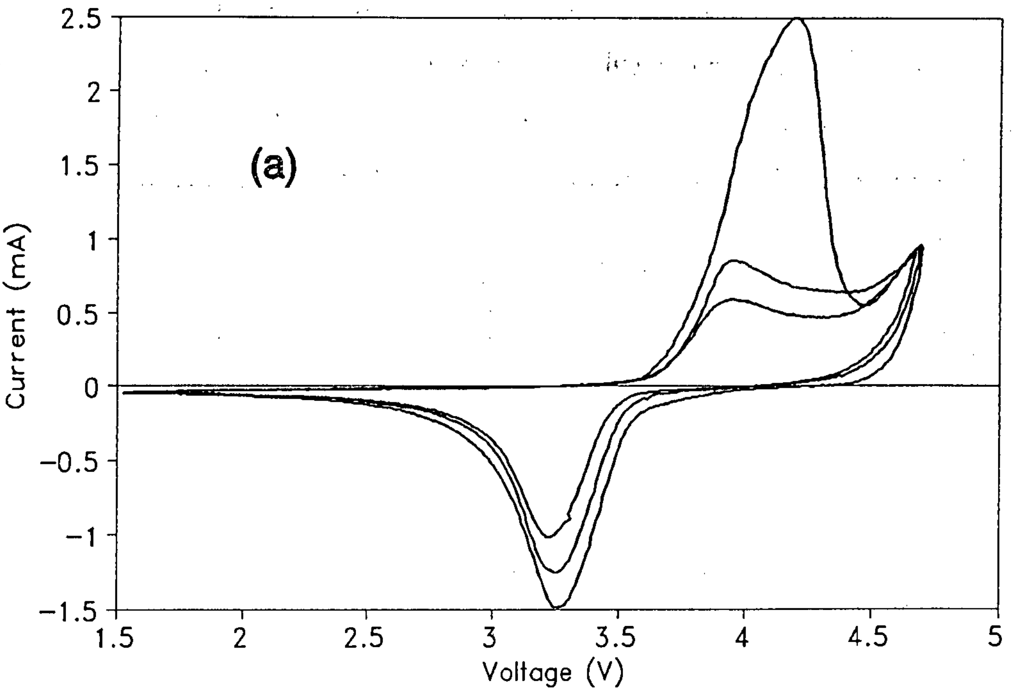

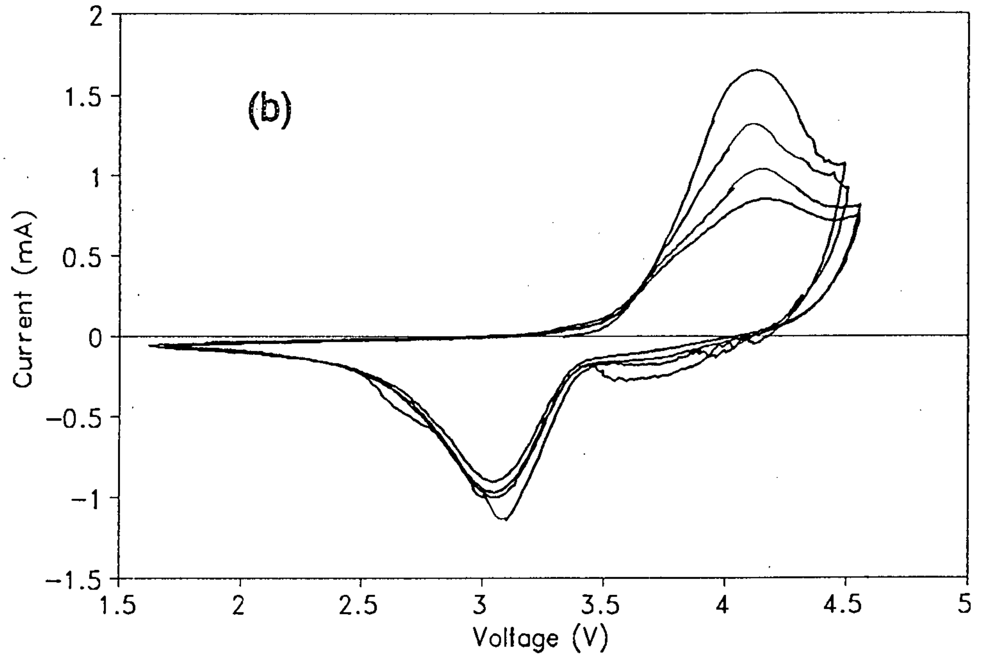

Figure 5.7 : Cyclic voltammograms of Li/LT-$LiCo_{1-y}Ni_yO_2$ cells a) y=0.1 and b) y=0.2. (0.5mV/s)

4.14). Structural analysis showed that LT-$Li_{0.4}CoO_2$ has a defect spinel structure and the anodic and cathodic peaks observed in the cyclic voltammogram were attributed to insertion and removal of lithium ions from the octahedral 16c sites of the spinel B_2X_4 framework by analogy with $LiMn_2O_4$ (Section 4.5.2). On the basis of the similarity of the cyclic voltammograms of the LT-$LiCo_{1-y}Ni_yO_2$ compounds to that of the spinel LT-$Li_{0.4}CoO_2$, it is concluded that the LT-$LiCo_{1-y}Ni_yO_2$ compounds have a similar spinel-related structure.

5.4.3 Galvanostatic Cell-Cycling

Electrochemical studies in lithium cells were carried out to evaluate the performance of LT-$LiCo_{1-y}Ni_yO_2$ electrodes (y = 0.1, 0.2). Typical cycling curves for the first 4 cycles are shown in Figs 5.8a and 5.8b respectively. The most important feature of the data is that the Li/LT-$LiCo_{1-y}Ni_yO_2$ cells discharge most of their capacity at a significantly lower voltage (3.8 V-3.3 V) compared to the Li/HT-$LiCoO_2$ cell (4.4 V - 3.8 V) and HT-Li/LT-$LiCo_{1-y}Ni_yO_2$ cells. By analogy with the LT-$LiCoO_2$ samples this is attributed to the two-phase nature of the cathodes synthesised at low temperatures.

The addition of nickel dopants also improves the stability of the cathodes on cycling in agreement with the findings for Ni-doped HT-$LiCoO_2$ cathodes. The nickel-doped electrodes yield significantly superior initial capacities (100 mAhr/g) compared to LT-$LiCoO_2$ electrodes (65 mAhr/g) when discharged to a cut-off voltage of 2.5 V (see Fig 4.17).

Fig 5.9 shows the cycling curves for 4 cycles obtained for a Li/LT-$Li_{0.4}Co_{0.9}Ni_{0.1}O_2$ cell in a "charged state" initially, in which the cathode had been prepared by acid-leaching. The cell was initially discharged to a voltage of 2.5V and then cycled between 2.5 and 4.2V. Comparison of the data with that of the Li/LT-$LiCo_{0.9}Ni_{0.1}O_2$ cell (Fig 5.8a) shows two important differences. Firstly, the acid-leached material shows significantly flatter charge and discharge curves; the voltage on discharge is approximately 3.4V. Secondly, the stability of the cells on cycling when compared with cells loaded in the "discharged" state with LT-$LiCo_{0.9}Ni_{0.1}O_2$ cathodes is considerably improved.

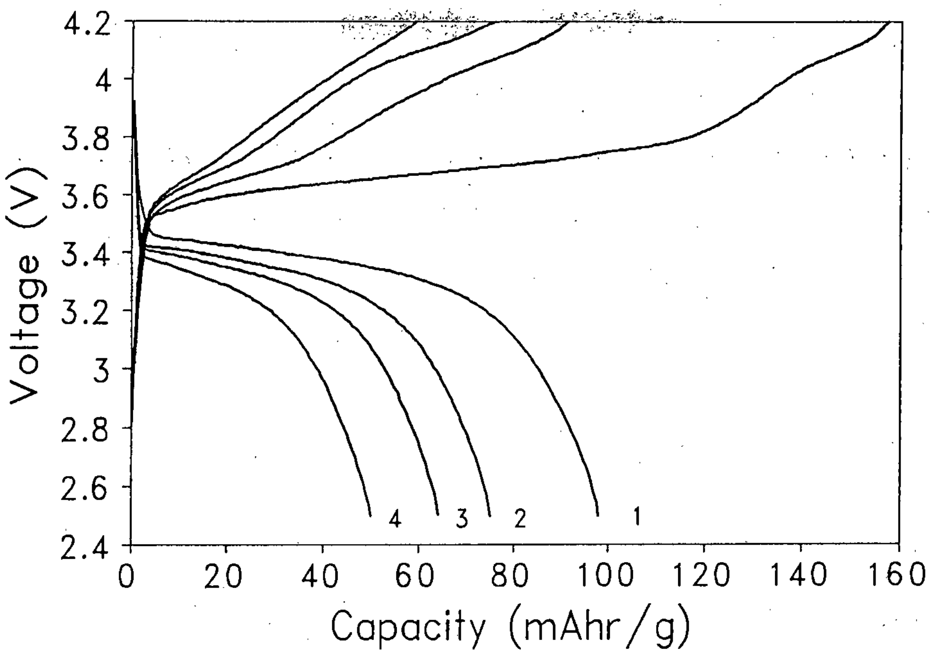

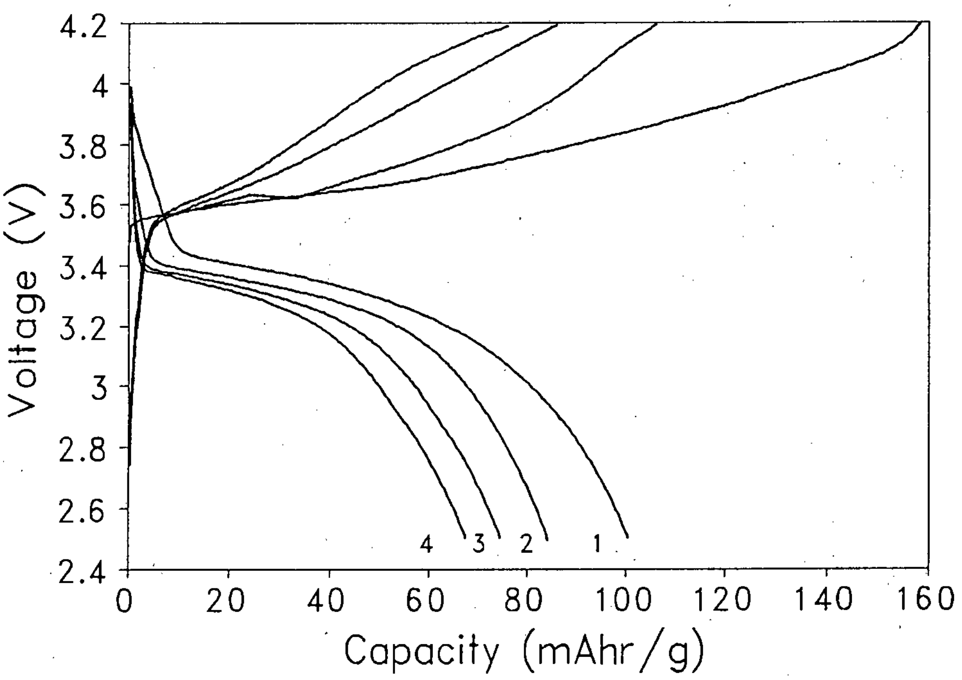

Figure 5.8 : Cycling curves of the following cells: a) Li/LT-$LiCo_{0.9}Ni_{0.1}O_2$ and b) Li/LT-$LiCo_{0.8}Ni_{0.2}O_2$.(2.5-4.2V)

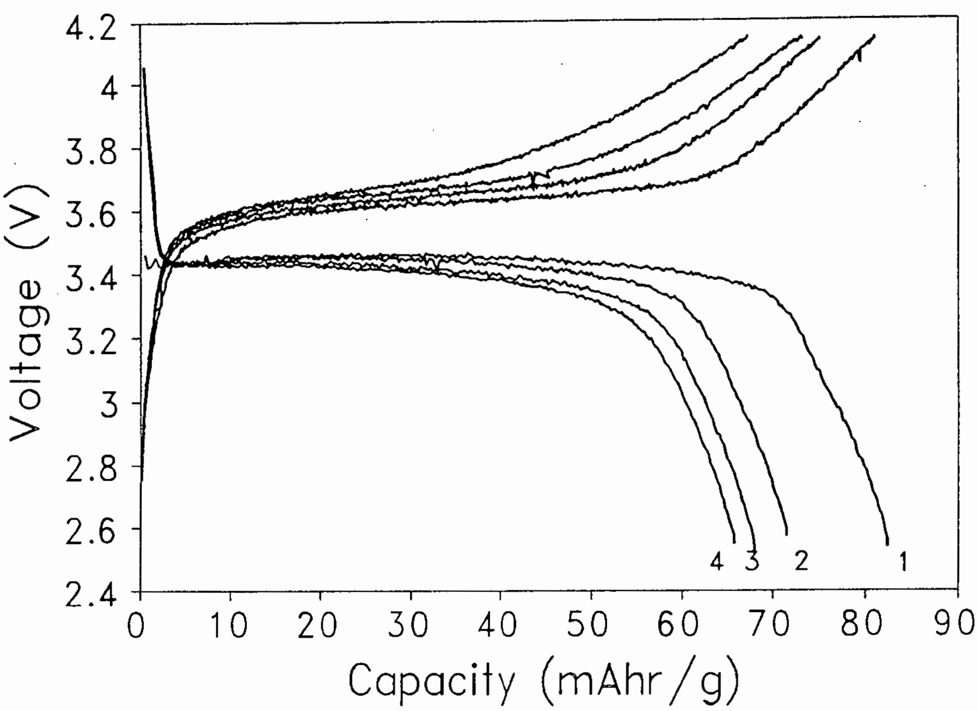

Figure 5.9 : Cycling curves of a Li/LT-$Li_{0.4}Co_{0.9}Ni_{0.1}O_2$ cell (2.5-4.2V)

5.5 CONCLUSIONS

Synthesis of $LiCo_{1-y}Ni_yO_2$ compounds at 400°C results in products which exhibit very similar electrochemical properties to LT-$LiCoO_2$, at least for $y=0.1$ and 0.2. Although no detailed structural refinements of LT-$LiCo_{1-y}Ni_yO_2$ products have been undertaken, the near-cubic symmetry of the lattice, retention of a *c/a* ratio of 4.90 on delithiation and the low OCV of 3.61V versus lithium (for $y=0.1$), all suggest that the structures are similar to that of LT-$LiCoO_2$.

A single-step insertion and removal of lithium was observed in the cyclic voltammograms of LT-$LiCo_{1-y}Ni_yO_2$ cathodes ($y=0.1$ and 0.2). This suggests, by analogy with LT-$Li_{0.4}CoO_2$, that the structures of these compounds are spinel-like. The addition of a minor proportion of nickel (10-20%) has therefore resulted in the stabilisation of the spinel structure in LT-$LiCo_{1-y}Ni_yO_2$ compounds.

The chemically-delithiated sample LT-$Li_{0.4}Co_{0.9}Ni_{0.1}O_2$ shows good reversibility for the first 4 cycles with an average discharge voltage of ~3.4V. The reversibility is superior to that shown by LT-$LiCoO_2$, LT-$LiCo_{0.9}Ni_{0.1}O_2$ or LT-$Li_{0.4}CoO_2$ cathodes. Chemical delithiation of LT-$LiCoO_2$ was shown in Chapter 4 to result in the formation of the spinel lattice in the product, LT-$Li_{0.4}CoO_2$. The addition of 10% nickel therefore stabilises the spinel lattice in LT-$Li_{0.4}Co_{0.9}Ni_{0.1}O_2$ and results in improved cycling properties. A neutron- diffraction refinement of the structure of a LT-$Li_{0.4}Co_{0.9}Ni_{0.1}O_2$ is still required to show unequivocally that this compound has a spinel structure, as indicated by its electrochemical properties.

A spinel cathode with an average discharge voltage of ~3.4V versus lithium and good reversibility on cycling is very attractive as a cathode for a rocking-chair cell. The best cycling performance has been obtained from cells with chemically-delithiated LT-$Li_{0.4}Co_{0.9}Ni_{0.1}O_2$ cathodes which are initially in a "charged state". Further work is required to synthesise a compound in the "discharged state" with a stable lithiated spinel structure, LT-$LiCo_{0.9}Ni_{0.1}O_2$, or in spinel notation LT-$Li_2[Co_{1.8}Ni_{0.2}]O_4$, for the fabrication of carbon/LT-$LiCo_{0.9}Ni_{0.1}O_2$ rocking-chair type cells. This may possibly be achieved by the addition of other transition metal cations as dopants, for example, manganese or vanadium.

CHAPTER 6
LITHIUM MANGANESE OXIDES

6.1 INTRODUCTION

The major limiting factor in the development of practical rechargeable lithium batteries is concern regarding their safety. Dendritic lithium deposited at the anode after prolonged cycling is highly reactive and poses a serious fire hazard if the cells are ruptured. Rocking-chair cells, which contain intercalation compounds as both the cathode and the anode, do not contain metallic lithium and are therefore far safer than conventional intercalation cells. Development of practical rechargeable lithium batteries is therefore focused on the optimisation of rocking-chair cells.

Carbon is a very attractive intercalation anode for rocking-chair batteries. The first charge cycle of the cell involves the transfer of lithium ions from the lithium-rich cathode to the carbon anode. For example, anodes based on petroleum coke offer reversible capacities of ~180 mAhr/g with $\Delta x \approx 0.5$ in Li_xC_6 [15]. However, lithium is always consumed on the first charge cycle of a carbon anode due to irreversible reaction of the lithium with the surface of the carbon. This results in an anode capacity loss of 20-40% on the first charge cycle.

Cathodes for rocking-chair cells using carbon anodes are required to be lithium-rich or in a discharged state initially. Ideally they should also contain an excess of lithium to compensate for the inevitable anode capacity loss on the first charge.

The manganese oxide system offers a wide variety of structural forms that are of interest as intercalation cathodes for lithium batteries. Examples of charged cathodes include α-MnO_2 with the hollandite structure, the defect spinel λ-MnO_2, ramsdellite MnO_2 and γ-MnO_2 which has an intergrowth structure comprised of β-MnO_2 (rutile) and ramsdellite-MnO_2. γ-MnO_2 is used extensively as the cathode in aqueous Zn/MnO_2 batteries, for example, Leclanché cells that use NH_4Cl as electrolyte and alkaline cells that use KOH as electrolyte.

The spinel $LiMn_2O_4$ is currently being investigated as a partially discharged cathode for rocking-chair cells and its structure and electrochemistry have been well characterised by previous authors[42,46-48]. Lithium can be reversibly extracted from $LiMn_2O_4$ to yield the defect spinel $Li_{1-x}Mn_2O_4$ $(0<x<1)$ giving a reversible capacity of approximately 120 mAhr/g at an average voltage of ~4V versus lithium metal. In a rocking-chair cell configuration the cell charge and discharge reactions can be represented by :-

$$12C + LiMn_2O_4 \quad \underset{discharge}{\overset{charge}{\rightarrow}} \quad 2Li_xC_6 + Li_{1-2x}Mn_2O_4 \qquad 0 \leq x \leq 0.5$$

The capacity balance between the cathode and the anode is critical for the successful operation of a rocking-chair cell. The spinel $LiMn_2O_4$ does not contain any excess lithium. In order to compensate for the capacity losses at the anode on the first cycle, an excess of $LiMn_2O_4$ must be used, reducing the specific capacity of the cells. An alternative approach is to synthesise a discharged manganese cathode, $Li_{1+x}Mn_2O_4$ $0 \leq x \leq 1$. The excess lithium contained in this compound could then be used directly to compensate for lithium irreversibly consumed at the anode.

Lithiation of $LiMn_2O_4$ results in a tetragonal product $Li_2Mn_2O_4$ ($LiMnO_2$) and is accompanied by a volume expansion of the lattice of ~6% and a 16% change in the *c/a* ratio[42]. Lithiation can be accomplished either electrochemically or chemically using butyllithium or LiI but $Li_2Mn_2O_4$ cannot be synthesised directly in air. Reaction of lithium and manganese salts or oxides in a 1:1 Li:Mn ratio results in the formation of two-phase mixtures of Li_2MnO_3 and $Li_xMn_{2-z}O_4$ $(0 \leq x \leq 4/3, 0 \leq z \leq 1/3)$ spinels depending on synthesis temperature.

Another well-known $LiMnO_2$ polymorph has orthorhombic symmetry; it is synthesised from Li_2O and Mn_2O_3 in argon at 750°C[122]. The ordered structure of orthorhombic $LiMnO_2$ in which all tetrahedra share faces with at least one manganese-occupied octahedron (Fig 1.6) is unsuitable for application as a cathode in secondary lithium batteries because it is difficult to extract lithium from the 750°C product. A recent report by Ohzuku et al[123] has, however, shown that it is possible to synthesise an electrochemically active compound with a structure closely resembling that of orthorhombic $LiMnO_2$ by low temperature (400°C) ion exchange of the H^+ ions in the isostructural compound MnO(OH). This compound has been reported to give 190mAhr/g capacity for the first charge and discharge.

In this chapter the direct synthesis of "discharged electrodes" with nominal $LiMnO_2$ stoichiometry in non-oxidizing conditions is examined. The structure and electrochemical performance of the compounds is described.

6.2. EXPERIMENTAL

Samples of nominal composition $LiMnO_2$ were prepared by various methods using several different precursors. In order to synthesise $LiMnO_2$ at moderate temperatures, a reducing atmosphere or reducing agent is required to prevent the oxidation of manganese from the trivalent to the tetravalent state. Two possibilities were investigated in this study. Firstly, the effect of heating the precursors in a hydrogen (reducing) atmosphere for varying lengths of time at temperatures in the range 200-400°C was investigated. Secondly, the precursors were mixed with acetylene black (as reducing agent) and heated in an argon atmosphere to temperatures in the range 580-620°C.

A $LiMn_2O_4$ spinel precursor was prepared by mixing stoichiometric quantities of Li_2CO_3 and $MnCO_3$ (Saarchem). The mixture was ball-milled in hexane for 24 hours and heated in air at 400°C for 10 hours and at 900 °C for 5 hours.

Method 1

Samples with nominal composition $LiMnO_2$ ($Li_2Mn_2O_4$) were prepared by the reaction of the stoichiometric spinel $LiMn_2O_4$ with $LiOH.H_2O$ (Saarchem) according to the ideal reaction :-

$$LiMn_2O_4 + LiOH.H_2O + 0.5H_2 \rightarrow Li_2Mn_2O_4 + 2H_2O$$

The reaction was carried out under a constant flow of dry hydrogen gas. The apparatus used is described in detail in Section 3.3.2. Sample A was prepared by heating at 300°C for 20 hours, Sample B by heating at 350°C for 3 hours and Sample C at 400°C for 20 hours.

Method 2

A precursor, comprising a mixture of the defect spinel $Li_4Mn_5O_{12}$ and Li_2MnO_3, was prepared by mixing Li_2CO_3 and $MnCO_3$ in a 1:2 molar ratio (i.e Li:Mn 1:1). The mixture was ball-milled in hexane for 24 hours and heated in air at 400°C for 48 hours. The 1:1 Li:Mn ratio was chosen as it was the desired ratio in the $LiMnO_2$ product. The precursor was mixed with 25 mol% acetylene black and reacted in argon at 600°C for 20 hours (Sample D). The ideal reaction is as follows :-

$$Li_4Mn_5O_{12} + Li_2MnO_3 + 1.5\ C \rightarrow 6\ LiMnO_2 + 1.5\ CO_2$$

Method 3

$LiOH.H_2O$ (Saarchem), γ-MnO_2 (CMD -Sedema Faradiser M) and acetylene black were reacted. In this case the ideal reaction is:-

$$LiOH.H_2O + MnO_2 + 0.25C \rightarrow LiMnO_2 + 0.25CO_2 + 1.5H_2O$$

The reaction was carried out in a tube furnace under a constant flow of dry argon. Three different samples were prepared : Sample E at 600°C for 2.5 hours, Sample F at 600°C for 4 hours and Sample G at 620°C for 20 hours.

Standard $Li_2Mn_2O_4$ was prepared by the reaction of $LiMn_2O_4$ with a three times excess of LiI (Aldrich) under reflux in acetonitrile in air at ~82°C (the boiling temperature of acetonitrile) for 3-4 hours[98]. The product was washed with acetonitrile to remove any excess LiI and dried in a drying oven at 80°C. The product of the reaction was stored in a desiccator to prevent decomposition by reaction with moist air.

Lithium was extracted from $LiMnO_2$ samples electrochemically using 2-electrode prismatic cells with a 1M solution of $LiClO_4$ in propylene carbonate as electrolyte. The cells were charged at a current density of 0.1mA/cm^2 for the required length of time and then allowed to equilibrate until a stable voltage was reached. The cathode materials were mixed with either 20% by mass of a 1:1 mixture of teflon and acetylene black or, alternatively, with 13% acetylene black and 3% EPDM binder and cycled versus lithium anodes in flooded electrolyte glass cells using a 1 M solution of $LiClO_4$ in propylene carbonate as electrolyte. Discharged products were examined after cycling in electrochemical cells after the 10th discharge to 2.0V.

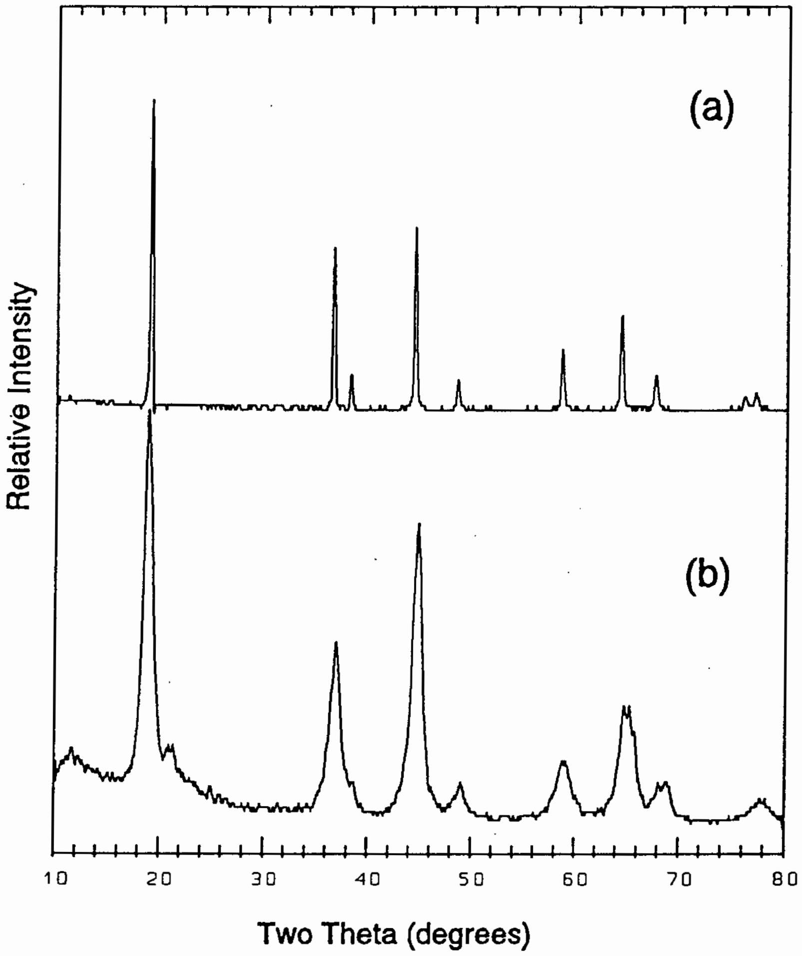

Figure 6.1 : X-ray diffraction patterns of a) $LiMn_2O_4$ and b) a mixture of Li_2MnO_3 and $Li_4Mn_5O_{12}$ precursors.

6.3 RESULTS

6.3.1 "$LiMnO_2$" from Spinel Precursors

Reaction of $LiMn_2O_4$ (a=8.237(1)Å, Fig 6.1a) with $LiOH.H_2O$ at 300-350°C in a hydrogen atmosphere results in compounds with major peaks which can be indexed to a tetragonal lattice and a minor rocksalt by-product (Samples A and B, Figs 6.2a and b). Peaks of the fully reduced manganese oxide rocksalt phase, MnO, are indicated with asterisks. Although it is unlikely that the tetragonal products are stoichiometric $Li_2Mn_2O_4$, they will be referred to as such in the discussion which follows for the sake of simplicity. The powder X-ray diffraction patterns compare well with that of standard $Li_2Mn_2O_4$ prepared by lithiation of $LiMn_2O_4$ with LiI (Fig 6.2d). The refined lattice parameters of the $Li_2Mn_2O_4$ products, indexed to a tetragonal unit cell in the space group $F4_1/ddm$ to indicate the splitting of the cubic spinel reflections, are given in Table 6.1. The $Li_2Mn_2O_4$ products formed by reaction of LiOH and $LiMn_2O_4$ (Samples A and B) are a light yellow-brown colour compared to the black-brown colour of the product of reaction of $LiMn_2O_4$ with LiI and their average particle size is $<1\mu m$, significantly smaller than that of the spinel precursor (average particle size $8\mu m$).

Reaction of $LiMn_2O_4$ and $LiOH.H_2O$ at 400°C for 20 hours results in a product with major peaks of a rocksalt phase (Sample C, Fig 6.2c). The refined lattice parameter of the rocksalt phase is a=4.440(2)Å which compares well with the value for MnO, a=4.445(1)Å. The rocksalt phase was present in minor proportions in all the products obtained by reduction in hydrogen indicating that the reduction potential at 300-400°C favours the formation of Mn^{2+}.

Reduction of the $Li_4Mn_5O_{12}$ + Li_2MnO_3 precursor (Fig 6.1b) with acetylene black at 600°C in argon results in a compound with major peaks of a tetragonal $Li_2Mn_2O_4$ phase (Sample D, Fig 6.3a); the small peaks, at ~15° and ~37° 2θ can be indexed to the (001) and (101) reflections of the orthorhombic $LiMnO_2$ phase (Pmmn symmetry). No MnO peaks are evident, consistent with the lower reduction potential of the carbon reducing agent compared to hydrogen gas. The lattice parameters of the tetragonal phase are given in Table 6.1(a).

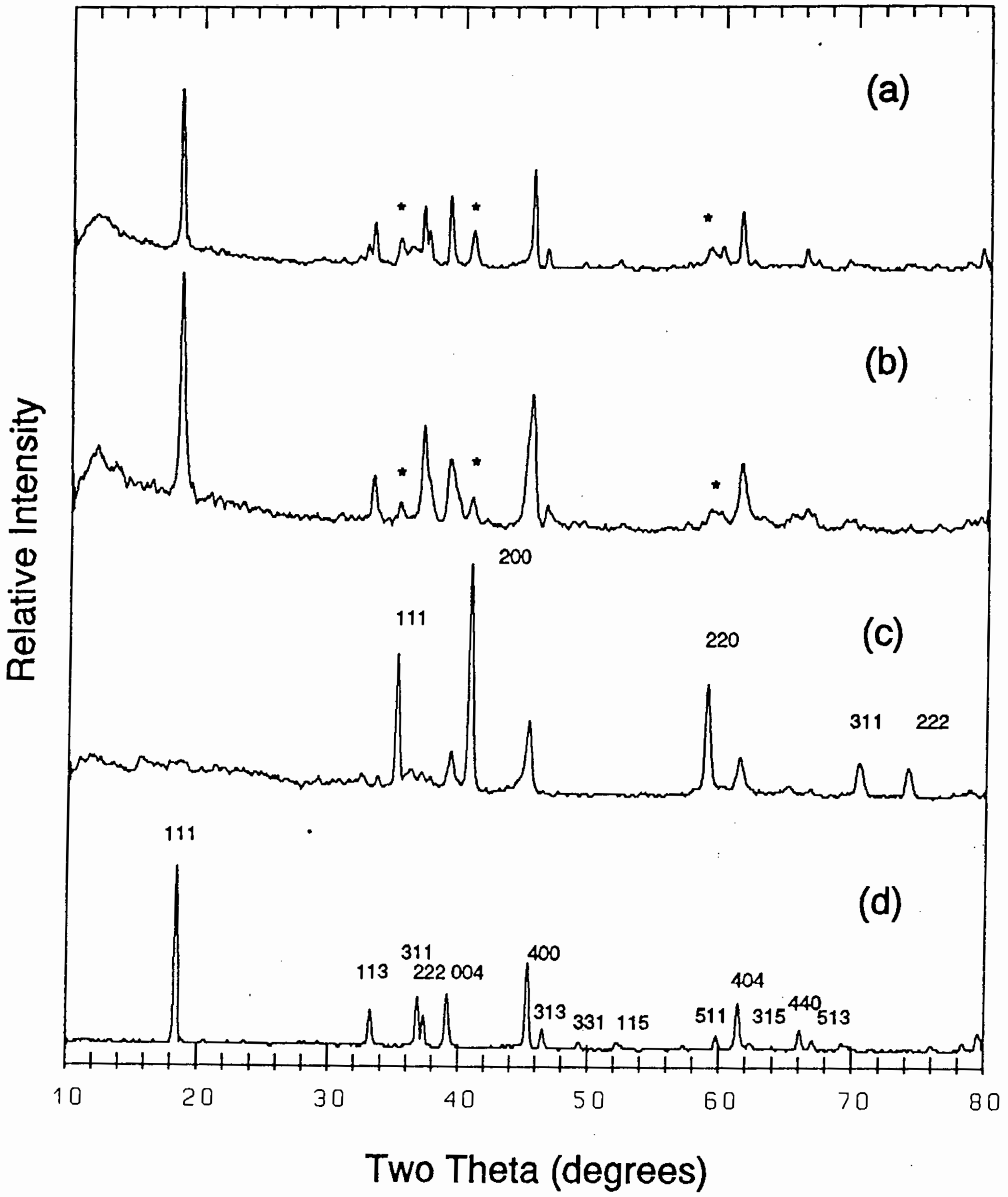

Figure 6.2: Products of reaction of LiOH and $LiMn_2O_4$ in H_2 a) 300°C, 20hrs(Sample A), b) 350°C, 3 hrs (Sample B), c) 400°C, 20 hrs (Sample C) and d) Standard $Li_2Mn_2O_4$ sample. Asterisks indicate peaks of a MnO rocksalt phase.

Table 6.1(a)
Refined Lattice Parameters of $Li_2Mn_2O_4$ Tetragonal Products

Sample	a (Å)	c (Å)	c/a
Sample A	8.004(2)	9.259(4)	1.157(1)
Sample B	8.01(1)	9.23(3)	1.152(4)
Sample D	8.06(2)	9.19(3)	1.140(4)
Std $Li_2Mn_2O_4$	8.006(2)	9.274(4)	1.158(1)

Table 6.1(b)
Refined Lattice Parameters of "$LiMnO_2$" Orthorhombic Products

Sample	a(Å)	b(Å)	c(Å)
Sample E	4.585(4)	2.797(5)	5.736(13)
Sample F	4.586(2)	2.803(2)	5.753(2)
Sample G	4.570(2)	2.800(1)	5.740(4)
Std $LiMnO_2$[122]	4.57(6)	2.80(4)	5.75(8)

6.3.2 "$LiMnO_2$" from γ-MnO_2 Precursors

Reaction of $LiOH.H_2O$, γ-MnO_2 (CMD) and acetylene black at temperatures in the 600°C range for various lengths of time (Samples E and F, Fig 6.3b-c) results in two phase products with peaks which can be indexed to both the tetragonal $Li_2Mn_2O_4$ phase and the orthorhombic $LiMnO_2$ phase. The changes in the relative intensities of the peaks in the products of the various reactions are attributed to slight variations in the stoichiometry of the compounds, for example, the oxygen content, and the distribution of the manganese and lithium ions within the close-packed oxygen lattice. In Sample E, Fig 6.3(b), for example, the intensity of the $LiMnO_2$ peak at 25° (101 in Pmmn) is reduced as is that of the peak at 18° in $Li_2Mn_2O_4$. With increased temperatures and reaction times the orthorhombic $LiMnO_2$ component increases at the expense of the tetragonal $Li_2Mn_2O_4$ phase. Sample G (Fig 6.3 d) is single-phase orthorhombic $LiMnO_2$ and has no characteristic spinel peaks. The refined lattice parameters of the "$LiMnO_2$"

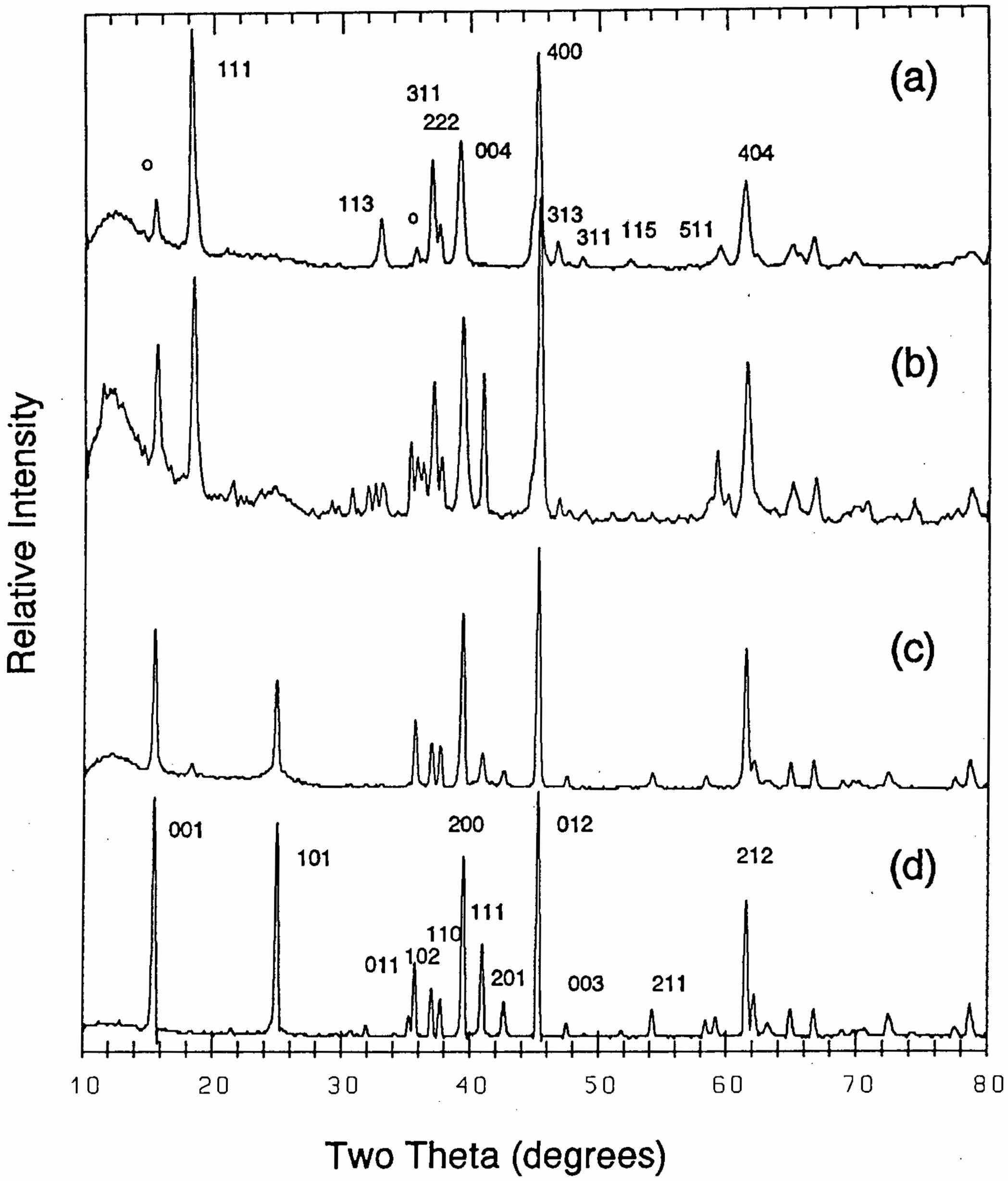

Figure 6.3: X-ray diffraction patterns of a) Sample D, and products of reaction of CMD, C and LiOH at b) 600°C for 2.5 hrs (Sample E), c) 600°C for 4hrs (Sample F) and, d) 620°C for 20 hrs (Sample G). o indicates peaks of the orthorhombic phase.

products, indexed to an orthorhombic unit cell (Pmmn symmetry) are given in Table 6.1(b).

6.4 ELECTROCHEMICAL DATA

6.4.1 Galvanostatic cycling of "$LiMnO_2$" products from spinel precursors

Figs 6.4 (a and b) show the galvanostatic cycling curves of a Li/$LiMn_2O_4$ cell. The cathode is a standard spinel which is electrochemically discharged on the first cycle to form $Li_2Mn_2O_4$. Figs 6.5 (a and b) show the galvanostatic charge and discharge curves of a Li/"$LiMnO_2$" (Sample A) cell, where the cathode consisted predominantly of a tetragonal $Li_2Mn_2O_4$ phase, recorded between 4.2 and 2.5 V. The first charge cycle of the cell gives a capacity of ~ 135 mAhr/g or 40% of the theoretical capacity. The voltage on charge rises steadily from ~3.05V to 4.2V without the clearly defined steps which are evident in subsequent cycles. The discharge voltage profile (Fig 6.5b) after the first charge bears a strong resemblance to that of the $Li_2Mn_2O_4$ lithiated spinel (Fig 6.4b), with a plateau at ~2.8V and two plateaus at ~4V separated by a ~1V step, but the observed capacity is only about 50% of that found for a $Li_2Mn_2O_4$ electrode. The excellent reversibility shown by the cathode contrasts sharply with that of the standard $Li_2Mn_2O_4$ which loses capacity very rapidly when cycled between 2 and 4.45V. The loss of capacity in $Li_{1+x}Mn_2O_4$ cathodes for $x>0$ has been attributed to the large volume changes which accompany the tetragonal distortion in $Li_{1+x}Mn_2O_4$ for $x>1$[42,114].

Figs 6.6 (a and b) show the 1st, 5th and 10th charge and discharge curves of a Li/"$LiMnO_2$" (sample B) cell cycled between 2 and 4.45V. The first charge cycle gives a capacity of ~230 mAhr/g or 76% of the theoretical capacity of $Li_2Mn_2O_4$. The discharge curves show a capacity which drops gradually with cycling with capacity being lost more rapidly on the 3V plateau as is the case for $Li_2Mn_2O_4$ (Fig 6.4b). It should be noted that the capacity above 3.5V (~45 mAhr/g) is significantly smaller than that of a stoichiometric spinel cathode.

Figs 6.7 (a and b) show the charge and discharge curves of a Li/"$LiMnO_2$" (Sample D) cell, where the cathode consists predominantly of a tetragonal phase with minor peaks of orthorhombic $LiMnO_2$. The shape of the initial charge curve is similar to that of Fig

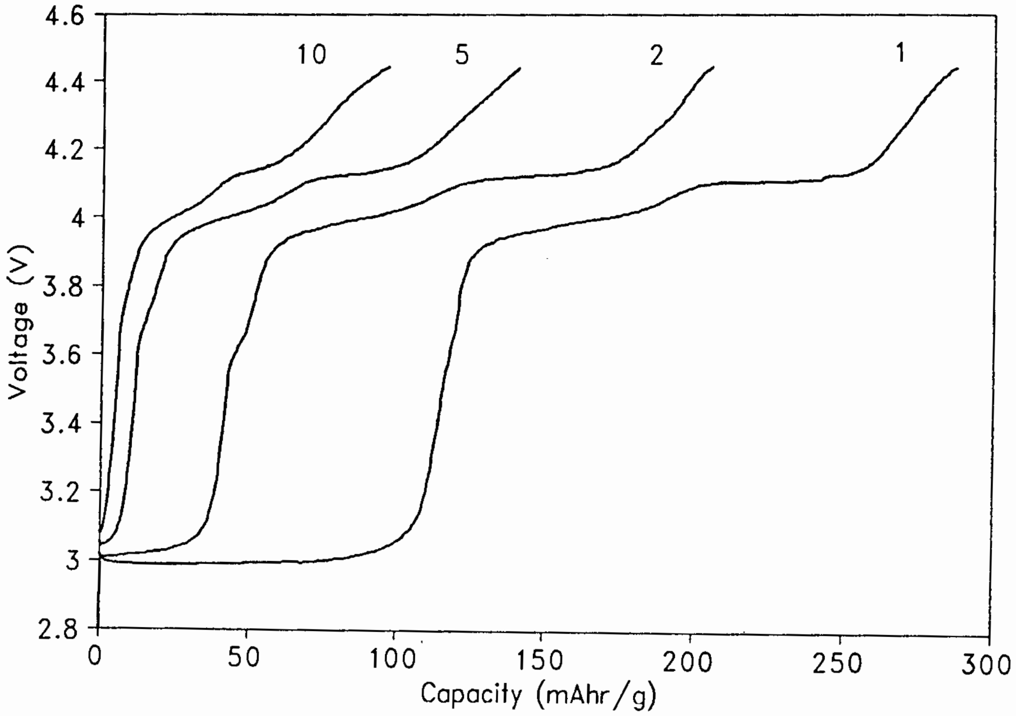

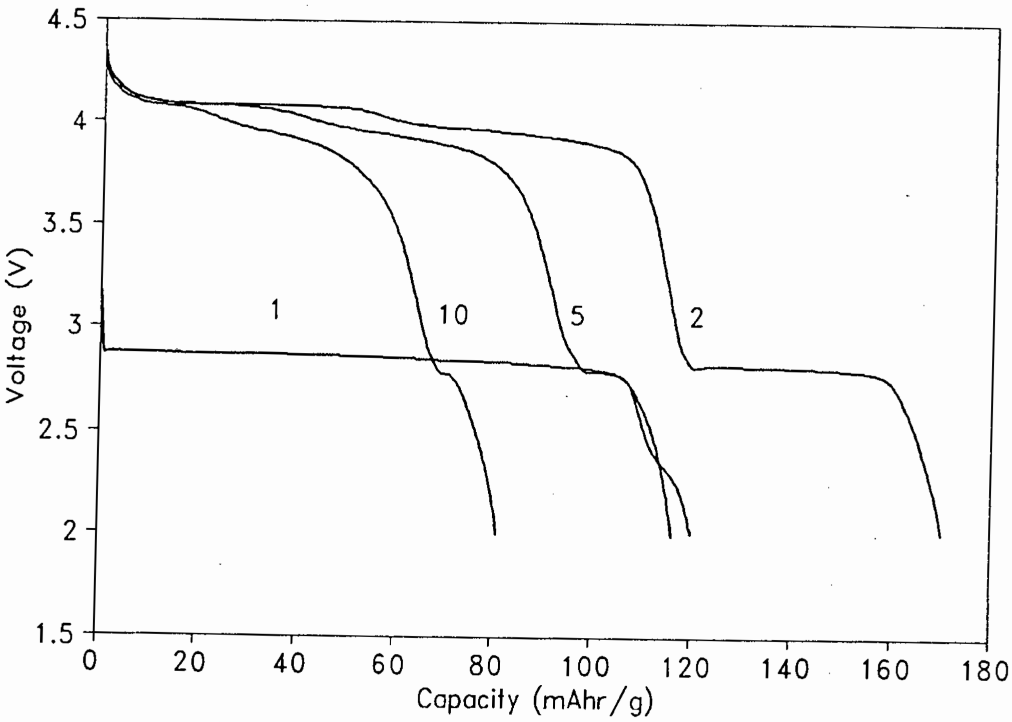

Figure 6.4 : Galvanostatic cycling curves of a Li/standard $LiMn_2O_4$ cell a) charge 0.1 mA/cm^2, b) discharge 0.1 mA/cm^2.

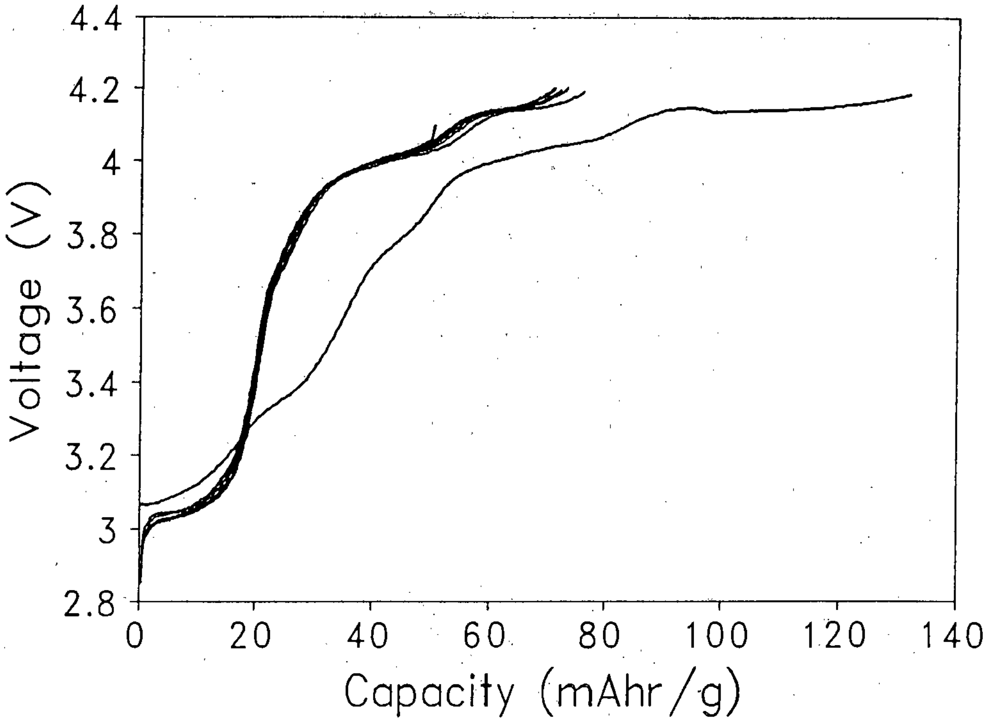

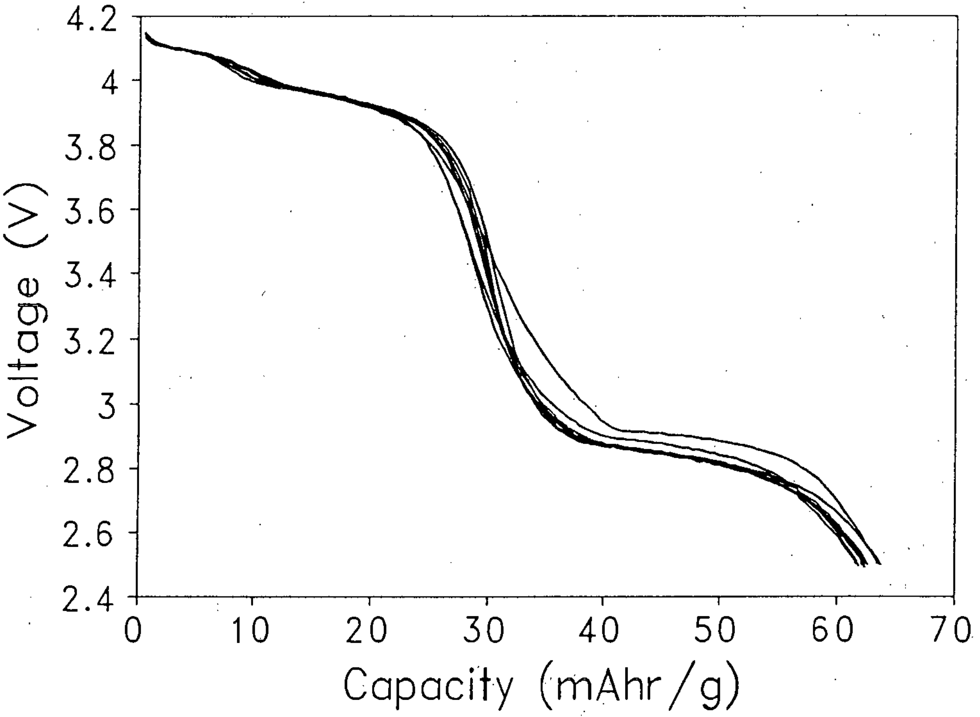

Figure 6.5 : **Galvanostatic cycling curves (cycles 1-10) of a Li/"$LiMnO_2$" cell (Sample A) a) charge cycles 0.1 mA/cm^2 b) discharge cycles 0.2 mA/cm^2.**

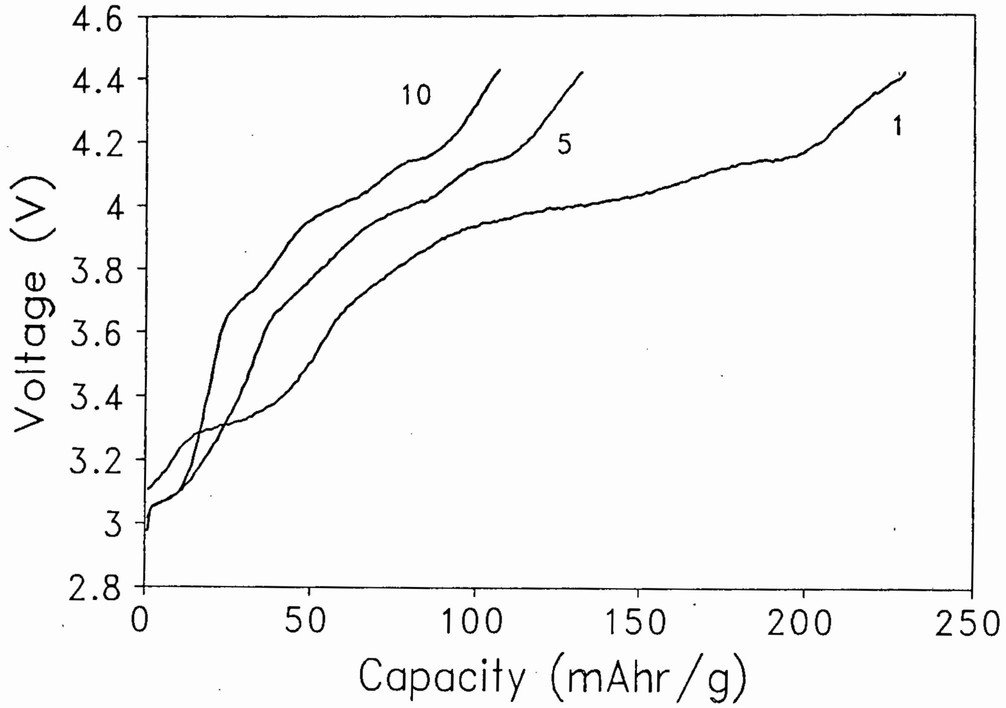

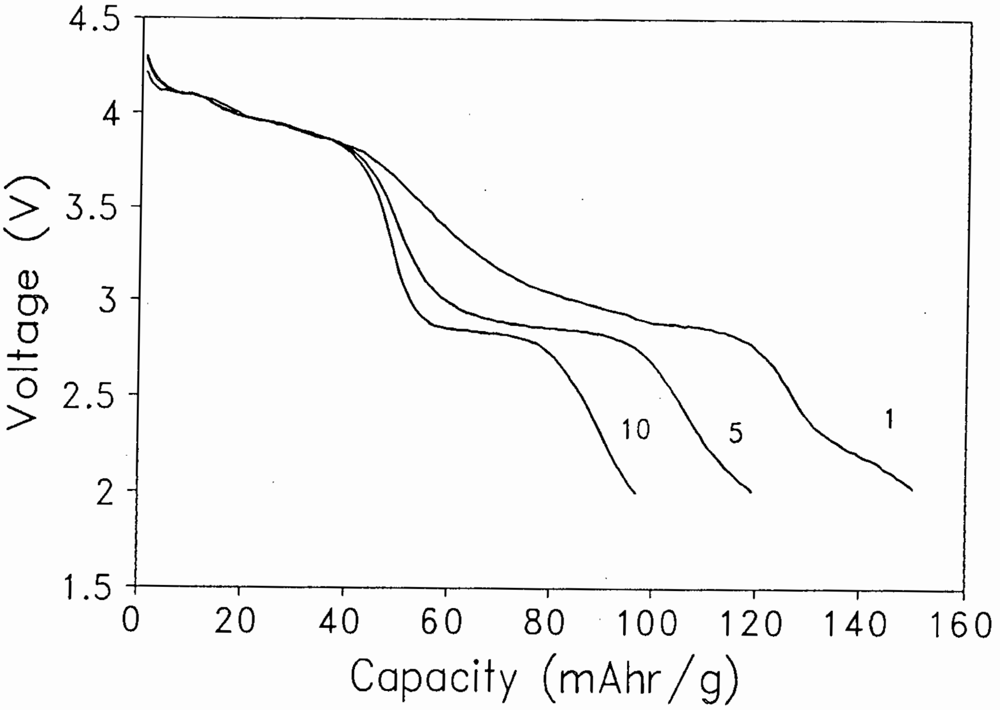

Figure 6.6 : **Galvanostatic cycling curves of a Li/"$LiMnO_2$" (Sample B) cell a) charge 0.1 mA/cm^2, b) discharge 0.1 mA/cm^2.**

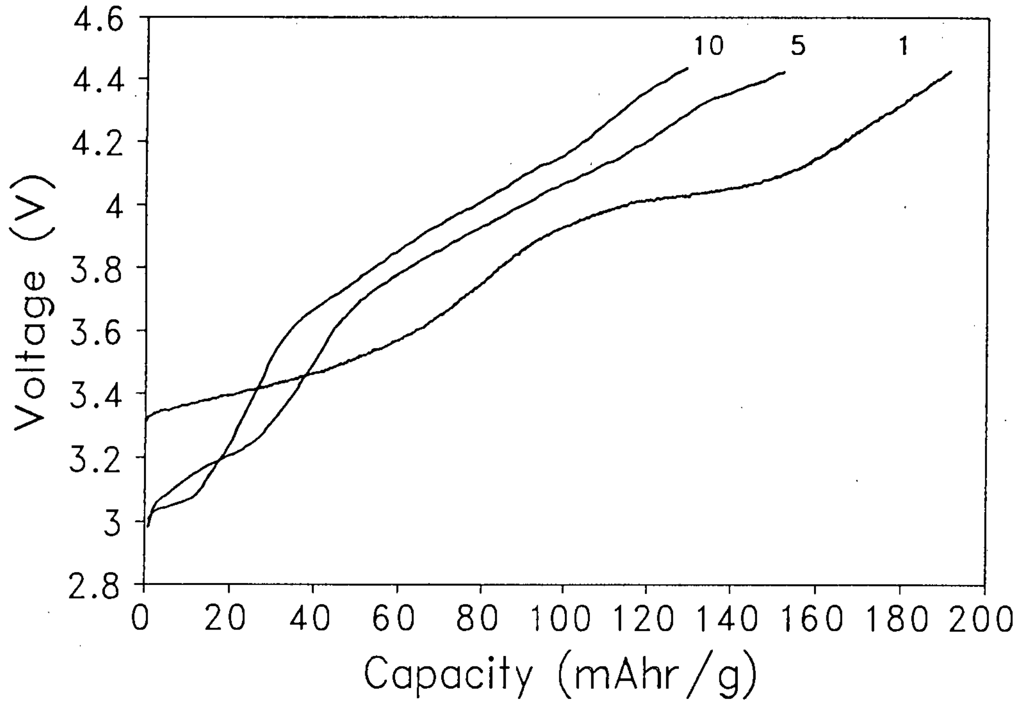

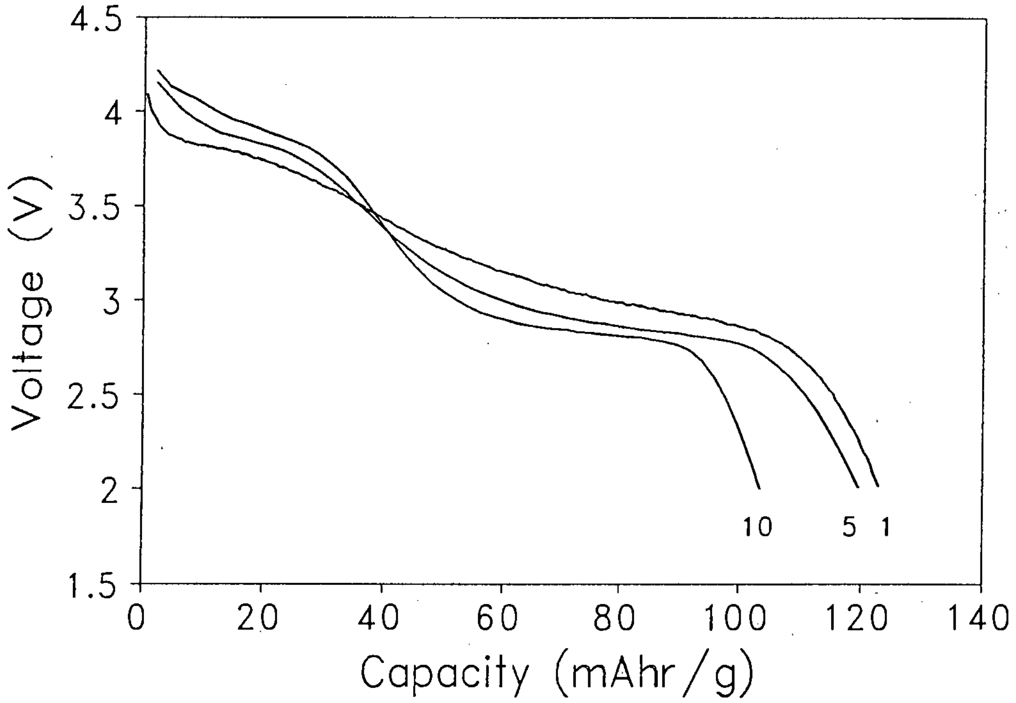

Figure 6.7 : Galvanostatic cycling curves of a Li/"$LiMnO_2$" cell (Sample D) a) charge curves 0.05 mA/cm^2, b) discharge curves 0.1 mA/cm^2.

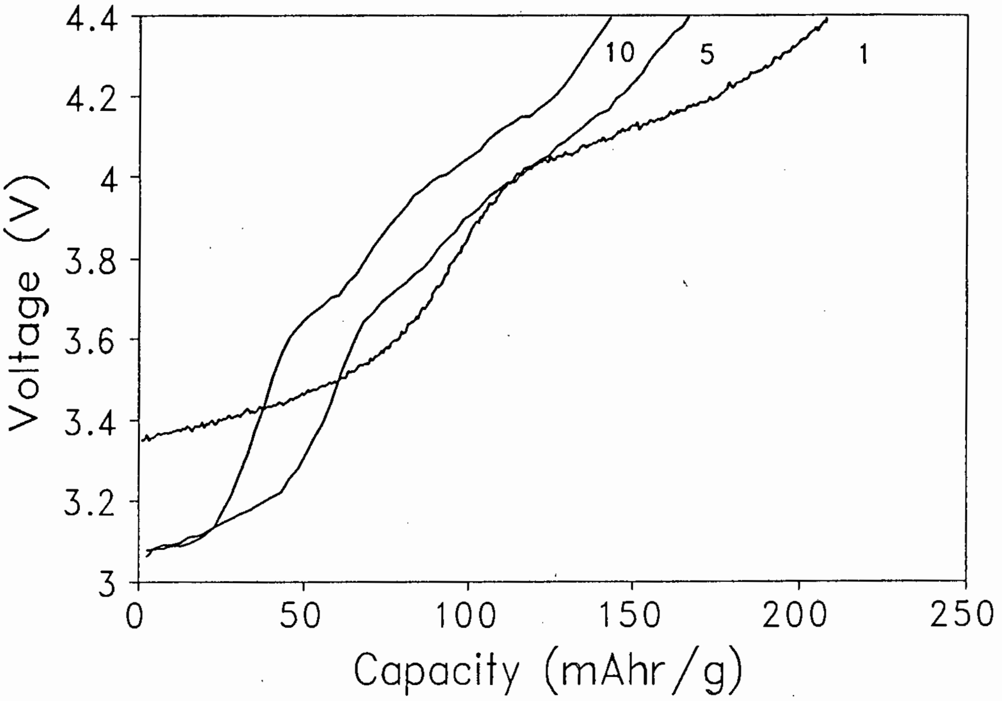

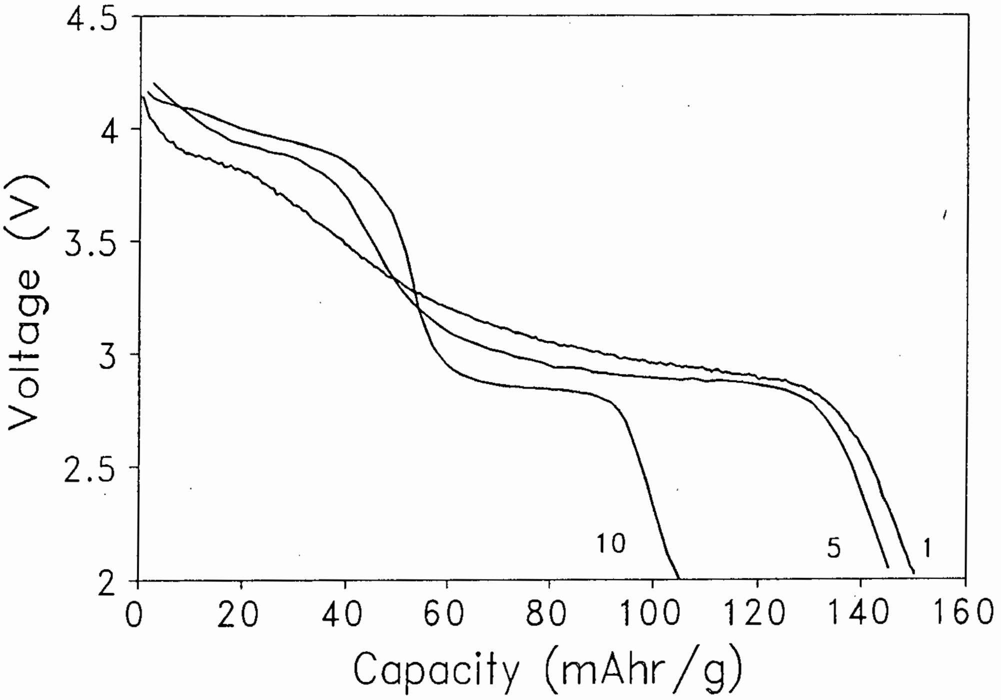

Figure 6.8 : **Galvanostatic cycling curves of a Li/"$LiMnO_2$" cell (Sample E) a) charge curves 0.1 mA/cm^2 and b) discharge curves 0.1 mA/cm^2.**

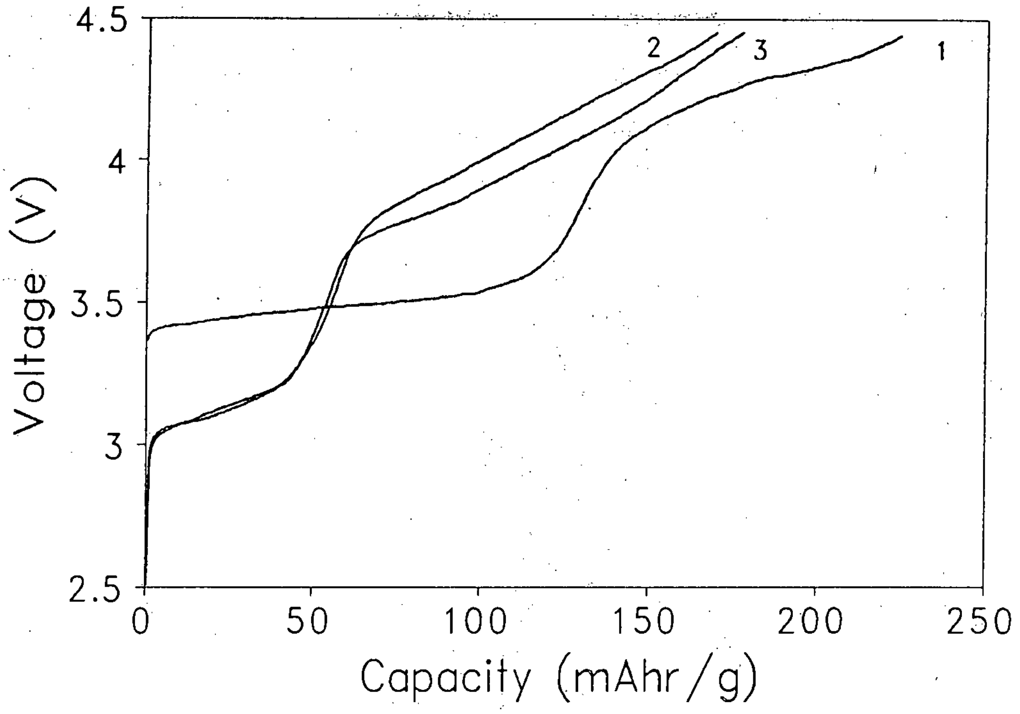

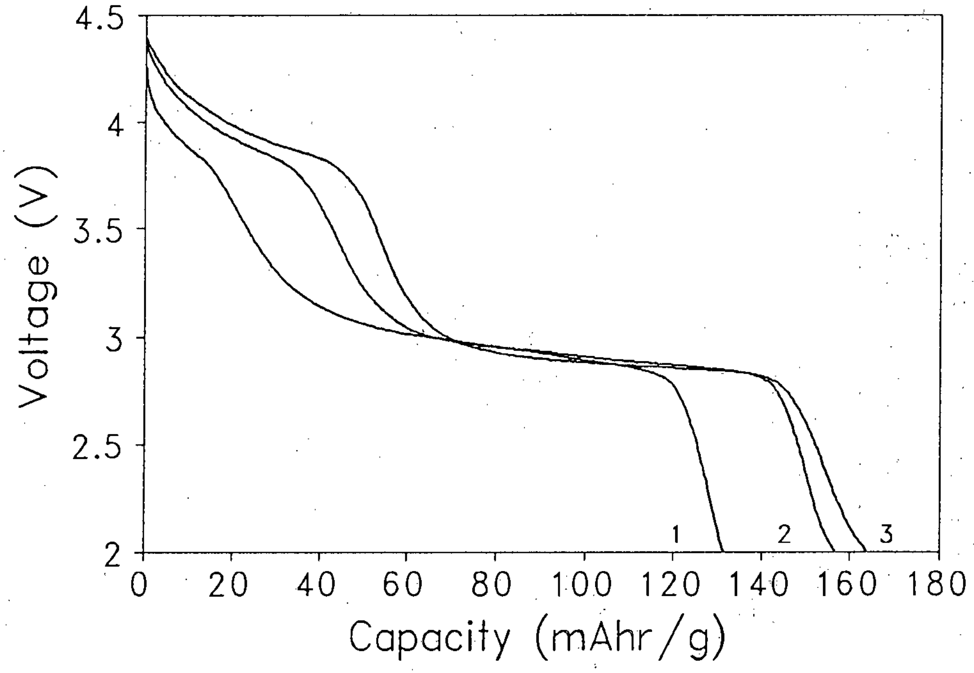

Figure 6.9 : **Galvanostatic cycling curves of a Li/"LiMnO$_2$" cell (Sample F) a) charge curves 0.1mA/cm^2 and b) discharge curves 0.1 mA/cm^2.**

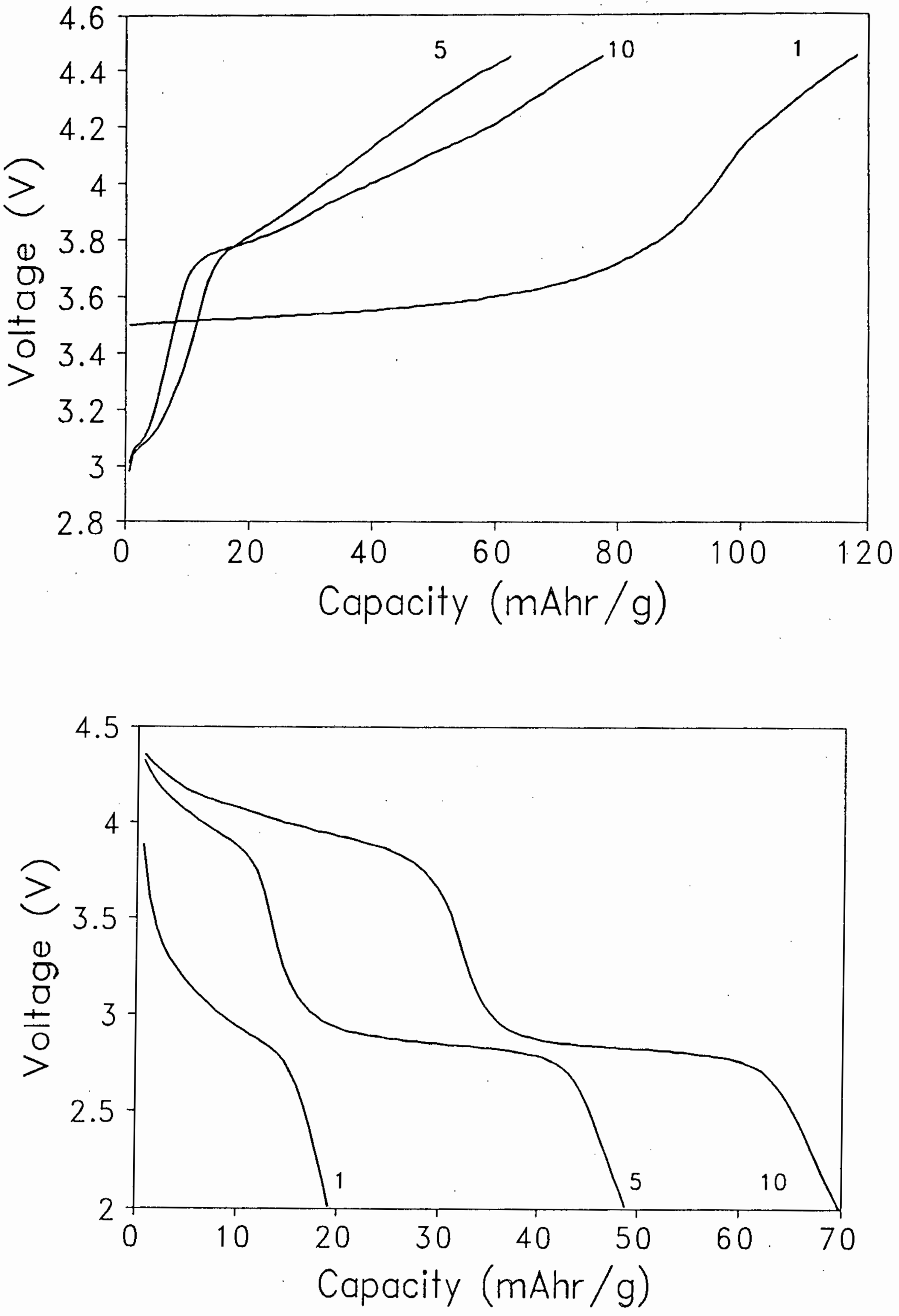

Figure 6.10: **Galvanostatic cycling curves of a Li/"$LiMnO_2$" cell (Sample G) a) charge curves 0.1 mA/cm^2 and b) discharge curves 0.1 mA/cm^2.**

6.6 and significantly different from that of subsequent cycles. The initial charge capacity of ~190 mAhr/g corresponds to $\Delta x \approx 1.3$ in $Li_xMn_2O_4$ to give an approximate composition of $Li_{0.7}Mn_2O_4$ for the fully charged cathode. The initial discharge curve gives a capacity of ~125 mAhr/g corresponding to $\Delta x \approx 0.8$. The shape of the discharge curve changes gradually with cycling showing increasing evolution of the plateau at 4.0V and the sharp step in the discharge curves typical of a standard $Li_x[Mn_2]O_4$ spinel electrode.

6.4.2 Galvanostatic Cycling of "$LiMnO_2$" products from γ-MnO_2

Samples E to G contain increasing amounts of orthorhombic $LiMnO_2$. Surprisingly, the $LiMnO_2$ content does not appear to limit the activity or reversibility of the "$LiMnO_2$" compounds except in the case of sample G which is essentially stoichiometric $LiMnO_2$ (Figs 6.8-6.10). In all three samples, the shape of the discharge curves changes with prolonged cycling with an increase in the capacity on the plateau at 4.0V and an increasingly pronounced voltage step dividing the discharge curves into two regions. This suggests, by analogy with the cycling curves of $Li/LiMn_2O_4$ (Fig 6.4), that the structure of the "$LiMnO_2$" cathodes becomes increasingly spinel-like as cycling progresses. In particular, the discharge capacities of samples F and G, both of which initially contain a major proportion of the orthorhombic $LiMnO_2$ phase, increase with cycling, indicating that the transformation of the orthorhombic structure to a spinel lattice leads to the increase in electrochemical activity. These data are entirely consistent with the known stability of the spinel structure in the Li-Mn-O system and the excellent electrochemical behaviour of lithium-manganese-oxide spinel cathodes that has been reported previously[49,98].

6.5 DISCUSSION

The results presented in this chapter show that a tetragonal product closely resembling the lithiated spinel $Li_2Mn_2O_4$ can be synthesised by reduction in a hydrogen atmosphere at 300-350°C of a mixture of a spinel, such as $LiMn_2O_4$, with LiOH, or, by reduction with a carbon reducing agent of a mixture of $Li_4Mn_5O_{12}$ and Li_2MnO_3 in argon at 600°C.

Reaction of γ-MnO_2 with LiOH and carbon in argon results in two-phase mixtures which can be described as intergrowth structures of orthorhombic $LiMnO_2$ and tetragonal $Li_2Mn_2O_4$. Previous investigators have reported that annealing tetragonal $Li_2Mn_2O_4$ in argon at temperatures >500°C results in a transformation to the orthorhombic $LiMnO_2$ phase[48,98]. The increase in the amount of orthorhombic phase in samples synthesised at high temperatures for long times is therefore consistent with this finding.

Barboux et al[124] attempted to synthesise tetragonal $Li_2Mn_2O_4$ from manganese and lithium acetate precursors by annealing at 400°C in atmospheres containing low oxygen pressures in argon. The products were always multiphase mixtures of $LiMn_2O_4$ with either MnO or Li_2MnO_3. By contrast, this study demonstrated that the spinel framework in the precursor materials favours the formation of the tetragonal $Li_2Mn_2O_4$ phase.

6.5.1 Evidence for Defect Spinel Character of Tetragonal Products

The lattice parameters and c/a ratio of the tetragonal phase in Sample A (a=8.004(2)Å, c=9.259(4)Å and c/a=1.157(1)) agree well with those of stoichiometric $Li_2Mn_2O_4$ (a=8.006(2), c=9.274(4) and c/a=1.158(1))[42](Table 6.1). The c/a ratios of samples B and D are slightly lower, having values of 1.152(4) and 1.140(4) respectively.

A decrease in the extent of the tetragonal distortion has been observed for the lithiated spinels of the solid solution $Li_2O.yMnO_2$. For example, a $Li_{6.3}Mn_5O_{12}$ product obtained by lithiation of $Li_4Mn_5O_{12}$ was two-phase with a tetragonal component with a=8.036(1)Å, c=8.906(1)Å and c/a=1.108(1), whereas a $Li_{4.4}Mn_4O_9$ product obtained by lithiation of $Li_2Mn_4O_9$ had a tetragonal component with a=8.011(1)Å, c=9.150(1)Å and c/a=1.142(1)[49]. A tetragonal product $Li_{1-y}MnO_2$ has also been formed by chemical lithiation of ß-MnO_2 with n-butyllithium[125]. The product of the reaction has an X-ray pattern similar to that of $Li_2Mn_2O_4$ but with a c/a ratio of 1.145(1).

These data show, therefore, that the tetragonal products obtained in this study are slightly non-stoichiometric. For example, the formation of a minor proportion of MnO, in samples A and B changes the Li:Mn ratio in the tetragonal product from 1:1 and results in a compound which can be described more generally by the formula $LiMn_{1-x}O_{1+y}$ with $x \approx 0.1$ and $y \approx 1$.

Sample D was formed from a defect spinel precursor in which the manganese ions were essentially all tetravalent. Incomplete reduction to Mn^{3+} results in a product which can be described as being slightly oxygen-rich with general formula $LiMnO_{2+y}$ with ($y \approx 0.1$).

The step of approximately 1V in the first charge curve of a $Li/LiMn_2O_4$ cell occurs at $x \approx 1$ in $Li_xMn_2O_4$ (Fig 6.4a). This corresponds to an average manganese oxidation state of approximately 3.5 and coincides with the onset of the Jahn-Teller distortion which lowers the symmetry from cubic to tetragonal. The origin of the ~1V step that is also found in other spinels, for example, LiV_2O_4, has not yet been explained in detail.

Lithium can be inserted into the oxygen-rich spinels of the $Li_2O.yMnO_2$ solid solution up to the rocksalt stoichiometry. In contrast to $LiMn_2O_4$ however, the oxygen-rich spinels e.g $Li_2Mn_4O_9$ (y=4) discharge all their capacity on the 3V plateau despite the fact that the Jahn-Teller distortion only occurs when the average manganese oxidation state reaches ~3.5.[49]

Low capacities were observed above 3.5V for the $Li_2Mn_2O_4$ cathodes prepared by reduction in hydrogen or using carbon in argon (Samples B and D, Figs 6.6 and 6.7 respectively). By analogy with the $Li_2O.yMnO_2$ spinel system, this result confirms that the tetragonal products synthesised for these investigations did not have the ideal $[B_2]X_4$ spinel framework.

The poor electrochemical activity of Sample A (tetragonal $Li_2Mn_2O_4$) may be understood in terms of the reaction of $LiMn_2O_4$ with LiOH in H_2. It is likely that this reaction occurs at the particle surface resulting in the break-down of the particles to give a product with a very small particle size. As the reaction progresses the particle surface is reduced further and is covered with an electrochemically inactive layer of MnO. (MnO has a rocksalt structure with all octahedral sites fully occupied with Mn^{2+} ions). The inactive surface layer on $Li_2Mn_2O_4$ particles therefore limits electrochemical activity and can account for the low observed capacities obtained from Sample A. Sample B was synthesised at a slightly higher temperature and for a much shorter time than sample A, resulting in a product containing a smaller amount of surface MnO and hence showing improved electrochemical activity.

6.5.2. The $LiMnO_2$ to spinel transition

The electrochemical data obtained in this study provide strong evidence that the orthorhombic $LiMnO_2$ lattice is destabilised by lithium extraction and transforms on cycling to a spinel lattice. The phase transition was confirmed by X-ray diffraction of electrochemically delithiated Li_xMnO_2 samples with x=0.7, 0.4 and 0.2 shown in Figs 6.11(b-d) respectively. The lattice constants of $LiMnO_2$ (Sample F, Fig 6.11(a)) are: a=4.586(2)Å, b=2.803(2)Å and c=5.753(2)Å; the a parameter is slightly larger than that reported by Dietrich and Hoppe[122] (a=4.57(6)Å, b=2.80(4)Å and c=5.75(8)Å) for stoichiometric $LiMnO_2$. A reduction in the intensity of the (001) and (101) peaks compared to stoichiometric $LiMnO_2$ and the small peak at ~18° 2θ indicate a deviation from the ideal $LiMnO_2$ structure and the onset of spinel-like domains within the structure. For x=0.7 in Li_xMnO_2 the (001) peak of the orthorhombic lattice at ~ 15° 2θ is still evident in the X-ray diffraction pattern although it is shifted to slightly lower 2θ values. However, for the samples with x=0.4 and x=0.2 this peak is no longer visible and the peak at 18° 2θ corresponding to the (111) spinel reflection increases in intensity. The spinel reflections become more clearly defined as x decreases.

Fig 6.11(e) shows the powder X-ray diffraction pattern of a partially discharged Li_xMnO_2 cathode with $x \approx 0.4$ after 10 cycles. The X-ray diffraction pattern can be indexed to a cubic unit cell (Fd3m) with a=8.260(2)Å. It is surprising that the lattice constant is slightly larger than that of $LiMn_2O_4$ (a=8.242(1)Å). The structure was refined to a spinel-related compound using integrated peak intensities with the Wiseman refinement program. The intensity distribution and crystallographic parameters of the refinement are given in Tables 6.2 and 6.3 respectively.

Assuming that the composition of the starting cathode was $LiMnO_2$, the composition of the cathode after 10 cycles was calculated from the capacities of subsequent charge and discharge cycles to be $Li_{0.4}MnO_2$. Lithium cations were assumed to occupy the 8a tetrahedral sites of the spinel structure and the lithium content was held constant during

Table 6.2 Normalised Observed and Calculated Intensities of $Li_{0.4}Mn_2O_4$

h k l	Observed Intensity	Calculated Intensity
1 1 1	2980	2844
3 1 1	1213	1633
2 2 2	457	392
4 0 0	3192	3306
5 1 1 3 3 3	878	566
4 4 0	1733	1703
4 4 2 5 3 1 6 0 0	688	359
6 2 2 5 3 3	376	409

Table 6.3 Crystallographic Parameters of the Refinement of $Li_{0.4}Mn_2O_4$

a=8.260(2)Å Space Group : Fd3m

ATOM	SITE	POSITION x	y	z	B_{iso}	Occupation
Li1	8a	0.125	0.125	0.125	1.0	0.4
Mn1	16c	0	0	0	0.8	0.13(4)
Mn2	16d	0.5	0.5	0.5	0.8	1.0(1)
O	32e	0.256(7)	0.256(7)	0.256(7)	3.00	1.0(1)

$R_{Bragg}=12.41\%$

the refinement. The manganese cations were refined in both the 16c and 16d octahedral sites. The isotropic B-factors were not refined. The refined stoichiometry was $\{Li_{0.8}\}_{8a}[Mn_2]_{16d}(Mn_{0.13})_{16c}O_4$ with R_{Bragg} = 12.41%. The refinement showed that there was a small amount of manganese in the 16c sites.

A proposed mechanism for the structural transformation of the MnO_2 framework in orthorhombic $LiMnO_2$ to the $[Mn_2]O_4$ spinel framework on lithium extraction from $LiMnO_2$ is given in Fig 6.12. The ideal orthorhombic $LiMnO_2$ structure consists of alternate zig-zag layers of lithium- and manganese-occupied octahedra. The layers lie perpendicular to the {001} direction and not perpendicular to the direction of close-packing as is the case in the $R\bar{3}m$ structure adopted by $LiCoO_2$ and $LiNiO_2$. Two parallel slices of the orthorhombic Li_xMnO_2 structure, offset by the width of one octahedron, are illustrated in Figs 6.12(a and b) with the corresponding slices of the $Li_xMn_2O_4$ spinel in Figs 6.12(c and d) respectively. Shaded octahedra represent manganese-occupied sites while clear octahedra represent lithium-occupied or vacant octahedra.

It is evident that certain discrete planes consisting of alternating strings of fully-occupied Mn and Li (or vacant) octahedra in the parent orthorhombic $LiMnO_2$ structure and in the spinel product are unaffected by the transformation; these planes are highlighted in bold outline in Figs 6.12(a-d); the transformation takes place in the oxygen framework between these planes. Lithium extraction from the zig-zag channels causes a displacement of 50% of the manganese ions into neighbouring octahedra left vacant by the extracted lithium ions as indicated by the arrows in Fig 6.12(a and b). In the ideal transformation process, the displacement of one manganese ion from its octahedral position through a face-shared tetrahedron (curved arrow) into a vacant octahedral site causes the cooperative displacement of one other manganese ion (straight arrow). The direction of the manganese-ion pair displacements in Fig 6.12a is opposite to that in the next slice (Fig 6.12b). These displacements generate the 3:1 spinel ratio of manganese ions in alternate layers between the close-packed oxygen planes (Fig 6.12(c and d)). In practice, the electrochemical and X-ray diffraction data show that a few cycles are necessary to accomplish the transformation and that metastable and disordered spinel-type structures are produced as intermediate phases.

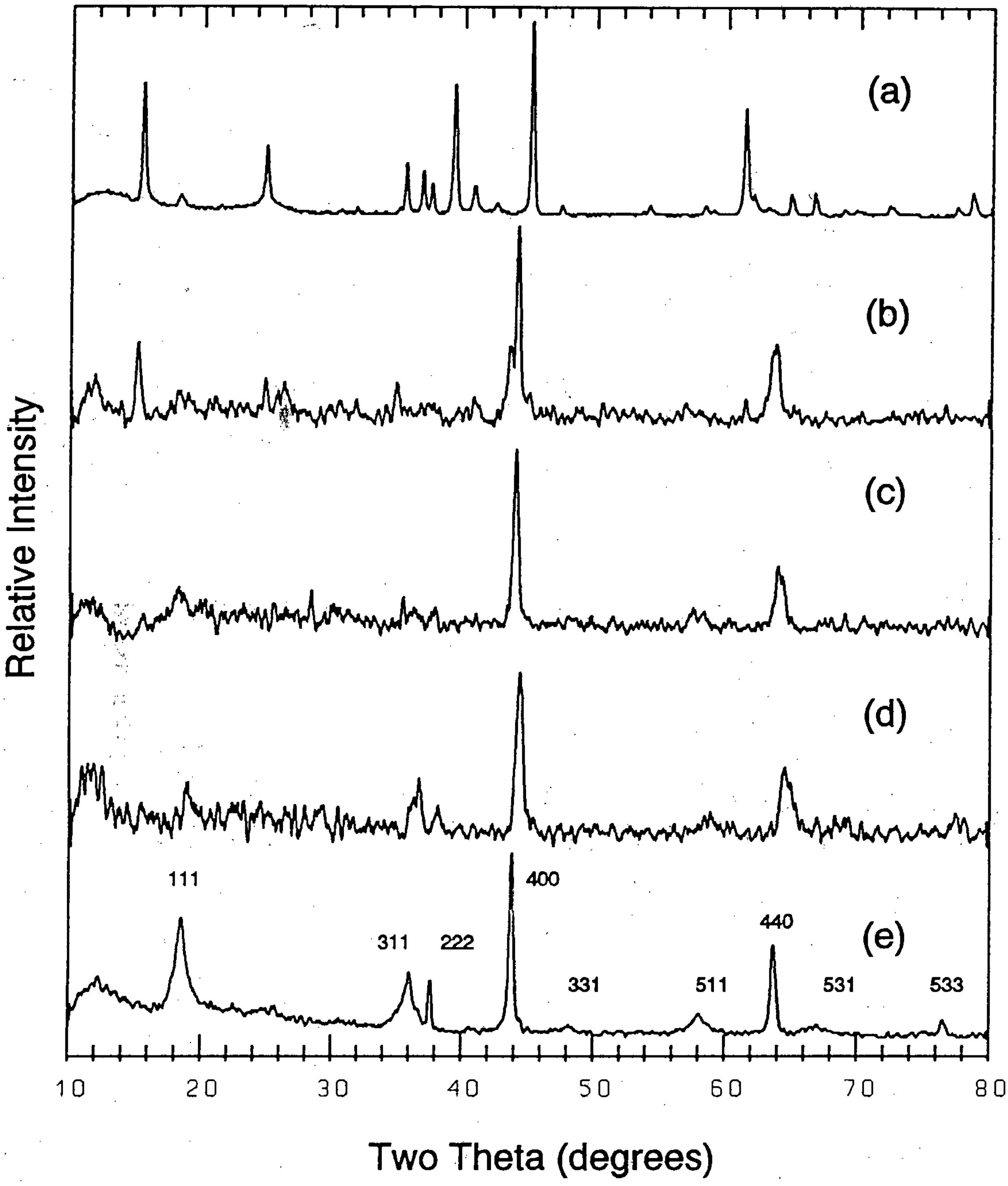

Figure 6.11: Powder X-ray diffraction patterns of Li_xMnO_2(Sample F) a) x=1.0, b) x=0.7, c) x=0.4, d) x=0.2 and e) discharged after 10 cycles.

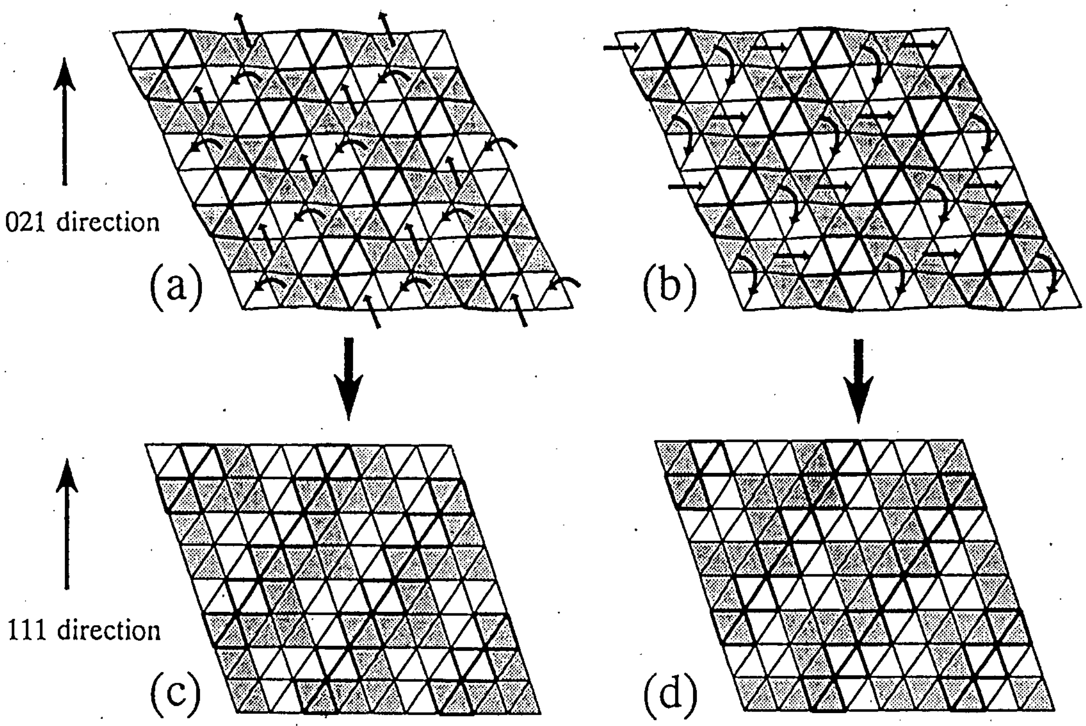

Figure 6.12 : Schematic diagram of the transformation from the orthorhombic to the spinel structure for Li_xMnO_2.

These results demonstrate that the $[Mn_2]O_4$ spinel framework, which may also be regarded as a defect rocksalt phase, is extremely stable at moderate temperatures. On continual cycling of Li/Li_xMnO_2 cells it is the preferred manganese-oxide framework compared with the cation arrangements of other possible defect rocksalt structures. These data are therefore totally consistent with other reports that the $[Mn_2]O_4$ spinel framework is generated by lithium insertion into manganese oxides e.g. ß-MnO_2[125] and ramsdellite-MnO_2[126] at moderate temperatures e.g. 50 to 300°C.

6.6 CONCLUSIONS

This study has demonstrated firstly, that tetragonal products with approximate $Li_2Mn_2O_4$ stoichiometry can be synthesised directly from simple precursors in reducing conditions. These compounds contain additional lithium compared to $LiMn_2O_4$ and this can be used to compensate for the capacity losses on the first cycle of the carbon anodes used in rocking-chair cells. However, the non-stoichiometric nature of the tetragonal products results in a decrease in the electrode capacity above 3.5V compared to that of $LiMn_2O_4$ electrodes. Further work is required to optimize the synthesis conditions to generate $Li_{1+x}Mn_2O_4$ $(0<x<1)$ tetragonal products with the ideal stoichiometry and capacities above 3.5V which compare favourably with that of standard $Li_xMn_2O_4$ electrodes $(0<x<1)$.

Secondly, the predominantly orthorhombic "$LiMnO_2$" compounds containing some spinel domains have been shown to be electrochemically active. Although these compounds discharge most of their capacity at ~3V versus lithium initially, they transform rapidly on cycling to the spinel structure resulting in a slight increase in capacity above 3.5V. However, once the spinel framework is established, capacity is lost rapidly on the 3V plateau, as is the case of stoichiometric $LiMn_2O_4$ electrodes. Therefore, although these compounds can be synthesised, relatively easily, in a discharged state, their rapid transformation to a spinel structure results in similar cycling properties compared to stoichiometric $LiMn_2O_4$ electrodes when cycled over the full range of lithium composition $(0 \leq x \leq 2)$.

CHAPTER 7

GENERAL CONCLUSIONS AND SUGGESTIONS FOR FURTHER WORK

This work has shown that the structure and electrochemical properties of the well-known layered compound $LiCoO_2$ synthesised at 900°C can be significantly altered by lowering the synthesis temperature to 400°C. The novel compound, LT-$LiCoO_2$ was found to have a rocksalt structure with cobalt and lithium cations distributed in an arrangement that is intermediate between that of an ideal layered and ideal lithiated spinel lattice. This structural change resulted in significantly different electrochemical properties for LT-$LiCoO_2$ compared to HT-$LiCoO_2$. Of particular significance for the potential application of this compound as a cathode in reversible lithium batteries is the fact that its average charge and discharge voltages were found to be lower than those of HT-$LiCoO_2$ over the same compositional range. LT-$LiCoO_2$ therefore shows promise as a replacement for HT-$LiCoO_2$ as a cathode for lithium batteries as it is potentially more stable in the organic electrolytes typically used in these cells. Cycling data obtained for LT-$LiCoO_2$ cathodes to date do not, however, compare well with those of HT-$LiCoO_2$ cathodes under the same electrochemical conditions. In particular LT-$LiCoO_2$ electrodes gave large polarisation voltages and did not cycle well.

Chemical delithiation of LT-$LiCoO_2$ by acid-leaching resulted in a compound, LT-$Li_{0.4}CoO_2$ which has a defect spinel structure, as shown by refinement of powder neutron diffraction data. This was the first indication that a cobalt spinel, isostructural with the LiM_2O_4 spinels (M = Mn, V and Ni), could be synthesised. This compound discharged most of its capacity on a constant voltage plateau at 3.4V vs lithium and showed slightly improved cycling stability and reduced polarisation compared to LT-$LiCoO_2$.

Further work is needed to develop a stable $LiCo_2O_4$ spinel which can reversibly intercalate lithium. However, for rocking-chair cells using carbon anodes, cathodes are required which can be prepared in a fully discharged state. Ideally, an alternative synthesis route is required which will generate a lithiated $Li_2[Co_2]O_4$ spinel directly. The ideal spinel lattice of $Li_2[Co_2]O_4$ is expected to be significantly more stable than LT-$LiCoO_2$ on lithium extraction and re-insertion. Lowering the synthesis temperature favoured the formation of the spinel structure over the layered structure of $LiCoO_2$. It is therefore believed that alternative precursors, which decompose to yield $LiCoO_2$ products at temperatures below 400°C, would offer possible routes for synthesising an ideal lithiated spinel product.

Nickel doping of LT-$LiCoO_2$ has been investigated and shown to result in essentially single-phase LT-$LiCo_{1-y}Ni_yO_2$ compounds for $x=0.1$ and 0.2 with structures similar to the structure of LT-$LiCoO_2$. For higher nickel contents a second phase, $Li_yNi_{1-y}O$, was also present. Nickel doping of the LT-$LiCoO_2$ compound resulted in stabilisation of the lattice and an improvement in the capacity and reversibility of LT-$LiCo_{1-y}Ni_yO_2$ cathodes. In particular, the delithiated LT-$Li_{0.4}Co_{0.9}Ni_{0.1}O_2$ compound, which, by analogy with LT-$Li_{0.4}CoO_2$, was assumed to have a spinel lattice showed improved reversibility and capacity retention compared with LT-$Li_{0.4}CoO_2$. A structural refinement of the neutron diffraction data of a LT-$Li_{0.4}Co_{0.9}Ni_{0.1}O_2$ sample is required to confirm the spinel arrangement of cations in this structure. The effects of alternative dopants to stabilise LT-$LiCoO_2$ electrodes, for example, Mn, V and Ti should also be investigated.

It was not possible to synthesise the nickel analogue of LT-$LiCoO_2$; samples of $LiNiO_2$ heat treated at 400°C showed only the presence of the rocksalt phase NiO.

In this work it has also been shown that, under appropriate reducing conditions, a compound closely resembling the lithiated spinel $Li_2[Mn_2]O_4$ could be synthesised directly from simple precursors. Slight non-stoichiometry in the product, however, reduced the available charge/discharge capacity of these electrodes in the region above 3.5V, compared to that which can be obtained from standard $Li_2[Mn_2]O_4$ cathodes. These compounds are potentially useful as cathodes for rocking-chair cells but further work is required to optimise the synthesis conditions to increase the capacity available above 3.5V.

Synthesis of "$LiMnO_2$" electrodes from either a mixture of $Li_4Mn_5O_{12}$ and $LiMn_2O_4$ or from γ-MnO_2 and LiOH, using carbon as the reducing agent at 600°C resulted in products with a structure that contained domains of orthorhombic $LiMnO_2$ and tetragonal $Li_2[Mn_2]O_4$. The proportion of the orthorhombic phase increased with increasing temperature and reaction time. "$LiMnO_2$" compounds containing predominantly orthorhombic $LiMnO_2$ were found to be electrochemically active and transformed to a spinel structure on lithium extraction. These data have emphasized the stability if the $[Mn_2]O_4$ spinel framework as a host structure for lithium insertion/extraction reactions.

REFERENCES

1. E Peled, *J. Electrochem. Soc.*, **126**, 2047 (1979).

2. D Aurbach, M L Daroux, P W Faguy and E B Yeager, *J. Electrochem. Soc.*, **134**, 1611 (1987).

3. S Tobishima, M Arakawa and J Yamaki, *Electrochim. Acta.*, **35**, 383 (1990).

4. Y Matsuda, *J. Power Sources*, **20**, 19 (1987).

5. D Wainwright and R Shimizu, *J. Electrochem. Soc.*, in press.(1993)

6. D P Wilkinson, H Blom, K Brandt and D Wainwright, *J. Power Sources*, **36**, 517 (1991).

7. F C Laman and K Brandt, *J. Power Sources*, **24**, 195 (1988).

8. "Cellular Phone Recall May Cause Setback for Moli", *Toronto Globe and Mail*, August 15, 1989 (Toronto, Canada).

9. *Adv. Batt. Technol.*, **25**, 4 (1989).

10. M Armand in *Materials for Advanced Batteries*, D W Murphy, J Broodhead and B C H Steele (ed.), Plenum Press, New York, 145 (1980).

11. T Nagaura and K Tozawa, *Prog. Batteries Sol. Cells*, **9**, 209 (1990).

12. C G Granqvist, *Solid State Ionics*, **53-56**, 479 (1992).

13. S Passerini, B Scrosati and A Gorenstein, *J. Electrochem. Soc.*, **137**, 3297 (1990).

14. M M Thackeray, *Mat. Res. Symp. Proc.*, **135**, 585 (1989).

15. D Guyomard and J M Tarascon, *J. Electrochem. Soc.*, **139**, 937 (1992).

16. M G S R Thomas, P G Bruce and J B Goodenough, *Solid State Ionics*, **17**, 13 (1985).

17. M S Whittingham, *Prog. Solid State Chem.*, **12**, 41 (1978).

18. A J Vaccaro, T Polanisamy, R L Kerr and J T Maloy, *J. Electrochem. Soc.*, **129**, 682 (1982).

19. P G Bruce, A Lisowska-Oleksiak, M Y Saidi and C A Vincent, *Solid State Ionics*, **57**, 353 (1992).

20. B C H Steele in *Fast Ion Transport in Solids*, W van Gool (ed), North Holland, Amsterdam, 103 (1973).

21. L Heyne in *Fast Ion Transport in Solids*, W van Gool (ed), North Holland, Amsterdam, 123 (1973).

22. M B Armand in *Fast Ion Transport in Solids*, W van Gool (ed), North Holland, Amsterdam, 665 (1973).

23. M S Whittingham, *J. Electrochem. Soc.*, **123**, 315 (1976).

24. M S Whittingham, *Science*, **192**, 1126 (1976).

25. D W Murphy, M Greenblatt, R J Cava and S M Zahurak, *Solid State Ionics*, **5**, 327 (1981).

26. R J Cava, A Santoro, D W Murphy, S M Zahurak and R S Roth, *J. Solid State*

Chem., **42**, 251 (1982).

27. K H Cheng and M S Whittingham, *Solid State Ionics*, **1**, 151 (1980).

28. B Gerand, G Nowogroki and M Figlarz, *J. Solid State Chem.*, **38**, 312 (1981).

29. K H Cheng, A J Jacobson and M S Whittingham, *Solid State Ionics*, **5**, 355 (1981).

30. P G Dickens, S J French, A T Hight and M F Pye, *Mat. Res. Bull.*, **14**, 1295 (1979).

31. B Zachau-Christiansen, K West and T Jacobsen, *Mat. Res. Bull.*, **20**, 485 (1985).

32. D W Murphy, P A Christian, F J Di Salvo and J N Carides, *J. Electrochem. Soc.*, **126**, 497 (1979).

33. D W Murphy, F J Di Salvo, J N Carides and J V Waszczak, *Mat. Res. Bull.*, **13**, 1395 (1978).

34. M M Thackeray, M H Rossouw, R J Gummow, D C Liles, *Electrochim. Acta*, **38**, 1259 (1993).

35. R J Hill, J R Craig and G V Gibbs, *Phys. Chem. Minerals*, **4**, 317 (1979).

36. J D Dunitz and L E Orgel, *Adv. Inorg. Radiochem.*, **2**, 1 (1960).

37. K J Standley, *Oxide Magnetic Materials*, Clarendon Press, Oxford (1972).

38. W B White and V G Keramides, *Nat. Bur. Stand. Spec. Publ.*, **134**, 113 (1972).

39. L Suchow and A A Ando, *J. Solid State Chem.*, **2**, 156 (1970).

40. C Prince and Treuting, *Acta Cryst.*, **9**, 1025 (1956).

41. J D Dunitz and L E Orgel, *J. Phys. Chem. Solids*, **3**, 20 (1957).

42. M M Thackeray, W I F David, P G Bruce and J B Goodenough, *Mat. Res. Bull.*, **18**, 461 (1983).

43. M M Thackeray, W I F David and J B Goodenough, *Mat. Res. Bull.*, **17**, 785 (1982).

44. M M Thackeray, W I F David and J B Goodenough, *J. Solid State Chem.*, **55**, 280 (1984).

45. L A de Picciotto and M M Thackeray, *Mat. Res. Bull.*, **20**, 1409 (1985).

46. W I F David, J B Goodenough, M M Thackeray and M G S R Thomas, *Rev. de Chim. Min.*, **20**, 636 (1983).

47. M M Thackeray, P J Johnson, L A de Picciotto, P G Bruce and J B Goodenough, *Mat. Res. Bull.*, **19**, 179 (1984).

48. A Mosbah, A Verbaere and M Tournoux, *Mat. Res. Bull.*, **18**, 1375 (1983).

49. M M Thackeray, A de Kock, M H Rossouw, D Liles, R Bittihn and D Hoge, *J. Electrochem. Soc.*, **139**, 364 (1992).

50. L A de Picciotto and M M Thackeray, *Mat. Res. Bull.*, **20**, 187 (1985).

51. M G S R Thomas, W I F David, J B Goodenough and P Groves, *Mat. Res. Bull.*, **20**, 1137 (1985).

52. G Dutta, A Manthiram, J B Goodenough and J-C Grenier, *J. Solid State Chem.*,

96, 123 (1992).

53. W D Johnston, R R Heikes and D Sestrich, *J. Phys. Chem. Solids*, **7**, 1 (1958).

54. *JCPDS Powder Diffraction File* 24-600 (1972).

55. L D Dyer, B S Borie Jr. and G P Smith, *J. Am. Chem. Soc.*, **76**, 1499 (1954).

56. W Rudörff and H Becker, *Zeitschr. Naturforsch.*, **98**, 614 (1954).

57. L A de Picciotto, M M Thackeray, W I F David, P G Bruce and J B Goodenough, *Mat. Res. Bull.*, **19**, 1497 (1984).

58. J Morales, C Perez-Vincente and J L Tirado, *Mat. Res. Bull.*, **25**, 623 (1990).

59. J R Dahn, U von Sacken and C A Michal, *Solid State Ionics*, **44**, 87 (1990).

60. H J Orman and P J Wiseman, *Acta Cryst.*, **C40**, 12 (1984).

61. J J Auborn and Y L Barberio, *J. Electrochem. Soc.*, **134**, 638 (1987).

62. K Mizushima, P C Jones, P J Wiseman and J B Goodenough, *Mat. Res. Bull.*, **15**, 783 (1980).

63. J N Reimers and J R Dahn, *J. Electrochem. Soc.*, in press (1993).

64. R Hoppe, G Brachtel and M Jansen, *Z. Anorg. und Allg. Chem.*, **417**, 1 (1975).

65. M H Rossouw, D C Liles and M M Thackeray, *J. Solid State Chem.*, in press (1993).

66. E Plichta, S Slane, M Uchiyama, M Salomon, D Chua, W B Ebner and H W Lin,

J. Electrochem. Soc., **136**, 1865 (1989).

67. J R Dahn, U von Sacken, M W Juzkow and H Al-Janaby, *J. Electrochem. Soc.*, **138**, 2207 (1991).

68. T Ohzuku, H Komori, K Sawai and T Hirai, *Chemistry Express*, **5**, 733 (1990).

69. J M Tarascon, D Guyomard and G L Baker, *J. Power Sources*, **44**, 689 (1993).

70. M F C Ladd and R A Palmer, *Structure Determinaion by X-ray Crystallography*, Plenum Press, New York (1977).

71. L A de Picciotto, K T Adendorff, D C Liles and M M Thackeray, *Solid State Ionics*, in press (1993).

72. A de Kock, M H Rossouw, L A de Picciotto, M M Thackeray, W I F David and R M Ibberson, *Mat. Res. Bull.*, **25**, 657 (1990).

73. M M Thackeray, L A de Picciotto, W I F David, P G Bruce and J B Goodenough, *J. Solid State Chem.*, **67**, 285 (1987).

74. B D Cullity, *Elements of X-ray Diffraction*, Second ed., Addison Wesley, Reading (Massachusetts) (1978).

75. H M Rietveld, *Acta Cryst.*, **22**, 151 (1967).

76. H M Rietveld, *J. Appl. Cryst.*, **2**, 65 (1969).

77. G E Bacon, *Neutron Diffraction in Chemistry*, Butterworths, London (1977).

78. M Zanini, *J. Electrochem. Soc.*, **132**, 588 (1985).

79. M Armand, F Dalard, D Deroo and C Mouliom, *Solid State Ionics*, **15**, 205 (1985).

80. A H Thompson, *J. Electrochem. Soc.*, **126**, 608 (1979).

81. S Basu and W L Worrell in *Fast Ion Transport in Solids*, Vashishta, Mundy and Shenoy (eds), North Holland (1979).

82. T Jacobsen, K West, B Zachau-Christiansen and S Atlung, *Electrochim. Acta*, **30**, 1205 (1985).

83. B B Scholtens, *Mat. Res. Bull.*, **11**, 1533 (1976).

84. A Honders and G H J Broers, *Solid State Ionics*, **15**, 173 (1985).

85. W Weppner and R A Huggins, *Ann. Rev. Mater. Sci.*, **8**, 269 (1978).

86. C Ho, I D Raistrick and R A Huggins, *J. Electrochem. Soc.*, **127**, 343 (1980).

87. J E B Randles, *Discuss. Faraday Soc.*, **1**, 11 (1947).

88. D B Wiles, R A Young, and A Sakthivel, *IUCR Int Workshop on the Rietveld Method*, Petten (1989).

89. J Schneider, *IUCR Int Workshop on the Rietveld Method*, Petten (1989).

90. P J Wiseman, D Phil Thesis, University of Oxford (1974).

91. K Yvon, W Jeitschko and E Parthe, *J. Appl. Cryst.*, **10**, 73 (1977).

92. W Voight, *Munich Ber.*, 603 (1912).

93. W I F David and J C Matthewman, *Rutherford Appleton Laboratory Report* RAL

84 064, SERC (1984).

94. G Kortorz and S W Lovesey, in *Neutron Scattering in Materials Science, A Treatise on Materials Science and Technology,* G Korstorz (ed), **15**, 1 Academic Press, New York (1979).

95. D W Murphy, M Greenblatt, S M Zahurak, R J Cava, J V Waszczak, G W Hull and R S Hutton, *Rev. Chim. Min.*, **19**, 441 (1982).

96. W I F David, M M Thackeray, P G Bruce and J B Goodenough, *Mat. Res. Bull.*, **19**, 99 (1984).

97. M M Thackeray, S D Baker, K T Adendorff and J B Goodenough, *Solid State Ionics*, **17**, 175 (1985).

98. J M Tarascon and D Guyomard, *J. Electrochem. Soc.*, **138**, 2864 (1991).

99. A I Popov and G H Geske, *J. Am. Chem. Soc.*, **80**, 1340 (1958).

100. M Armand in *Materials for Advanced Batteries*, D W Murphy, J Broadhead and B C H Steele (eds), Plenum Press, New York (1980).

101. J C Hunter, *J. Solid State Chem.*, **39**, 142 (1981).

102. T Nagaura, M Yokokawa and T Hashimoto, U K Patent Application G B 2 196 785 (1988).

103. N Furukawa, T Saito and T Nohma, European Patent Application, 0 265 950 (1987).

104. N Furukawa, T Ohsumigaoka and T Nohma, European Patent Application, 0 279 235 (1988).

105. N Furukawa, T Nohma, K Teraji, I Nekane, Y Yamamoto and T Saito, *Denki Kagaku*, **57**, 533 (1989).

106. L Li and G Pistoia, *Solid State Ionics*, **47**, 241 (1991).

107. D W Murphy, R J Cava, S M Zahurak and A Santoro, *Solid State Ionics*, **9-10**, 413 (1983).

108. M H Rossouw, A de Kock, L A de Picciotto, M M Thackeray, W I F David and R M Ibberson, *Mat. Res. Bull.*, **25**, 173 (1990).

109. A Honders, J M der Kinderen, A H van Heeren, J H W de Wit and G H J Broers, *Solid State Ionics*, **15**, 265 (1985).

110. P Lambert, M Harrison and M Edwards, *J. Solid State Chem.*, **75**, 332 (1988).

111. *JCPDS Powder Diffraction File*, 35-782 (1989).

112. E Rossen, J N Reimers and J R Dahn, *Solid State Ionics*, in press (1993).

113. J C Hunter and F B Tudron, *Proc. Electrochem. Soc.*, **85-4**, 444 (1985).

114. J M Tarascon, E Wang, F K Shokoohi, W R McKinnon and S Colson, *J. Electrochem. Soc.*, **138**, 2859 (1991).

115. L A de Picciotto, M M Thackeray and G Pistoia, *Solid State Ionics*, **28-30**, 1364 (1988).

116. A Honders, E W A Young, A J H Hintzen, J H W de Witt and G H J Broers, *Solid State Ionics*, **15**, 277 (1985).

117. M S Whittingham and R R Gamble, *Mat. Res. Bull.*, **10**, 363 (1975).

118. C Delmas and I Saadoune, *Solid State Ionics*, **53-56**, 370 (1992).

119. A Lecerf, M Broussely and J P Gabano, European Patent Application, EP 89110158 (1989).

120. J B Goodenough, D G Wickham and W J Croft, *J. Appl. Physics*, **29**, 382 (1951).

121. I J Pickering, J T Lewandowski, A J Jacobsen and J A Goldstone, *Solid State Ionics*, **53-56**, 405 (1992).

122. G Dittrich and R Hoppe, *Z. Anorg. Allg. Chemie*, **368**, 262 (1969).

123. T Ohzuku, A Ueda and T Hirai, *Chemistry Express*, **7**, 193 (1992).

124. P Barboux, J M Tarascon and F K Shokoohi, *J. Solid State Chem.*, **94**, 185 (1991).

125. W I F David, M M Thackeray, P G Bruce and J B Goodenough, *Mat. Res. Bull.*, **19**, 99 (1984).

126. M M Thackeray, M H Rossouw, R J Gummow, D C Liles, K Pearce, A de Kock, W I F David and S Hull, *Electrochim. Acta*, **38**, 1259 (1993).